AD-A146 968   INFRARED PRESENSITIZATION PHOTOGRAPHY(U) AIR FORCE   1/2
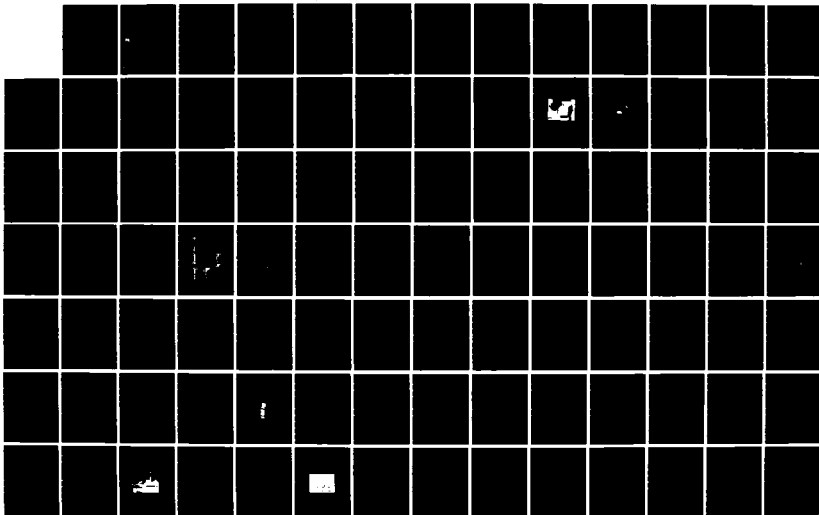   WEAPONS LAB KIRTLAND AFB NM   J M GEARY SEP 84
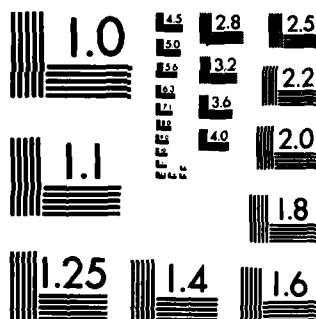   AFWL-TR-84-92

UNCLASSIFIED   F/G 14/5   NL

AD-A146 968

INFRARED PRESENSITIZATION PHOTOGRAPHY

Joseph Martin Geary

September 1984

Final Report

Approved for public release; distribution unlimited.

DTIC
ELECTE
OCT 3 1 1984

S   D

A

AIR FORCE WEAPONS LABORATORY
Air Force Systems Command
Kirtland Air Force Base, NM   87117

DTIC FILE COPY

84   10   25   041

AFWL-TR-84-92

This final report was prepared by the Air Force Weapons Laboratory Kirtland Air Force Base, New Mexico, under Job Order 317J1496. Dr. Joseph M. Geary (ARBB) was the Laboratory Project Officer-in-Charge.

When Government drawings, specifications, or other data are used for any purpose other than in connection with a definitely Government-related procurement, the United States Government incurs no responsibility or any obligation whatsoever. The fact that the Government may have formulated or in any way supplied the said drawings, specifications, or other data, is not to be regarded by implication, or otherwise in any manner construed, as licensing the holder, or any other person or corporation; or conveying any rights or permission to manufacture, use, or sell any patented invention that may in any way be related thereto.

This report has been authored by an employee of the United States Government. Accordingly, the United States Government retains a nonexclusive, royalty-free license to publish or reproduce the material contained herein, or allow others to do so, for the United States Government purposes.

This report has been reviewed by the Public Affairs Office and is releasable to the National Technical Information Services (NTIS). At NTIS, it will be available to the general public, including foreign nations.

If your address has changed, if you wish to be removed from our mailing list, or if your organization no longer employs the addressee, please notify AFWL/ARBB, Kirtland AFB, NM 87117 to help us maintain a current mailing list.

This technical report has been reviewed and is approved for publication.

JOSEPH M. GEARY
Project Officer

FOR THE COMMANDER

JANET S. FENDER
Chief, Phased Array Branch

WINSTON K. PENDLETON
Colonel, USAF
Chief, Laser Science & Test Office

REPORT DOCUMENTATION PAGE

1a. REPORT SECURITY CLASSIFICATION Unclassified	1b. RESTRICTIVE MARKINGS
2a. SECURITY CLASSIFICATION AUTHORITY 2b. DECLASSIFICATION/DOWNGRADING SCHEDULE	3. DISTRIBUTION/AVAILABILITY OF REPORT Approved for public release; distribution unlimited.
4. PERFORMING ORGANIZATION REPORT NUMBER(S) AFWL-TR-84-92	5. MONITORING ORGANIZATION REPORT NUMBER(S)

6a. NAME OF PERFORMING ORGANIZATION Air Force Weapons Laboratory	6b. OFFICE SYMBOL (If applicable) ARBB	7a. NAME OF MONITORING ORGANIZATION
6c. ADDRESS (City, State and ZIP Code) Kirtland Air Force Base, NM 87117		7b. ADDRESS (City, State and ZIP Code)

8a. NAME OF FUNDING/SPONSORING ORGANIZATION	8b. OFFICE SYMBOL (If applicable)	9. PROCUREMENT INSTRUMENT IDENTIFICATION NUMBER

8c. ADDRESS (City, State and ZIP Code)	10. SOURCE OF FUNDING NOS.			
	PROGRAM ELEMENT NO. 63605F	PROJECT NO. 317J	TASK NO. 14	WORK UNIT NO. 96

11. TITLE (Include Security Classification)
INFRARED PRESENSITIZATION PHOTOGRAPHY (U)

12. PERSONAL AUTHOR(S)
Geary, Joseph M.

13a. TYPE OF REPORT Final Report	13b. TIME COVERED FROM Jun 83 TO Jun 84	14. DATE OF REPORT (Yr., Mo., Day) 1984 September	15. PAGE COUNT 190

16. SUPPLEMENTARY NOTATION

17. COSATI CODES			18. SUBJECT TERMS (Continue on reverse if necessary and identify by block number)
FIELD	GROUP	SUB. GR.	Infrared, Photography, Presensitization, Double Exposure Process

19. ABSTRACT (Continue on reverse if necessary and identify by block number)

Infrared presensitization photography (IRPP) is a double exposure technique that allows the recording of IR information on standard silver halide films not ordinarily sensitive in this long wavelength regime. This dissertation prescribes conditions for the practical implementation of the IRPP process in data collection. It then moves on to an investigation of mechanism; i.e., "why does IRPP work?" The study is divided into experimental and theoretical portions, with much heavier emphasis on the former. Experiments delve into the behavior of the characteristic and spectral sensitivity curves of film within the context of the IRPP phenomenon. The temperature rise experienced by the film during this process is determined. The influence of sensitizing dyes and ionic population increases in the grain crystals is also explored. Theoretical efforts concentrate on an extension of the shaw photographic model to explain the IRPP effect in terms of a downshifting in the overall quantum sensitivity requirements of the grain population.

20. DISTRIBUTION/AVAILABILITY OF ABSTRACT UNCLASSIFIED/UNLIMITED ☐ SAME AS RPT. ☐ DTIC USERS ☒	21. ABSTRACT SECURITY CLASSIFICATION Unclassified	
22a. NAME OF RESPONSIBLE INDIVIDUAL Dr. Joseph M. Geary	22b. TELEPHONE NUMBER (Include Area Code) (505) 844-9831	22c. OFFICE SYMBOL ARBB

DD FORM 1473, 83 APR   EDITION OF 1 JAN 73 IS OBSOLETE.

STATEMENT BY AUTHOR

This dissertation has been submitted in partial fulfillment of requirements for an advanced degree at The University of Arizona and is deposited in the University Library to be made available to borrowers under rules of the Library.

Brief quotations from this dissertation are allowable without special permission, provided that accurate acknowledgment of source is made. Requests for permission for extended quotation from or reproduction of this manuscript in whole or in part may be granted by the head of the major department or the Dean of the Graduate College when in his judgment the proposed use of the material is in the interests of scholarship. In all other instances, however, permission must be obtained from the author.

SIGNED:

iii

ACKNOWLEDGEMENTS

TABLE OF CONTENTS

TABLE OF CONTENTS—Continued

List of Illustrations

ix

LIST OF ILLUSTRATIONS—Continued

LIST OF ILLUSTRATIONS—Continued

LIST OF ILLUSTRATIONS—Continued

xii

LIST OF ILLUSTRATIONS—Continued

LIST OF ILLUSTRATIONS—Continued

LIST OF TABLES

LIST OF TABLES—Continued

CHAPTER 1

INFRARED PRESENSITIZATION PHOTOGRAPHY

Introduction

Infrared presensitization photography (IRPP) is a process employed on ordinary photographic emulsions to record information in the near IR wavelengths, e.g. CO_2 laser operation at 10.6 μm. Silver halides are not normally responsive to low energy IR photons. Indeed, silver halide films typically require the cooperation of sensitizing dyes just to gain access to the red end of the visible spectrum. Films characterized as "infrared" usually become quite useless past 1 μm. The IRPP phenomenon sidesteps the energy limitations of IR photons by taking an indirect approach. Two sequential exposures are required. The film is first exposed to the IR radiation pattern of interest (e.g. far field intensity distribution). This is followed closely by a uniform background visible exposure. When the developed film is viewed, regions that received an IR pre-exposure are darker than those areas that received only the visible treatment. Film exposed only to the IR will be clear upon development. The background exposure is essential to the successful recording of the IR information.

1

IRPP was first reported in the literature by Frazier and coworkers[1,2] in 1976. Its discovery seems to have been accidental. Frazier's efforts concentrated on Polaroid 55PN film because of its laboratory convenience. Exposure times for the IR (λ = 5 or 10 μm) were on the order of several seconds; for the visible, they were on the order of 100 ms. Frazier saw both sensitizing and desensitizing effects on the film, usually within the context of the same test. He noted in passing that shorter visible exposures (10 ms) resulted mostly in sensitization. Frazier was also the first to speculate on the mechanisms involved. His efforts, however, focused on temperature-dependent desensitization aspects. The first reported practical application of IRPP was made by Burnett et al.[3] The technique was used to study the spatial structure of plasma breakdown from scattered IR radiation. Mitchel et al.[4] used IRPP to study the far field intensity distribution of a CO_2 laser used for laser-matter interaction studies. Apparently this latter group became so interested in the IRPP phenomenon itself that they explored it further. Mitchel et al.[5] later reported results on multiple IR exposures (a 200-ns train of 1.5-ns pulses spaced by 25 ns). The experimental aspects of this paper dealing with IRPP are generally without fault. However, in their attempts to explain the IRPP phenomenon, there were a number of bad assumptions. For example, they successfully showed that film bulk heated to some steady-state temperature, and exposed to visible light for 10 sec, showed a decrease in sensitivity. The characteristic curve shifted to the

right. From this, they completely discounted emulsion heating due to absorption of IR radiation (visible exposure ~10 ms) as a mechanism responsible for IRPP. Naor et al.[6] showed that Mitchel and coworkers were operating in the low intensity reciprocity failure regime. Had they used the 10-ms visible exposure employed in their IRPP tests, they would have found the characteristic curve shifting to the left because of high intensity reciprocity failure. Another faulty assumption by Mitchel and his group was the identification of Frenkel defects in a silver halide crystal lattice as the trap sites for photoelectrons. Trap sites are predominantly located at strains in the crystal due to edge or screw dislocations. A photoelectron caught here can attract a mobil Ag^+ (Frenkle defect contribution) and form a silver atom. Naor et al.[6] were the first group to seriously consider the question of mechanism. Their work is referred to frequently throughout this dissertation. Juyal et al.[7] report using IRPP in an interferometry experiment. This, however, was essentially the technique employed by Mitchel's group. Even their speculation on mechanism is taken almost directly from Mitchel. Juyal's paper, therefore, has little new to offer. Geary et al.[8] provide the first reported use of IRPP by the U.S. Department of Defense. The Air Force has developed the technique for studying far field patterns of powerful directed energy lasers. They also report the first use of high speed IRPP photography. Their paper provides a good summary of the IRPP phenomenon highlighted with many graphic illustrations. It is also the first paper to clearly point out the importance of the

visible exposure pulse length and the relationship of the IRPP effect to the characteristic curve of the film.

It is the purpose of this dissertation to explore IRPP in some detail and to determine (to some extent) the specific mechanism(s) responsible for the phenomenon. This first chapter examines some of the fundamental experiments[8] by which one gains familiarity with the IRPP phenomenon and some understanding of how the technique is best implemented in practice.

Experiments

The basic experimental arrangement used in these studies is illustrated in Figure 1.1. A CO_2 laser beam (10.6 μm) is incident upon a diffraction "aperture" consisting of two parallel pins (cf Figure 1.2). The pins were used because they could generate significant structure in the far field without removing much power from the beam. The optics following serve two purposes. The first is to form a far field pattern in the film plane of the camera. The second is to pass the ~3 cm diameter incident beam through the small circular aperture (6-mm diameter) of the NRC electronic shutter. The background exposure is supplied via a direct path (no optics) by a flash (or strobe) unit off to the side. The duration of the IR exposure and the relative timing between the IR and visible are determined by the NRC control box. Figure 1.3 is an enlarged print of a typical recorded IR far field pattern.

Perhaps the most important single piece of information about the IRPP process to be garnered is the relationship between the

LASER
IR

PINS— 30cm f/3 (Ge)

5.1cm f/2.7 (ZnSe)

NRC ELECTRONIC SHUTTER

STROBOTAC
(VISIBLE)

25.4cm f/9.1 (ZnSe)

FILM PLANE
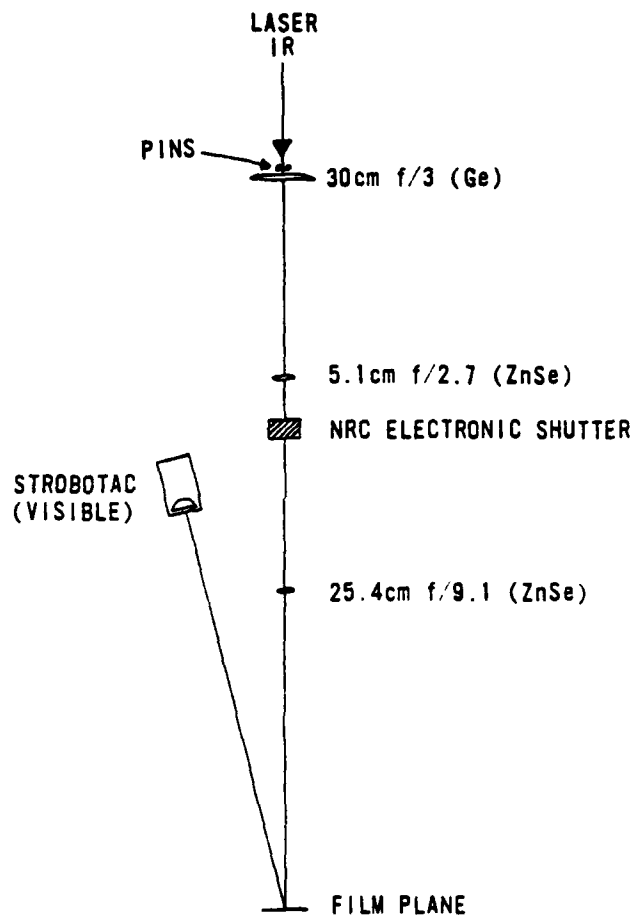
Figure 1.1. Experimental arrangement for studying IRPP.
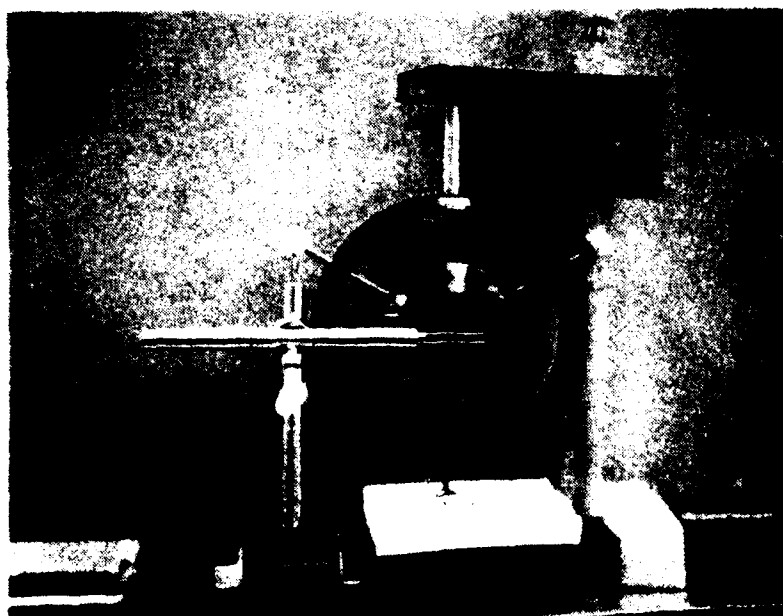
Figure 1.2. Pair of metal pins used as
"diffraction aperture".

Figure 1.3. Far field diffraction pattern
due to metal pins.

density showing up on the test film and the IR energy that was deposited on it. This requires the correlation of two distinct measurements, one radiometric, and the other densitometric. For example, the air image of the pattern shown in Figure 1.3 was scanned with a calibrated "pinhole" (380-μm) radiometer, Laser Precision Model RK 3441. Figure 1.4 is the resulting data plot. For correlation purposes with density information, peaks were arbitrarily labeled by letters, valleys by numbers. Microdensitometer scan data is presented in Figure 1.5 for three different exposure levels. (Note: This is specular density data.) In Figure 1.5a, points A, B, C, 7, 8, and 9 map with some fidelity to the radiometric scan. However, for points F and G something very odd is happening. As the IR energy is increased, these points, instead of increasing, actually decrease in density. They are driven not only below the background density, but toward zero! This is rather bizarre behavior. If we overlap Figures 5a–c (as is done in Figure 1.6), we note another curious feature. There is a density "ceiling" around a value of 1.1. This is not a saturation value. The Kodak 5369 film used for most of the studies saturates at a density around 3.3. By correlating points in the radiometric scan with the microdensitometer data, we obtain density vs IR energy (DIRE), the curve shown in Figure 1.7. Initially, the curve is linear, but it gradually rolls over, peaking at the density "ceiling." It then reverses its density trek despite increasing IR energy. The reason for the ceiling and reversal effects is not at all understood and further complicates investigations into the IRPP mechanism.
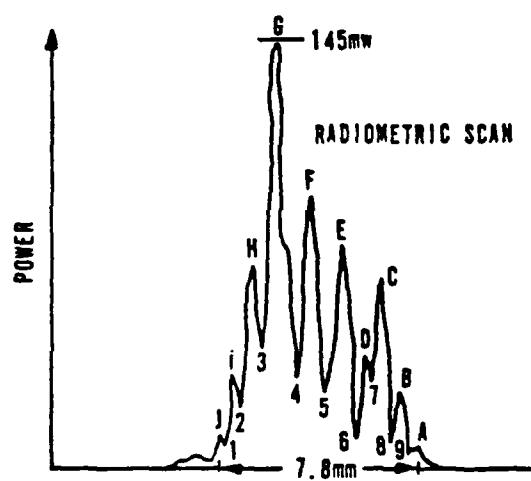
Figure 1.4. Radiometric scan of IR diffraction pattern.
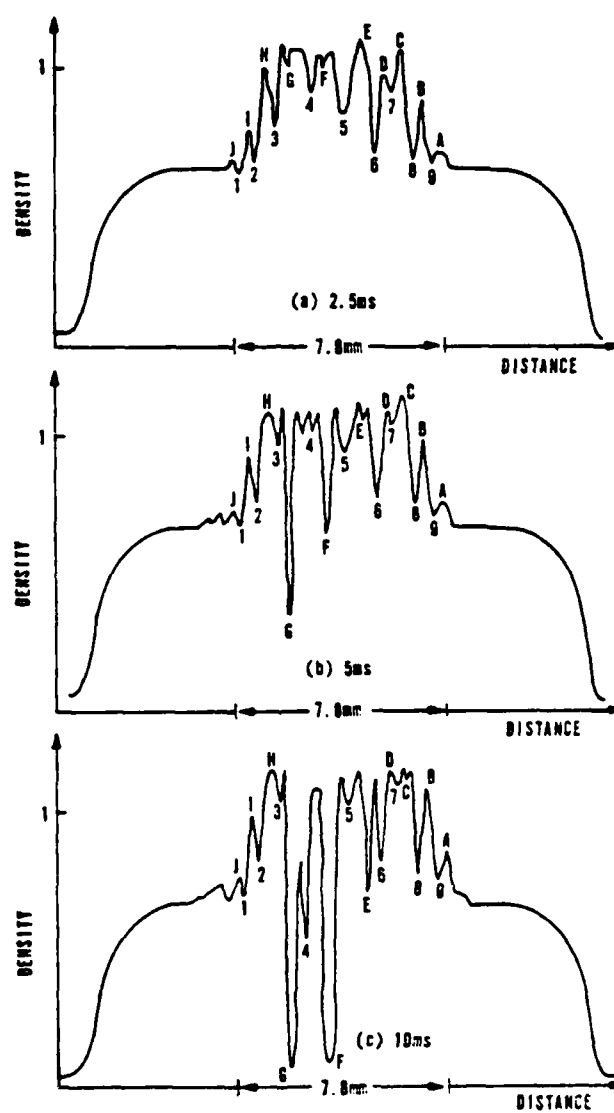
Figure 1.5. Microdensitometer scans of diffraction pattern
for three different IR exposure levels.
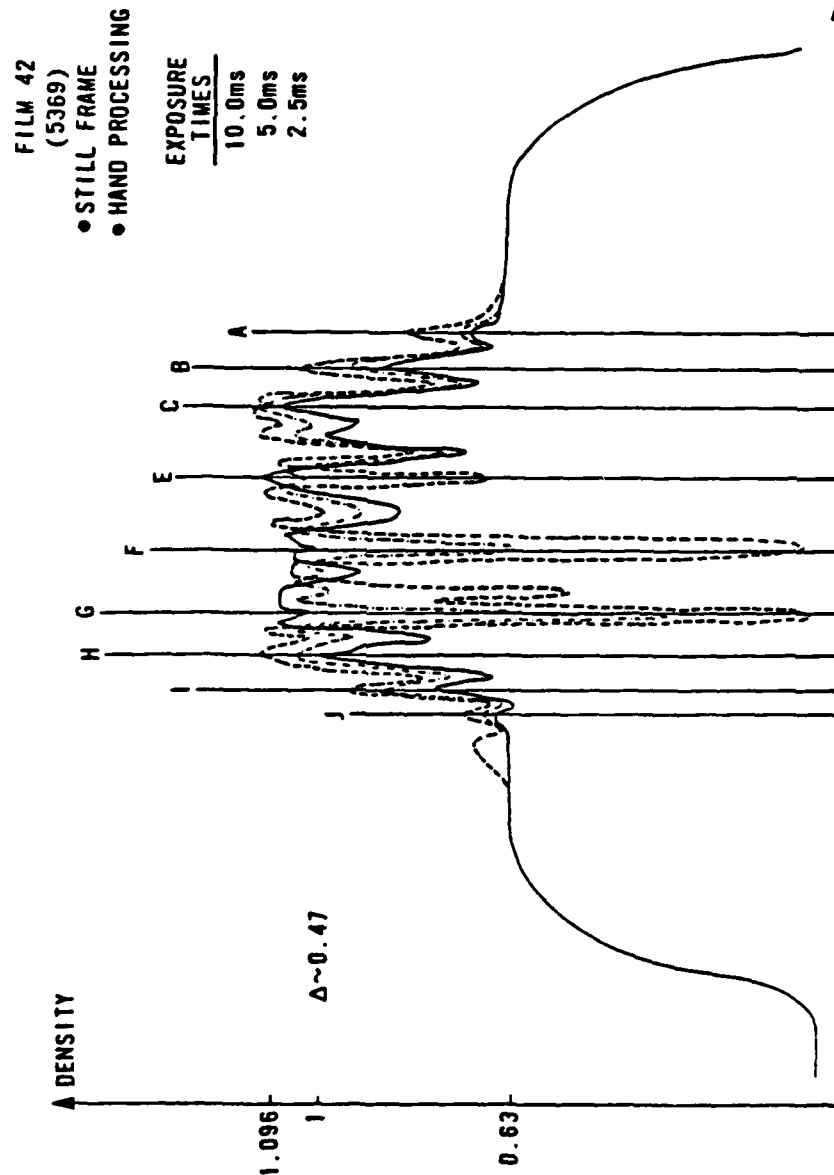
Figure 1.6. Overlap of the three microdensitometer scans.
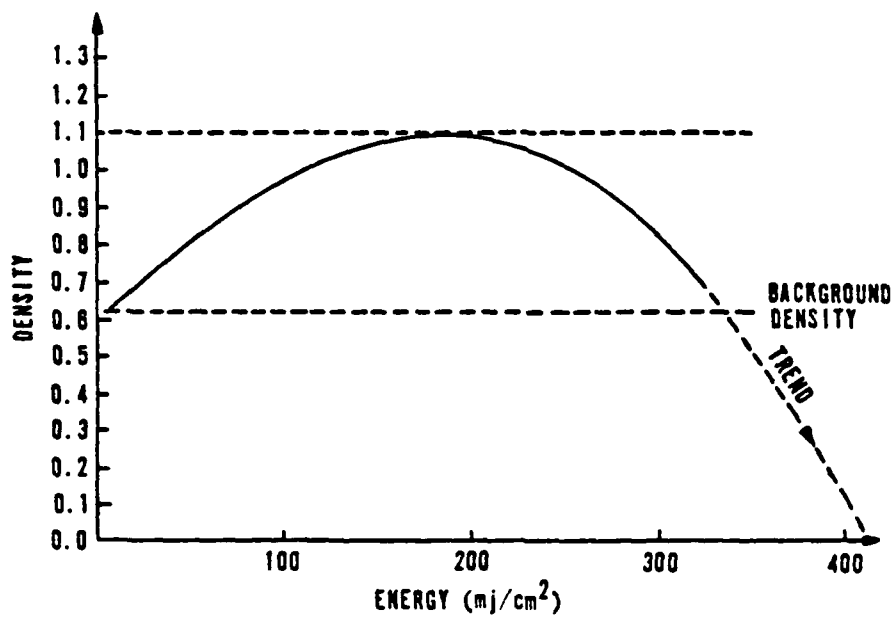
Figure 1.7. Plot of density vs IR energy.

Note that the sampling aperture of the microdensitometer was a 50-μm square, much smaller than that of the radiometer. For low resolution structures such as the diffraction pattern in Figure 1.3, this should not introduce significant discrepancies in the DIRE curve. The reason for the different sampling apertures was a result of instrument limitations. A much smaller aperture on the radiometer resulted in very poor signal-to-noise ratio. On the microdensitometer, the 50-μm square was the largest nonslitlike aperture available. There were no circular apertures. Furthermore, the tracks of the radiometer and microdensitometer scans do not exactly coincide. Small translation and angular discrepancies are present that influence the DIRE curve.

The visible source (used to obtain the previous information) delivered most of its energy to the film within 2 ms. Figure 1.8 compares the IRPP effect of this flash unit with a faster General Radio strobe, which deposits most of its energy within 2 μs. Timing information is also provided. The differences are striking, particularly when Figure 1.8 is compared to the complementary radiometric data provided in Figure 1.9 for this comparison test. The fidelity between Figure 1.9 and Figure 1.8b is excellent. But is the difference between Figure 1.8a and 8b really due to temporal properties, or is it due to spectral dissimilarities? Figure 1.10 shows the spectral comparison between the flash and strobe units, the latter being more heavily weighted in the blue. To settle this question, a narrowband interference filter (cf Figure 1.11) was used
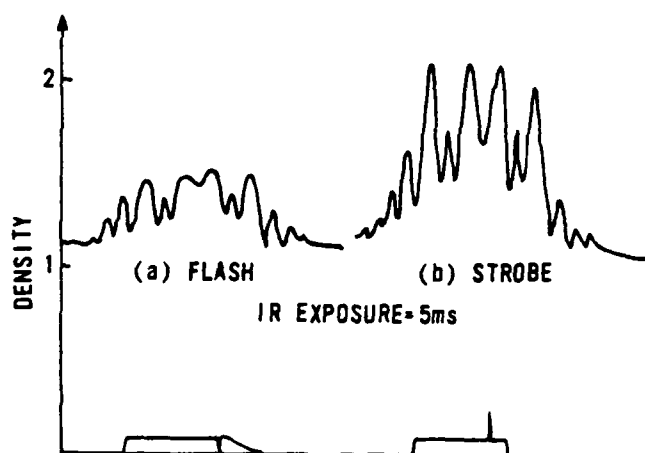
Figure 1.8. Microdensitometer comparison:
long vs short visible exposure.
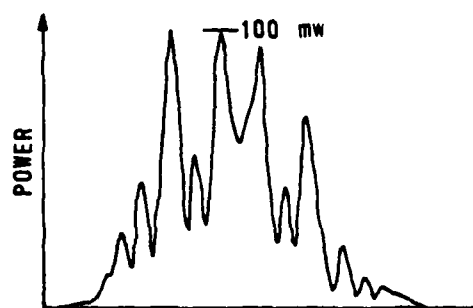
Figure 1.9. Radiometric scan of IR pattern
used for visible pulse length
exposure test.
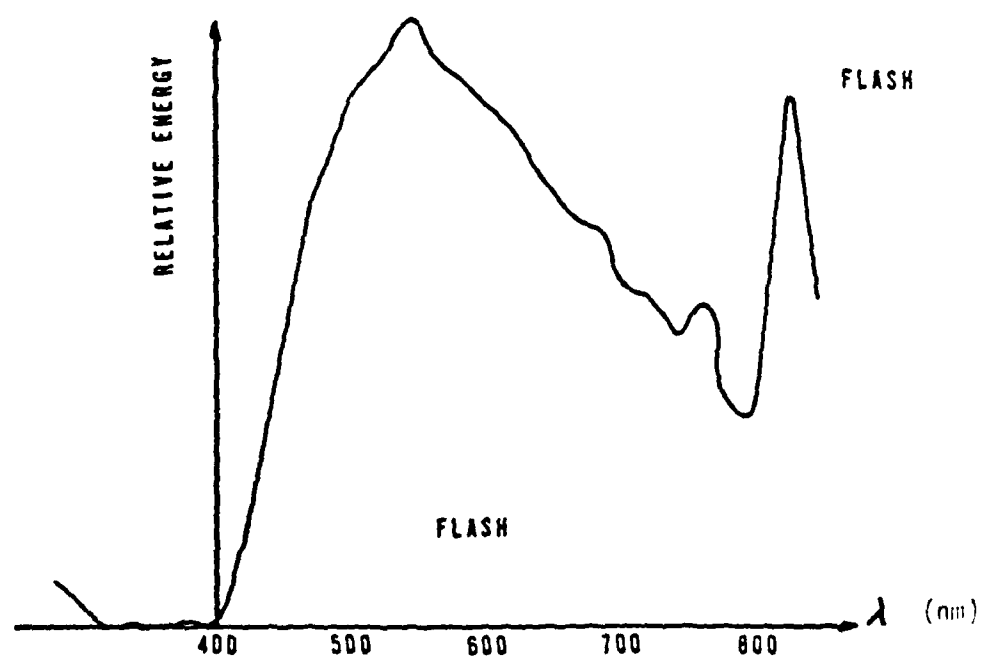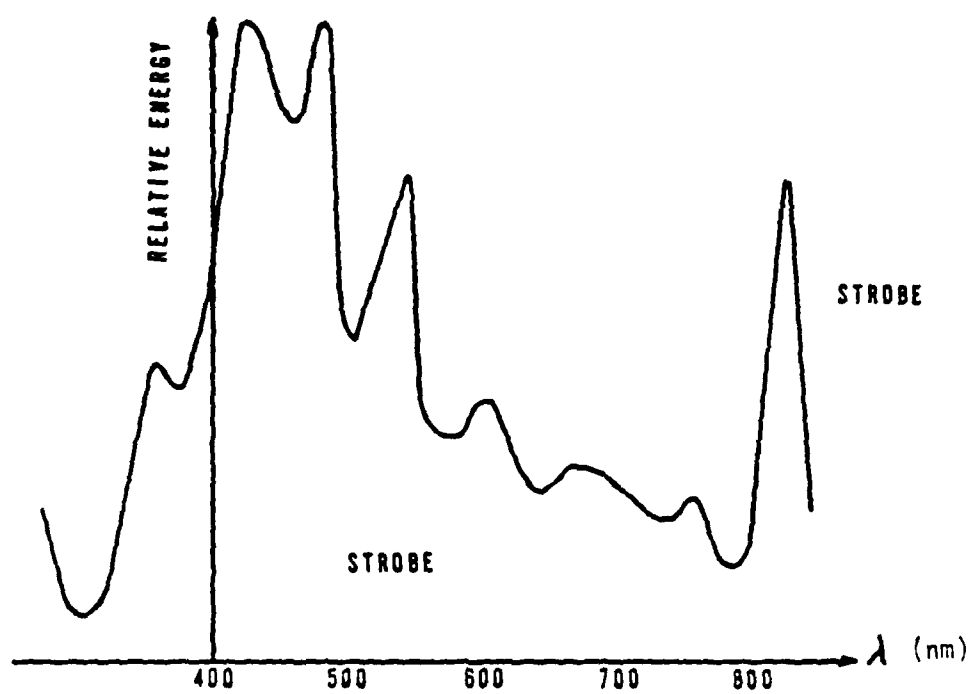
Figure 1.10. Comparison of flash vs strobe spectra.
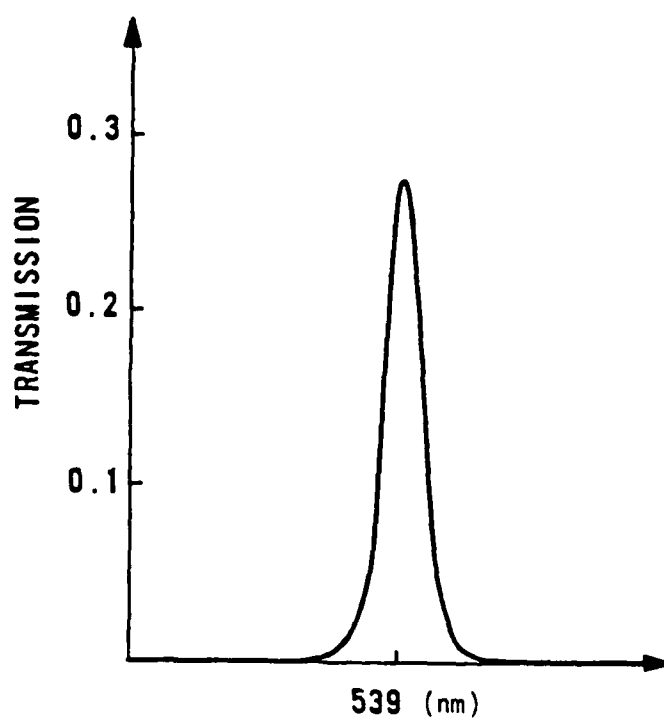
Figure 1.11. Relative transmission of narrow
band interference filter.

to make exposures with both units. In this way, the spectral contents were identical, leaving only the temporal differences. Figure 1.12 shows the results. The attempt to match background densities exactly was unsuccessful. However, the flash background is adequately bracketed by those obtained for the strobe to definitely confirm that the visible pulse length is critical to obtaining a faithful rendition of the IR pattern. This is also reflected in the DIRE curve, as seen in Figure 1.13. The linear region is greatly extended, the rollover point being about 1200 mJ/cm^2 farther out. There still is a density ceiling but at a much higher level. Reversal also takes place after 1.4 J/cm^2. Note that there is another reversal around 2.2 J/cm^2. This time, however, the film is being damaged. The emulsion is actually charring, and will, with more energy, burn completely off, leaving clear base material. Note also that the density difference between background and ceiling is approximately twice that of Figure 1.7.

There is one other factor that must be considered when comparing visible pulse lengths...reciprocity failure. When using the long pulse source (green filter) to obtain a background density around 0.4, we deposited approximately .01 $ergs/cm^2$. To get this same background density with the short pulse (green filter), the visible energy was increased to around .03 $ergs/cm^2$. In other words, the film is less sensitive to the short pulse. Yet looking at Figure 1.12, the density values of the strobe plots are quite dramatic in relation to the flash data. It seems unlikely that visible
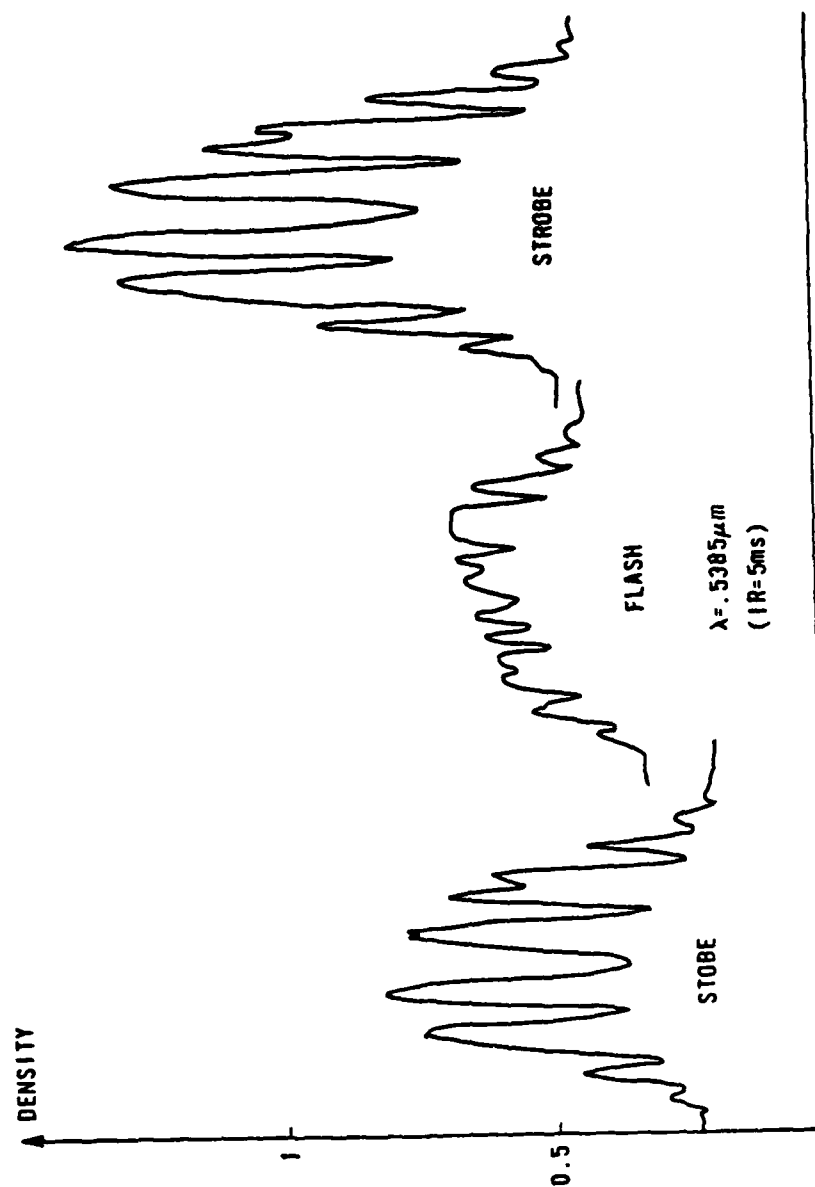
Figure 1.12. Microdensitometer comparison for long and short exposures using same spectrum.
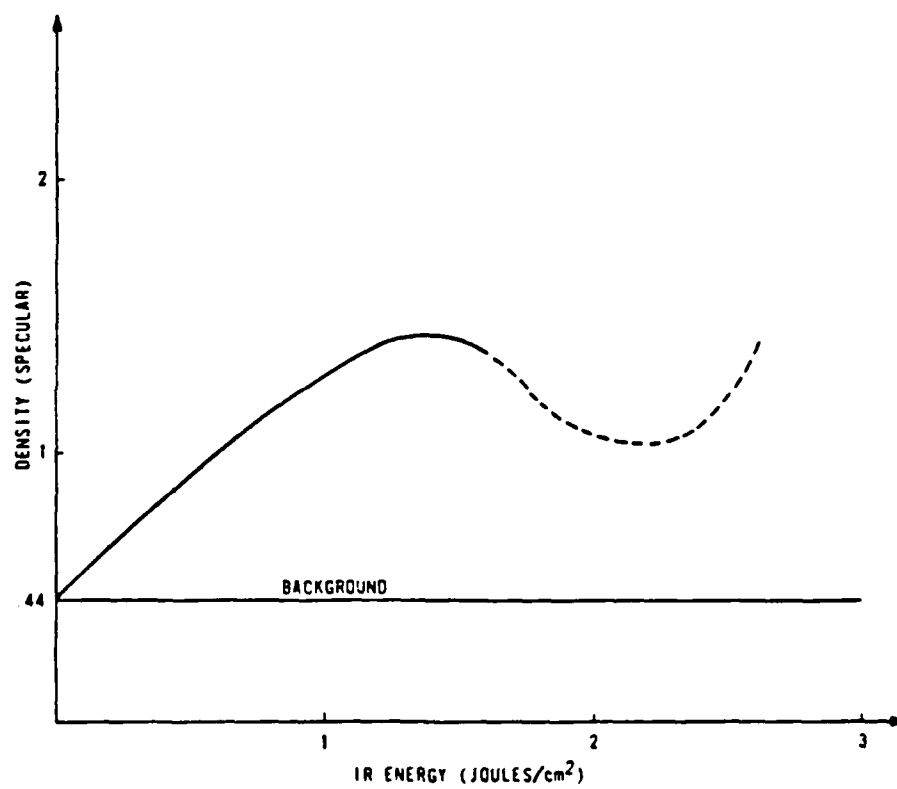
Figure 1.13. DIRE curve for short visible exposure.

reciprocity is playing a significant role in the context of these experiments.

Aside from visible reciprocity effects, the possibility of IR reciprocity failure must also be kept in mind. Figure 1.14 shows a limited test indicating that reciprocity is holding up (over an experimental range of interest). However, if IR exposure times are changed an order of magnitude or more (keeping energy constant), then the IRPP response of the film may be quite different.

If we compare the two strobe plots in Figure 1.12, we note that the left-hand side is weaker than the right-hand side. This is a reflection of the characteristic curve influence of the film. This is explored in more detail in Figure 1.15, where the background density is varied across the full range of the characteristic curve. In the toe and shoulder regions, modulation (relative to local background) is low. We define modulation here as: $M = (\hat{D} - \check{D})/(\hat{D} + \check{D})$, where $\hat{D}$ is the high density value (minus background) and $\check{D}$ is the low (minus background). In the linear region of the Hurter and Driffield (H and D) curve, modulation values remain fairly stable.

Next, we look at the effect of relative timing between the IR and visible exposures. The results are shown in Figure 1.16, where a through d show a simple monotonic increase in density. The relationship between the highest density peak and the visible pulse position is shown in Figure 1.17. The plot is practically linear below 5 ms. IR energy deposited after the visible flash is impotent, When the exposures no longer overlap, the modulation pattern remains
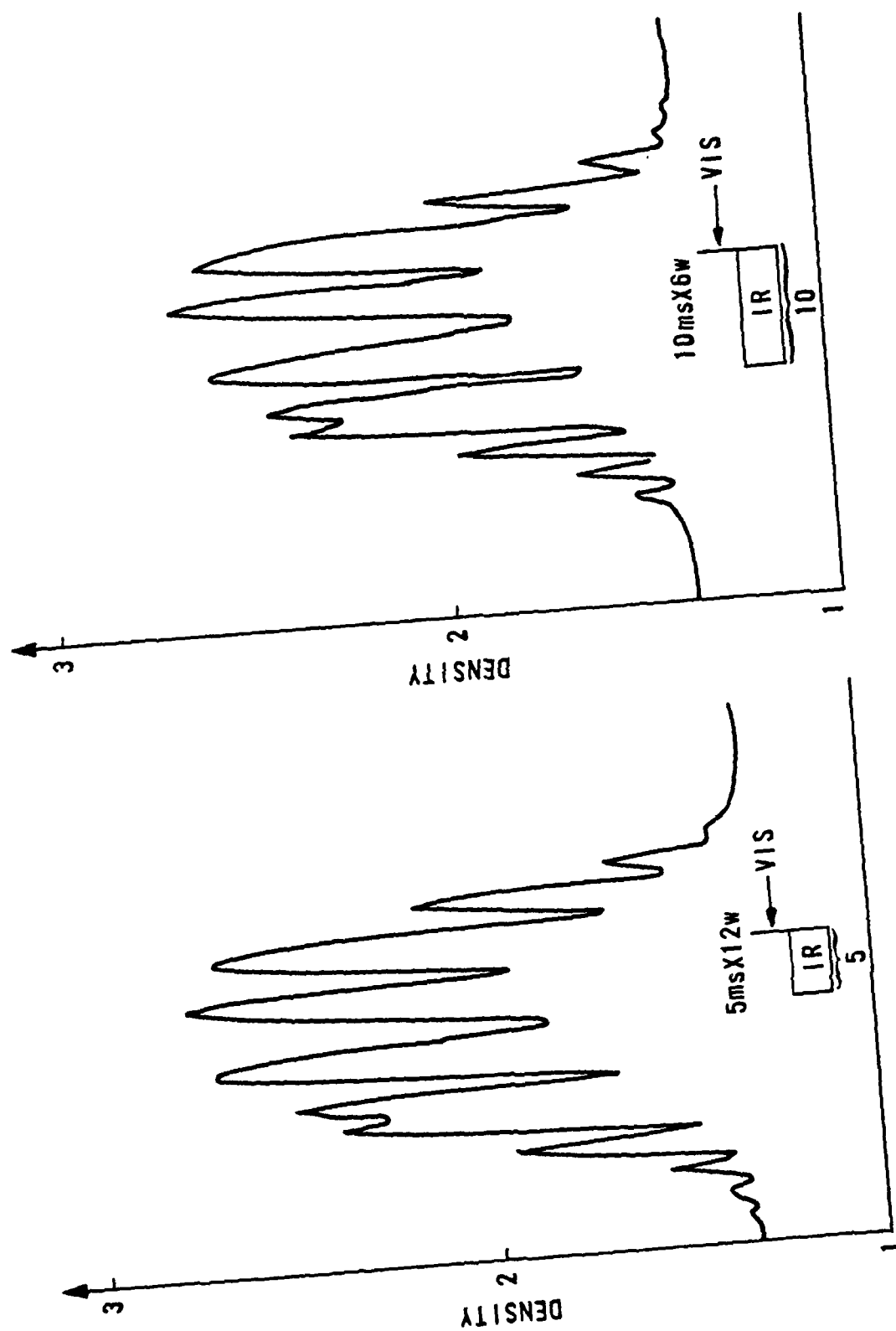
Figure 1.14. Reciprocity failure test in the IR.

21
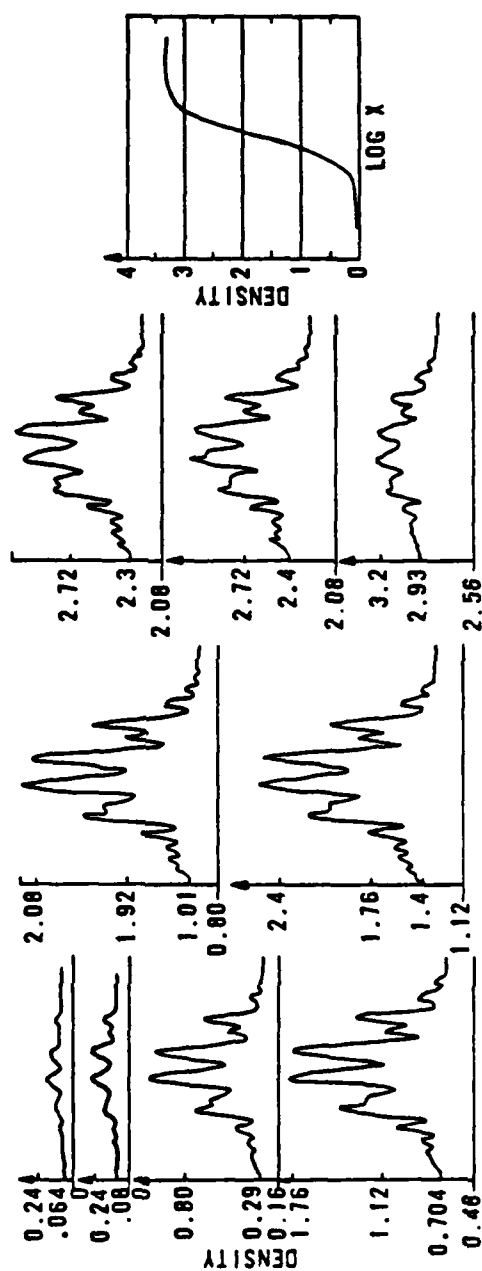
Figure 1.15. The effect of varying the background density on IR dynamic range.
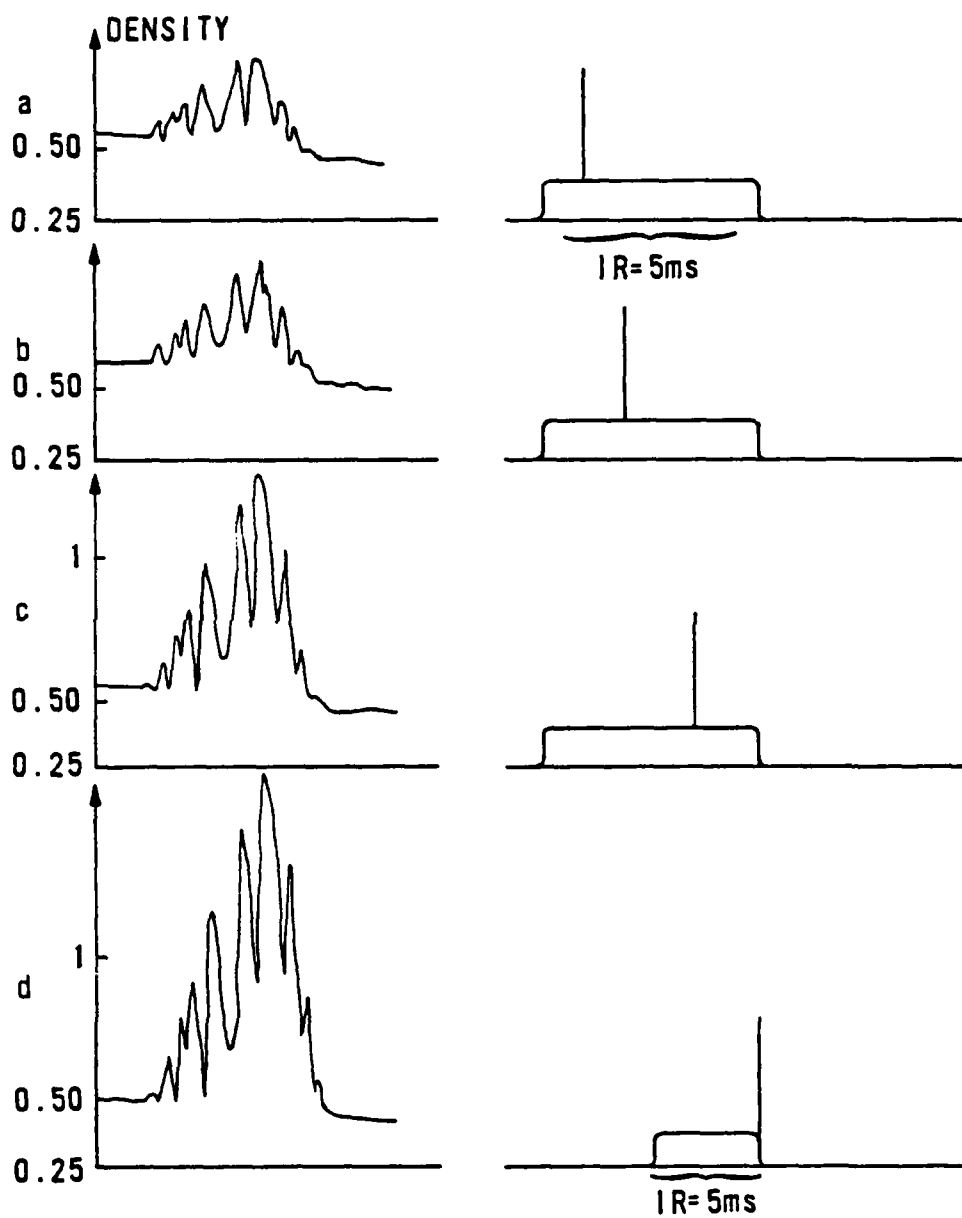
Figure 1.16. Effect of relative timing between IR & visible exposures on IR dynamic range.
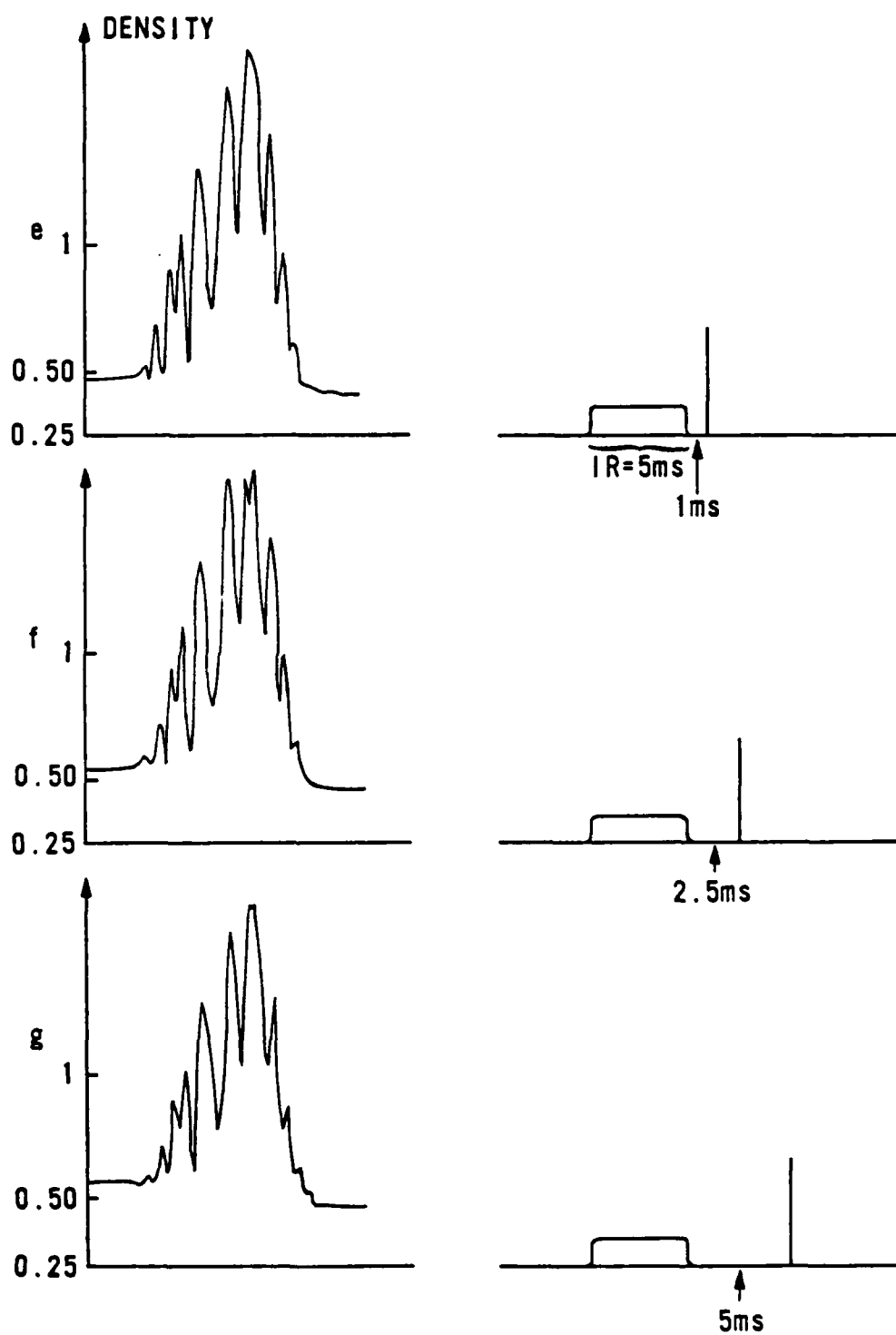
Figure 1.16. continued
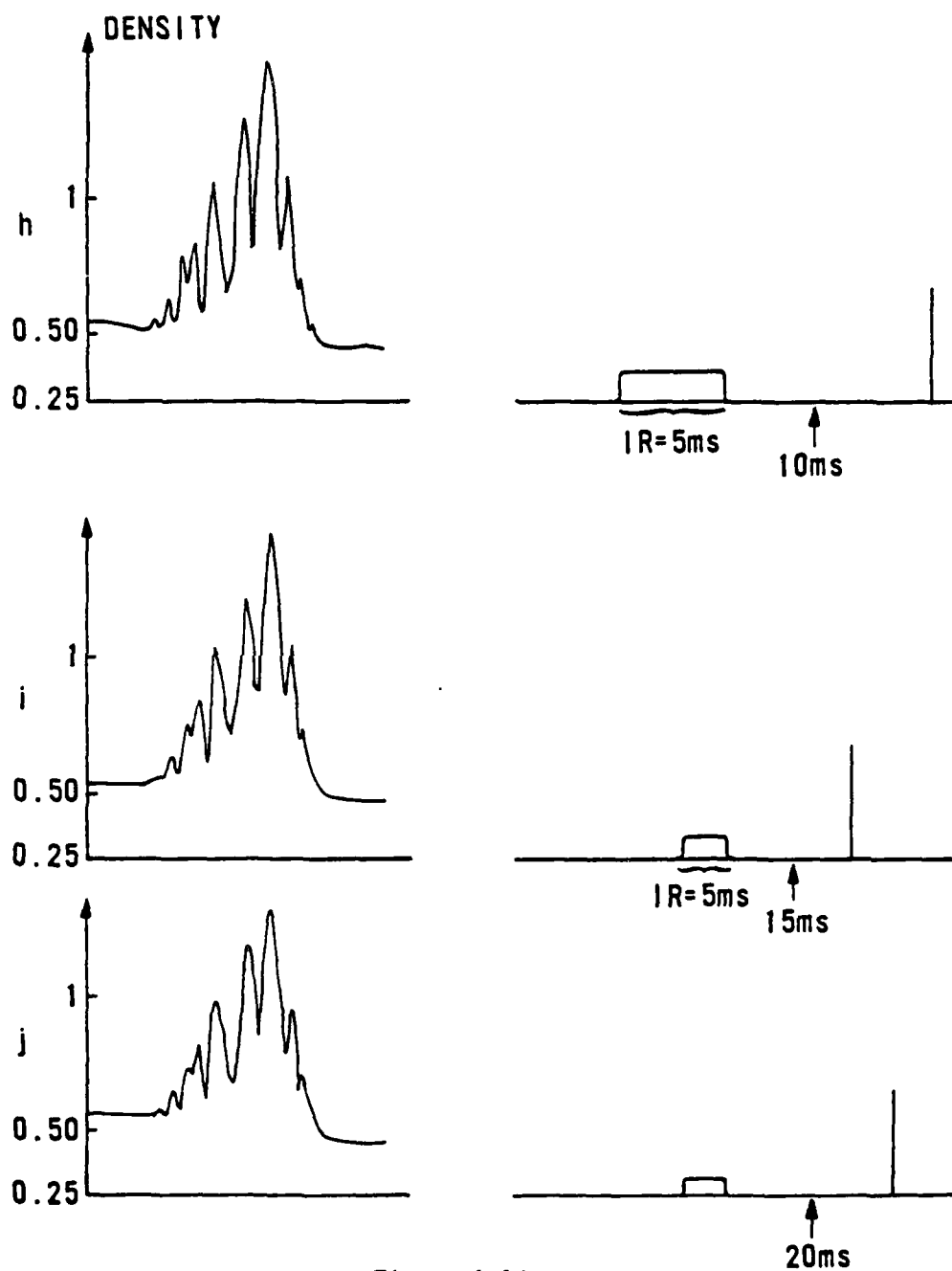
Figure 1.16. continued
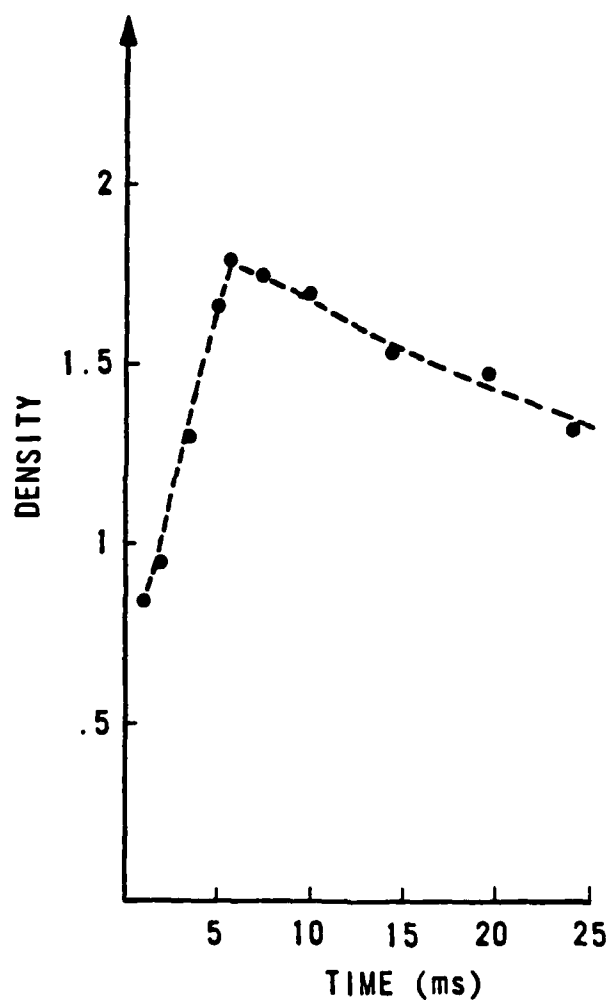
Figure 1.17. Plot of density peak vs relative exposure.

fairly constant out to 5 ms separation. Slow degradation occurs thereafter.

We now summarize what we have learned about IRPP implementation. First, we should use a quick visible exposure (on the order of several microseconds). Second, that exposure should be made within 1 ms of the completion of the IR exposure. Third, we must operate on the linear portion of the H and D curve. Fourth, we must operate on the linear portion of the DIRE curve. The linear density range of the DIRE curve is significantly less than that of the H and D curve. Consequently, we can slide the DIRE curve (by changing background density) along the H and D curve over quite a range without danger that nonlinear behavior will compromise the results.

Other Films

Most of the experimental studies in this dissertation make use of Kodak 5369 film, salient features of which are discussed in Chapter 6. This film showed the greatest sensitivity to the IRPP effect. However, other films were tried, including commericial PAN-X, PLUS-X, and TRI-X. Figure 1.18 presents a composite portrait of the performance of these films as a function of IR energy and background density for the long pulse length visible exposure. The data curves in Figure 1.18 are microdensitometer traces. These films received standard processing (hand). Figure 1.19 is a similar presentation for the short pulse length visible exposure. From this comparison we again see that the short flash is better than the long
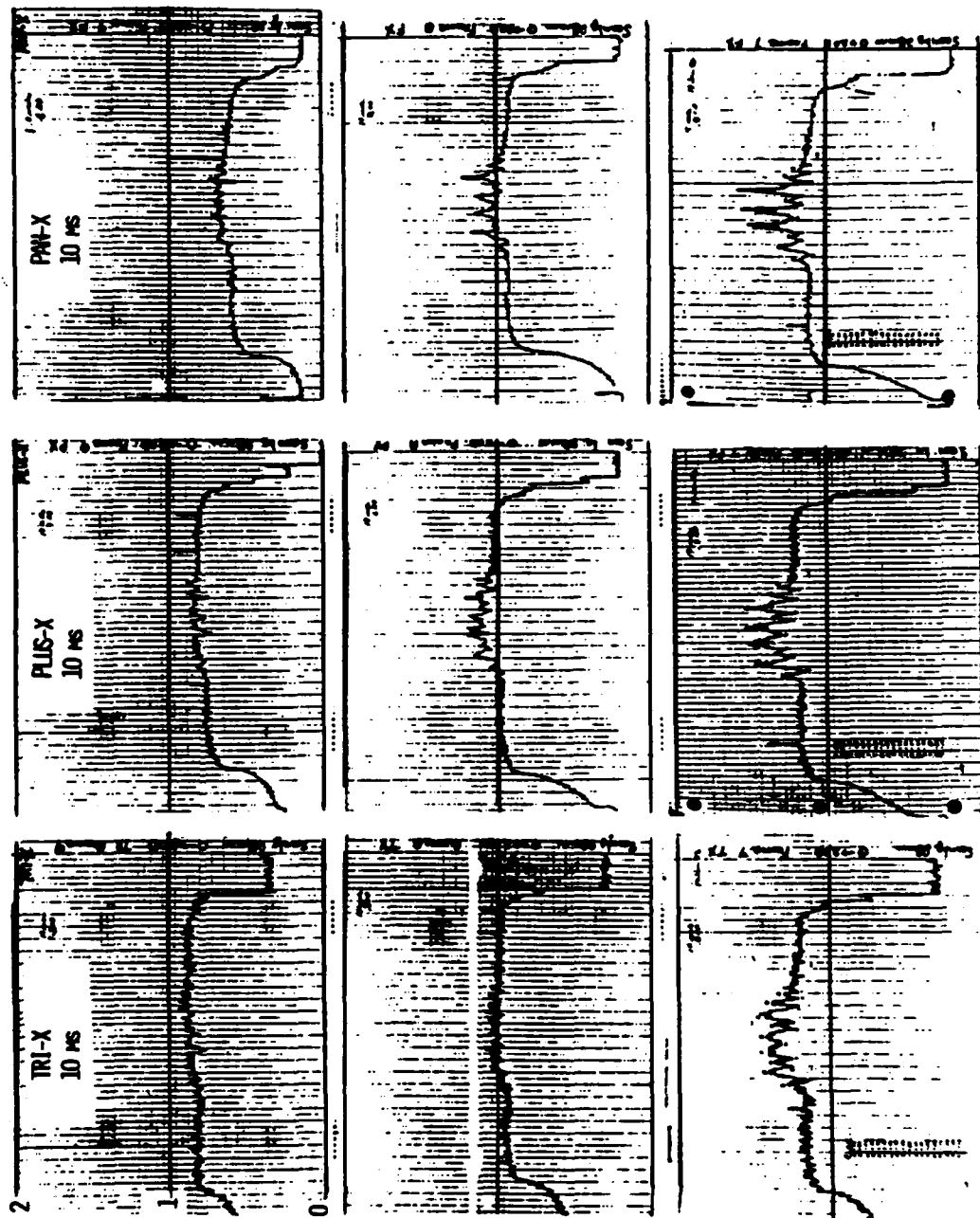
Figure 1.18. Film comparison for long duration visible exposure.
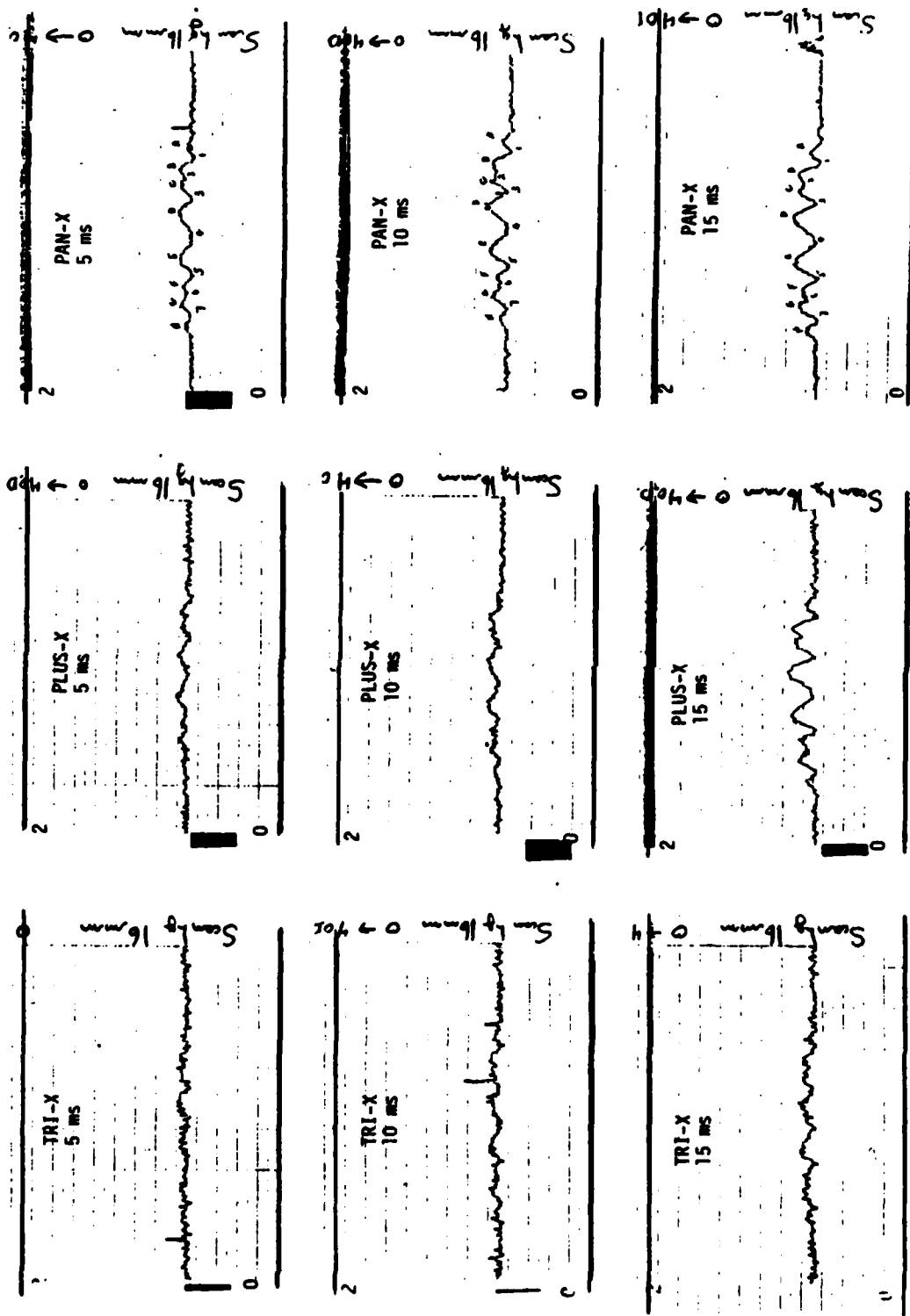
Figure 1.19. Film comparison for short duration visible exposure.

flash. We also see that fine grain emulsions do better that coarse grain emulsions.

Discussion

The IRPP process is a useful tool. It has been implemented successfully at the U.S. Air Force Weapons Laboratory for beam diagnostics on some of the Air Force's high energy laser systems, where it has proved invaluable in obtaining very high spatial resolution data in a wavelength regime dominated, until recently, by electro-optic imaging systems. The latter, though offering higher sensitivity, lack the superior definition available in a photographic film. This is IRPP's distinct advantage. Elect.o-optic sensors initially appear to have the advantage in speed. But weigh this against Mitchel's experiments in which he recorded IR information using laser pulses nanoseconds in duration. IR electro-optic imagers are costly both to purchase ($10,000 to $100,000) and to repair. They also require separate data storage systems. Many sensors need sophisticated cooling systems to attain operational status. The sensors themselves are not robust. They cannot withstand strong mechanical shocks or significant photon overload. An IRPP system, on the other hand, has the transducing, recording, storage, and display capabilities all within the same medium. Moreover, film is cheap, rugged, and reliable.

Though IRPP is a valuable technique, its basic physics are not well understood. Since 1976 there have only been a handful of papers on the topic (cf references). Of these, only that by Naor et

al.[6] seriously considers mechanism. Naor and coworkers consider heat as the principal physical cause of IRPP. They attempt to relate this to variations in the film's spectral sensitivity. In their experiments, they used Kodak 5367, a blue-sensitive emulsion. A short pulse light source filtered with various narrowband interference filters was used to expose film that had either been bulk heated to some steady-state temperature or irradiated with IR energy from a CO_2 laser operating with a pulse time of 0.1 μs. The idea was to relate the steady-state temperature to the transient deposition of IR energy by means of a common density value.

It is generally not a good idea to compare density values based on local transient temperature effects induced by radiation-matter interaction to those resulting from bulk contact type steady-state heating. The solid-state physics between the two could be quite different. Even if heat is a prime cause, the mechanism is not really explained unless issues surrounding latent image formation are considered. It must always be kept in mind that the density induced via the IRPP process is a function of the number of latent image grains formed over and above those brought on-line by the background exposure. It is at grain sites that the real physics of IRPP is taking place. Naor et al. never address this key issue.

Latent image formation is a complex process. Only a broad brush stroke theory (Gurney-Mott) is generally accepted. The details are still being hammered out in the arena of competing theory and experiment. The areas of agreement are as follows: (1) Within a

silver halide grain there are silver ions that have vacated their proper home in the crystal lattice (Frenkel defects). These have a certain freedom to wander about the confines of the crystalline structure. (2) A photon incident upon the grain is absorbed, and it liberates a photoelectron. (3) The photoelectron thus created has a certain probability of being caught at a trap—site. A trap—site is usually located along strain lines in the crystal. (4) The trap—site, with its captured photoelectron, has a chance of catching one of the free silver ions by Coulomb interaction. When this happens the trap—site contains a silver atom. (5) A single silver atom is not thermodynamically stable, and will dissociate owing to thermal excitation unless another photoelectron and silver ion get married at the same trap—site. Two silver atoms located at the same place form a stable configuration that will last. This process is called "nucleation." (6) Though a stable center has been formed, two silver atoms are insufficient to act as a catalyst in the development process. For this purpose, four or five silver atoms are needed at the common site. Such growth (due to continued interaction between photoelectrons and free silver ions) is termed "aggregation," and the site of such accumulated silver is called a "latent image center." (7) The latent image center is a catalyst that enables the developer to reduce the entire silver halide crystal grain to pure silver.

The IRPP process influences the statistics of latent image formation. Somehow more latent image grains are formed. This may be due to a grain's response to heat. But heat may also just be a side

effect, handy for correlating other parameters. It may be that the IRPP effect is a quantum phenomenon involving a direct IR photon-grain interaction, captured for posterity by the visible background exposure. In any event, it is the aim of this present study to perform experiments and theoretical analyses to further elucidate various aspects of the IRPP process, and to attempt some fundamental understanding of the physical mechanism responsible for the phenomenon. We begin, in Chapter 2, with an experiment to determine how IRPP affects the most fundamental dynamic property of a film, its characteristic (or H and D) curve. In Chapter 3, we look at a more comprehensive experiment examining the effect of IRPP on a film's spectral sensitivity curve. Recall that Naor et al.[6] used only four specific wavelengths. We employ the full visible spectrum. In Chapter 4, we actually determine how hot the film gets during the highly transient deposition of IR energy. Naor et al., for instance, looked only at bulk steady-state heating, i.e., they pressed the film against a hot plate. Analytical efforts are reported in Chapter 5. Here we use a theoretical model (developed by Dr. Rodney Shaw) for predicting density and detective quantum efficiencies of film emulsions responding to visible spectrum sources. However, we use this model in an unconventional way in order to explain the linear part of the DIRE curve. Chapter 5 also begins our exploratory probing of mechanism, which continues into the remaining chapters. In Chapters 6 and 7, we investigate the influence of sensitizing dyes and ionic conductivity respectively as potential causes of IRPP. Concluding remarks are presented in Chapter 8.

CHAPTER 2

THE CHARACTERISTIC CURVE

Introduction

The Hurter-Driffield curve is perhaps the most fundamental relationship characterizing the photographic process. Consequently, it is important to determine how this characteristic curve is affected by the IRPP process. We wish to conduct this investigation on the time scale of the phenomenon itself. The experiment, therefore, does not utilize steady-state temperature techniques as employed by Naor et al.,[6] but rather attempts to catch the highly transient phenomenon as it occurs. This is done by first exposing the film to an IR gaussian beam for several milliseconds. The IR exposure is followed immediately with a visible exposure from the short duration pulse. However, this is not a background exposure as described in Chapter 1. In this experiment, we are microimaging a density step tablet in the center of the gaussian pattern. The image is so small that the variations in IR energy over this region can be considered negligible. In other words, the IR-induced film temperature across the image of the step tablet is uniform.

Experiment

The experimental arrangement is shown in Figure 2.1. The IR path is similar to that described in Chapter 1, but without the diffraction pins. Thus a fairly clean gaussian beam irradiates the film plane. The visible path consists of a Kohler illumination system used to provide uniform irradiance at the plane containing the density step transparency. This transparency contained a total of 10 steps, and was 1.5 cm long by 0.3 cm wide. A microdensitometer scan of the transparency is shown in Figure 2.2. It is not a very high contrast target. This density step transparency (or wedge) was then imaged by a microscope (operating in reverse) onto the film plane. The image was approximately 1 mm long, and centered in the gaussian IR pattern. Figure 2.3 presents a microdensitometer scan through the gaussian IR pattern (5-ms exposure) made with the usual visible background exposure. The relative wedge size and location are also indicated. In the actual test, only the region of the wedge received a visible exposure. The outlying gaussian pattern received no such treatment and was therefore not recorded.

Exposures were made in the IR at 0, 5, 10, 15, and 20 ms, corresponding to energy deposition values at the peak of the gaussian of 0, 400, 800, 1200, and 1600 mJ/cm^2 respectively. Figure 2.4 compares print enlargements of the 0, 5, and 20 ms cases. The change in the density distribution is evident, becoming heavier for increasing IR exposure. To make sure data were obtained over the full range of the characteristic curve, a number of neutral density
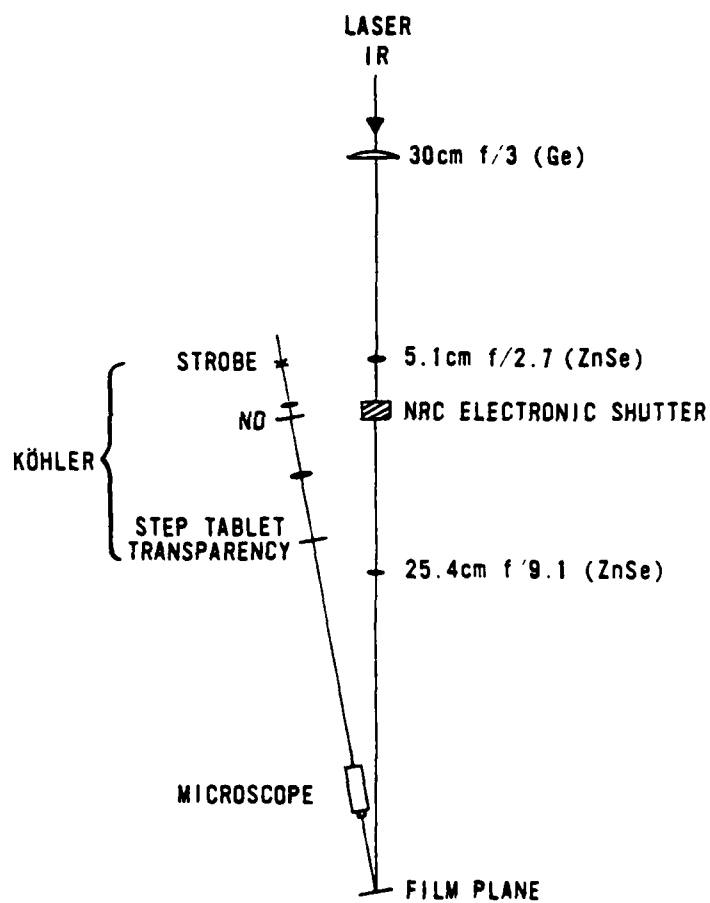
Figure 2.1. Experimental arrangement for
measuring characteristic curve
effects.
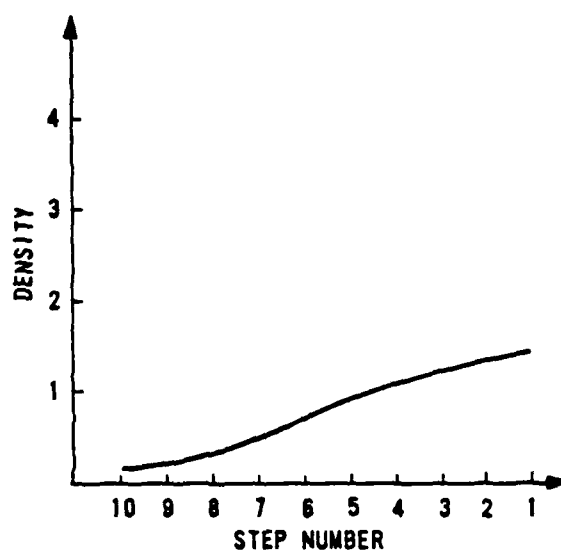
Figure 2.2. Microdensitometer scan of step transparency.
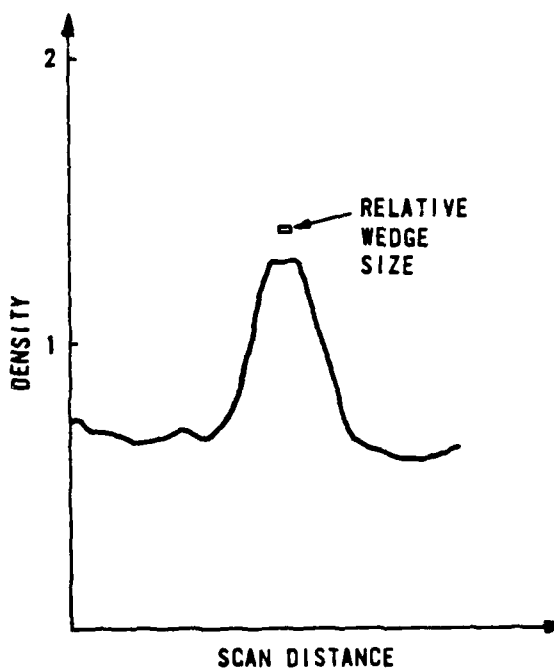
Figure 2.3. Microdensitometer scan of gaussian laser pattern.

Figure 2.4. Microimage negatives for 0,5, and
20 ms IR exposures.

(ND) filters were used in the visible path. (Processing of the Kodak 5369 film was done in D-72, 69°F, 3 minutes, with agitation, gamma ~3.3.) The wedge images on the film were traced with a microdensitometer having a 20-μm-square sampling aperture. An example is shown in Figure 2.5 for a 20-ms exposure. As an aid in determining the density level of various steps, a grid overlay was employed. This is illustrated in Figure 2.6. Points selected as representative of the density of a particular step are also shown. The grid was needed because there were occasions when not all steps were clearly defined on the microdensitometer trace.

Table 2.1 lists the density values for all cases, including those made over the range of Nν density filters. The data are plotted in Figure 2.7, for 0, 0.2, and 0.4 ND. In all cases, the characteristic curve shifts to the left with increasing amounts of IR energy, i.e., it becomes more sensitive with increasing temperature. Note that the biggest lateral shift occurs between 0 and 5 ms. Displacements are more modest after that.

Discussion

With this information, we can understand, at least in a qualitative way, how the DIRE curve is related to the characteristic curve. This is illustrated in Figure 2.8. The right-hand side of the graph shows a family of characteristic curves, each shifted according to temperature. (Keep in mind that the temperature of the film is directly related to IR energy deposited.) We use a certain visible exposure, q$_\theta$, for all cases. On the room temperature (no IR)
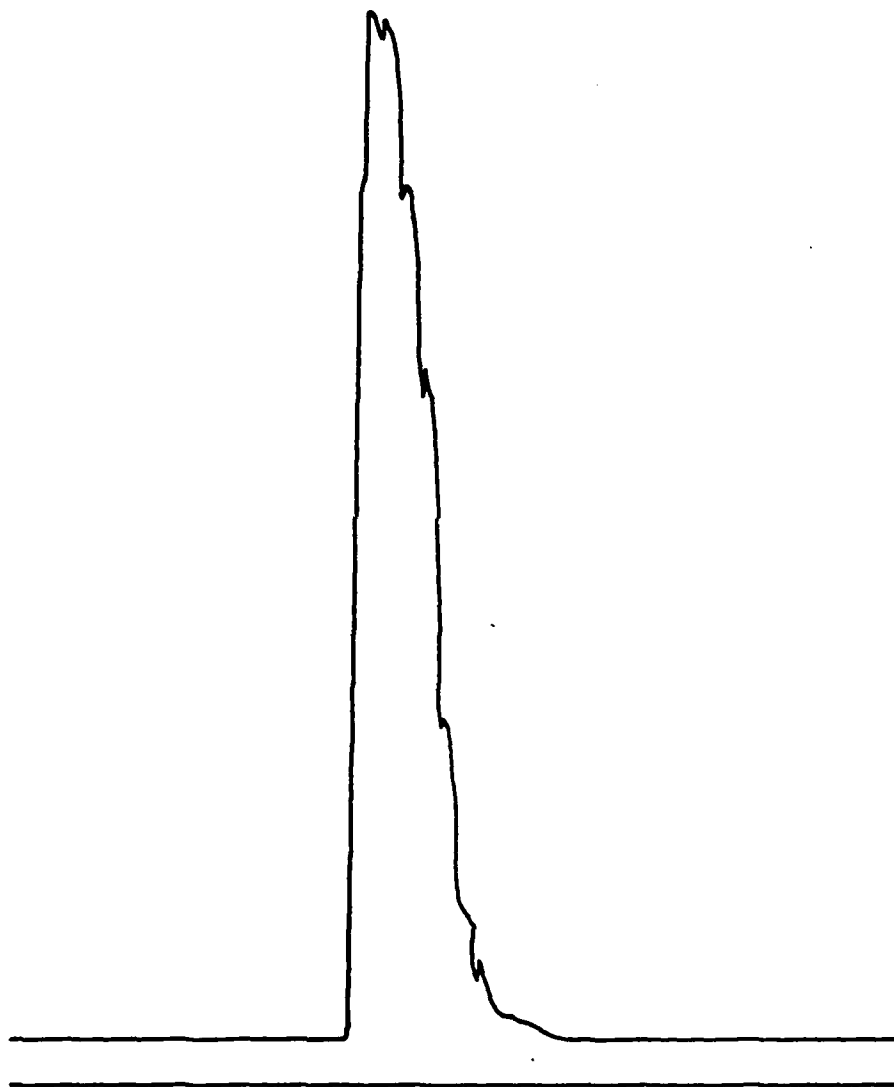
Figure 2.5. Microdensitometer scan of 20 ms exposure.
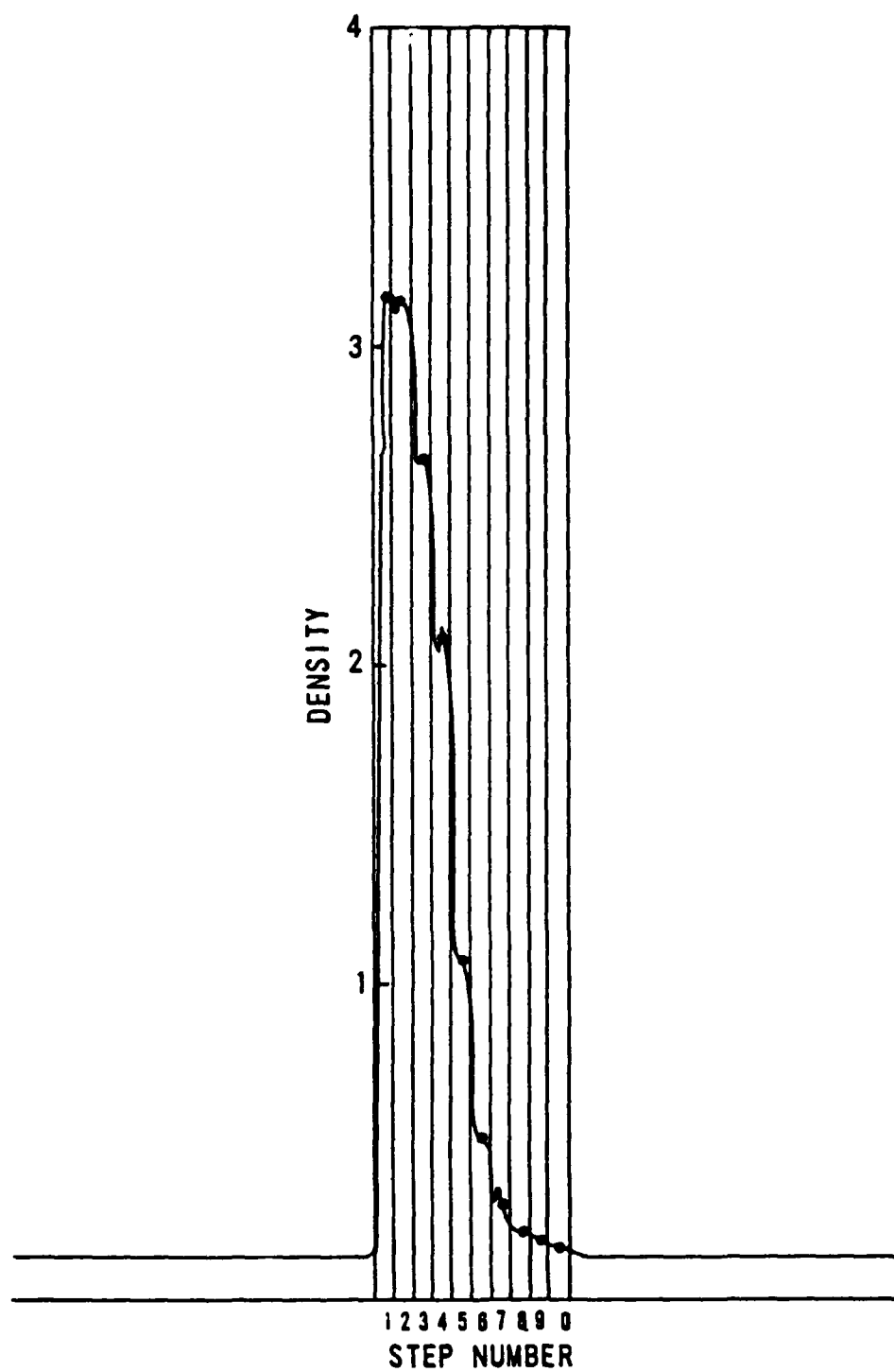
Figure 2.6. Grid overlay on data of previous
figure.

Table 2.1. Characteristic curve density values for various IR and visible exposure levels.

Step#	0 ms			5 ms			10 ms			15 ms			20 ms		
	0	.2	.4	0	.2	.4	0	.2	.4	0	.2	.4	0	.2	.4
1	3.3	3.0	2.1	3.5	3.3	2.8	3.5	3.4	3.0	3.5	3.4	3.6	3.5	3.4	3.2
2	3.3	2.9	1.9	3.5	3.3	2.8	3.5	3.4	2.9	3.4	3.4	3.0	3.5	3.4	3.2
3	3.1	2.3	1.2	3.4	3.0	2.0	3.4	3.1	2.2	3.4	3.1	2.4	3.5	3.3	2.7
4	2.7	1.7	.72	3.3	2.5	1.4	3.3	2.8	1.6	3.3	2.8	1.8	3.4	3.0	2.1
5	1.8	.82	.32	2.7	1.4	.64	2.8	1.9	.79	3.0	2.0	.45	3.1	2.2	1.1
6	1.0	.44	.19	1.9	.82	.33	2.2	1.1	.40	2.3	1.2	.48	2.5	1.4	.51
7	.51	.23	.14	1.2	.41	.19	1.4	.44	.23	1.6	.65	.26	1.8	.67	.30
8	.36	.19	.13	.79	.29	.17	1.0	.37	.19	1.2	.44	.20	1.3	.43	.21
9	.23	.15	.11	.48	.20	.13	.66	.26	.14	.72	.27	.15	.81	.29	.18
10	.18	.13	.11	.34	.16	.13	.38	.18	.14	.43	.20	.14	.47	.20	.17
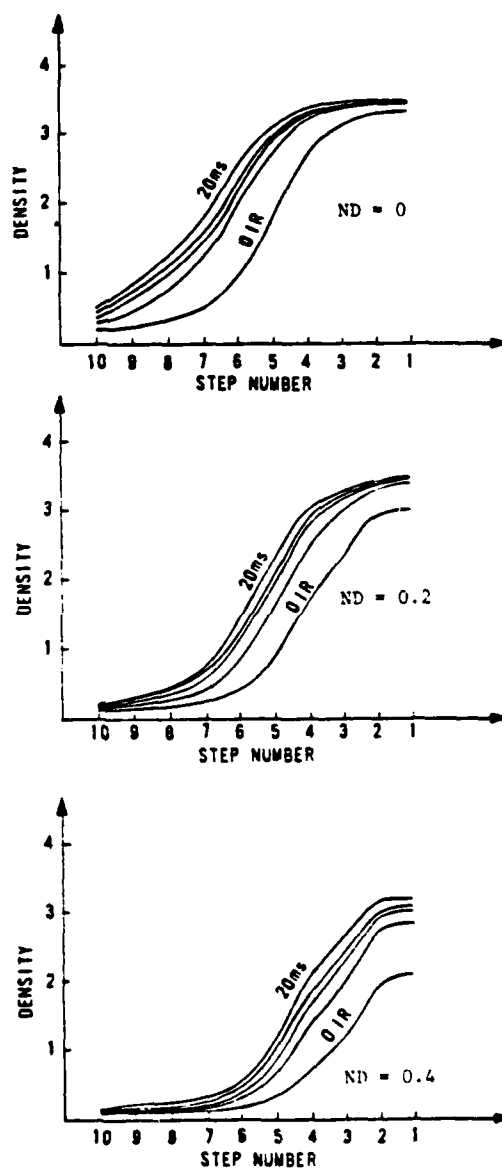
Figure 2.7. Characteristic curve shift as a function of
several IR exposure levels and neutral density.
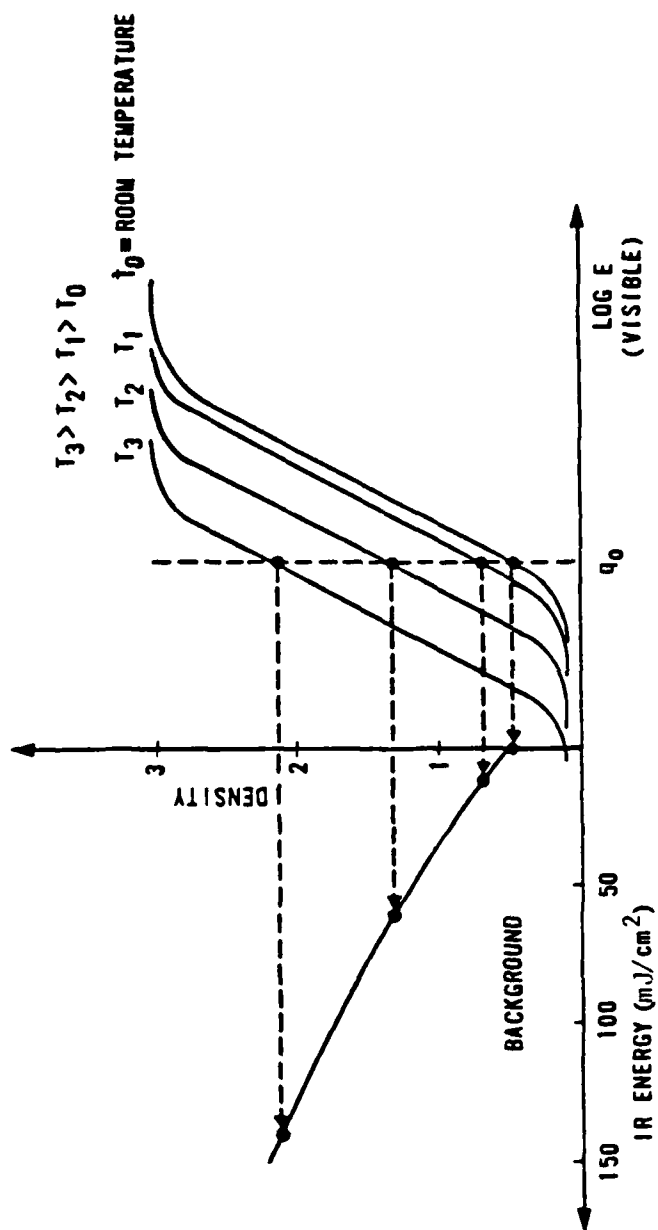
Figure 2.8. Relationship between DIRE and characteristic curves.

curve, this just provides us with the overall background density. This is also the *first point* on the DIRE curve. As we start depositing IR energy onto the film, the characteristic curve shifts to the left a distance proportional to the *amount* of this IR energy. The exposure q_e now operates on a different (and more sensitive part) of the characteristic curve; i.e., a *higher density* is achieved for the *same* visible input. Thus every *point* on the DIRE curve is associated with a particular characteristic curve.

CHAPTER 3

SPECTRAL SENSITIVITY

Introduction

In this chapter, we explore the effect of IRPP on the spectral sensitivity of Kodak 5369. Naor and his colleagues[6] did find a dependency for Kodak 5367, a blue-sensitive emulsion. However, their test was done in a piecemeal fashion, with limited spectral sampling. In our experiment, we wanted to subject an entire and continuous spectrum to the IRPP process in one operation. A procedure was therefore employed similar to that used in Chapter 2 for obtaining information on the characteristic curve. Instead of a step wedge being microimaged in the center of the gaussian IR beam pattern, a complete visible spectrum was imaged. Figure 3.1 illustrates the arrangement of the experiment. The visible arc in the Strobotac lamp was slitlike in appearance. It was also temporally and spatially stable when in operation. This arc source was placed in the focal plane of an input lens (singlet, double convex, 5 cm focal length, $f/1.3$). The resultant collimated beam was then incident upon a $60°$ spectrometer prism. The spectrally dispersed output beam was collected by a lens identical to the input

LASER
IR

30cm f/3 (Ge)

5.1cm f/2.7 (ZnSe)

SLIT-LIKE
STROBE SOURCE   NRC ELECTRONIC SHUTTER

5cm f/1.3

60°
SPECTROMETER   5cm f/1.3
PRISM

25.4cm f/9.1 (ZnSe)
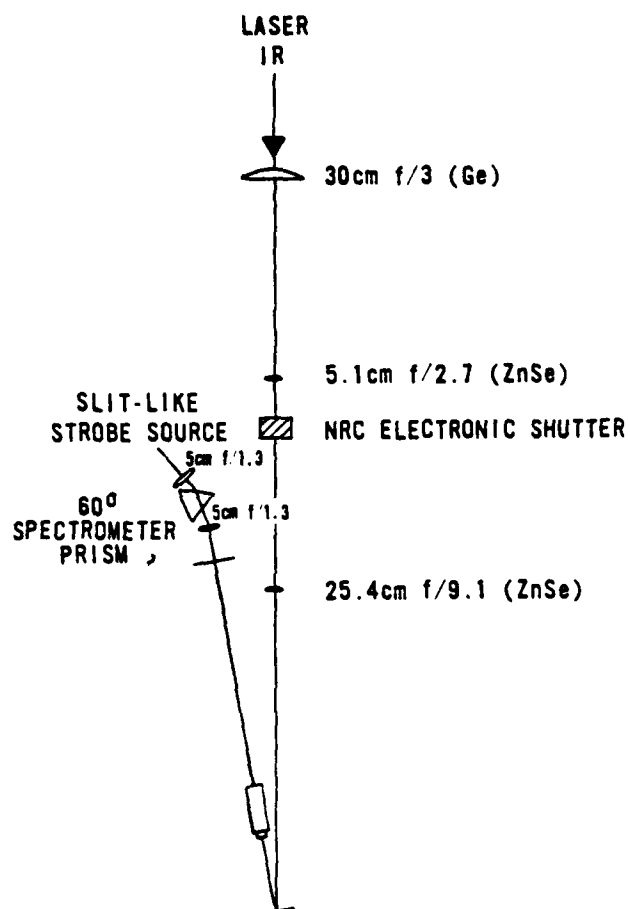
Figure 3.1. Experimental arrangement for
measuring film spectral IRPP
sensitivity.

lens. The arc spectrum was displayed in the focal plane of this
output lens. A microscope was then used to image (and substantially
demagnify) this spectrum onto the film plane. The microimage was in
the IR gaussian footprint. The critical step was in calibrating this
microimage. We needed to know not only intensity as a function of
wavelength, but also wavelength as a function of position in the
spectrum image. We describe the latter calibration first.

Calibrating Wavelength

The microscope in Figure 3.1 was turned around 180°. A 1X
objective was used along with a Gamma Scientific fiber probe scanning
eyepiece to view the spectrum in the output lens focal plane. The
fiber would make a horizontal scan through the spectrum parallel to
the electrode shadow line, and with a predetermined vertical offset.
Another auxiliary reference shadow line was placed vertical to the
fiber scan path to provide a horizontal position reference (HPR).
The latter would be needed to relate microdensitometer and radiometer
scan data. (This auxiliary reference was a human hair placed in the
focal plane of the output lens.) These various references relative
to the fiber scan are illustrated in Figure 3.2. The output end of
the fiber scanning probe was fed into a grating monochromator, which
in turn fed a photomultiplier tube (PMT) radiometer. The signal from
the radiometer controlled the Y-axis of an X-Y recorder. The X-axis
was controlled by a voltage signal from the fiber probe proportional
to its horizontal scan position. The overall experimental
arrangement is illustrated in Figure 3.3. The procedure was as
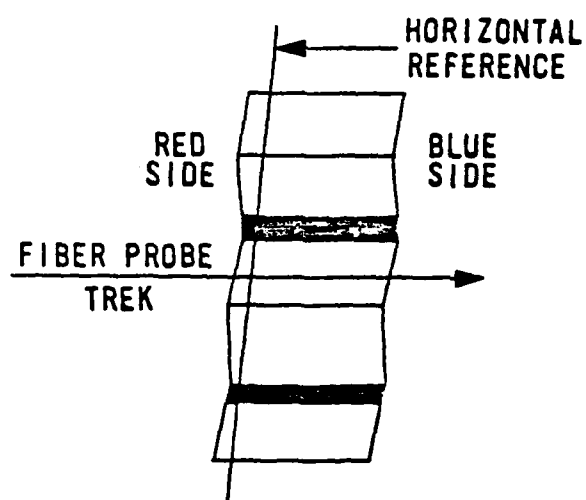
Figure 3.2. Illustration of spectrum image with
features identified.
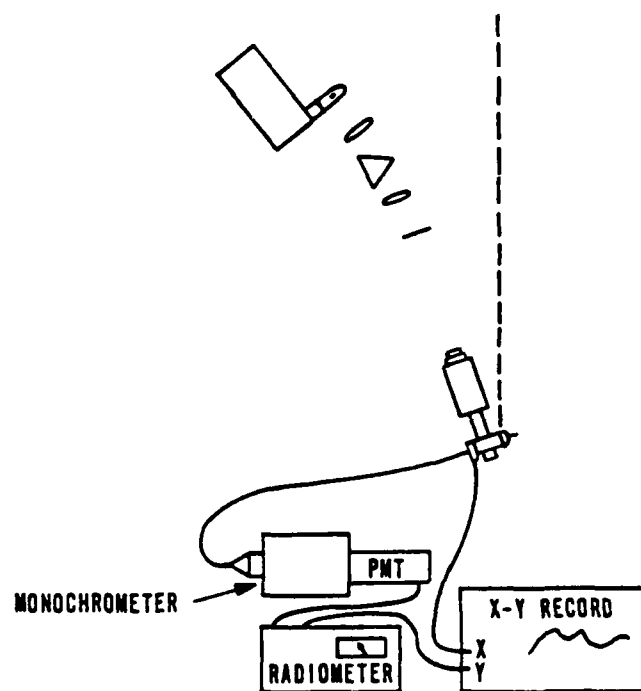
Figure 3.3. Optical arrangement for calibrating
spectrum.

follows. For a given lateral position of the fiber probe, the wavelength selector on the monochromator was tuned until a peak reading was obtained from the radiometer. This identified a particular probe position with a specific wavelength. This process was repeated until the entire spectrum had been suitably sampled. We emphasize that the monochrometer was used only to identify a wavelength selected by the relative position of the fiber probe in the spectrum. In this way, the horizontal axis of the chart recorder was wavelength calibrated. Figure 3.4 shows a plot of probe position vs wavelength.

Calibrating Spectral Intensity

With the wavelengths properly identified on the chart paper, we now needed the relative spectral distribution. The monochromator was removed, and the output end of the fiber probe was coupled directly to the PMT. The signal from the radiometer once again drove the Y-axis (this time continuously). The results are shown in Figure 3.5. The dip in the spectrum at the left is the HPR. Note that this reference line was placed well into the red, into a spectral region for which Kodak 5369 was not very sensitive. We did not want the HPR to obscure interesting data in the realm where the film had the bulk of its sensitivity. The spectral plot of Figure 3.5 is not the final product. The "radiometer system" still needed to be calibrated, not absolutely but relatively.

The spectral response of the PMT is shown in Figure 3.6. The spectral transmission of the fiber probe scanning eyepiece and
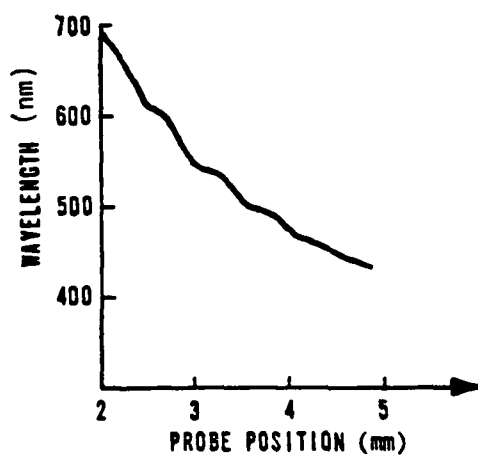
Figure 3.4. Plot of probe position
vs wavelength.
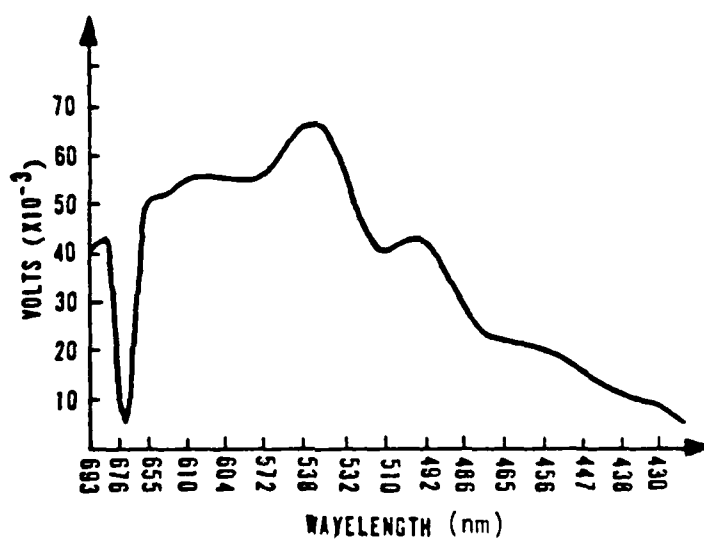
Figure 3.5. Uncalibrated relative spectrum.
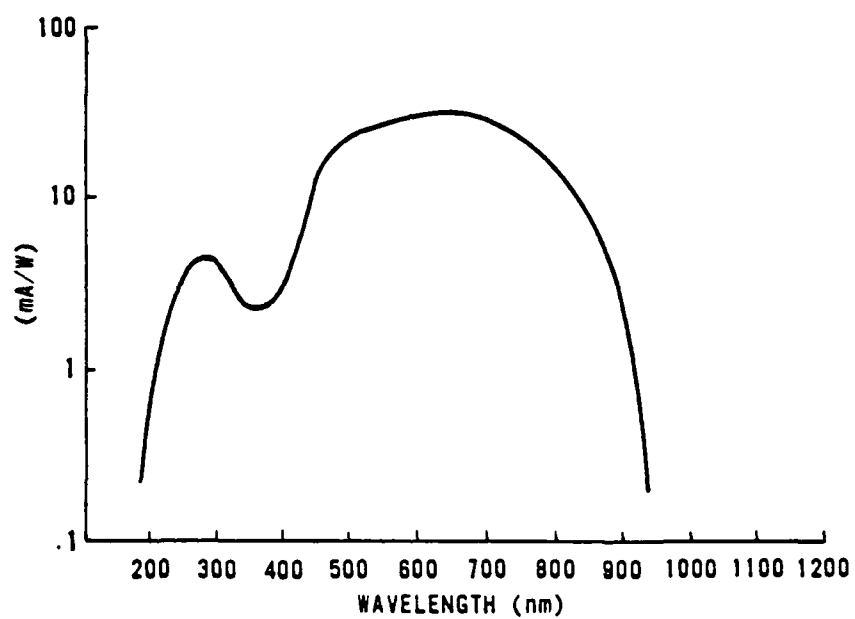
Figure 3.6. PMT spectral response.

coupler is shown in Figure 3.7. Applying these to Figure 3.5, we obtain the corrected relative spectral distribution, Figure 3.8, in the plane of the scanning eyepiece. This is essentially the distribution incident upon the film.

Film Test

We now turn our attention to the film record. IR exposures were made for 0, 5, 10, 15, and 20 ms respectively. At the completion of this exposure, the microimage of the spectrum was flashed into the center of the gaussian footprint. A series of neutral density (ND) filters was employed in the visible path to provide a range of offset density levels for this exposure. The film was developed so that the film processing of all cases took place at the same time and in the same manner. The microimage was 2 mm long with the spectrum running horizontally 0.75 mm in width. Figure 3.9 is an enlargement made from the ND = 2, 20 ms case. The clear horizontal bars are the electrode shadows. The clear "vertical" line on the right is the HPR. All test images were scanned on a PDS microdensitometer (10-μm sampling aperture). A typical scan is shown in Figure 3.10 for the ND = 2, 0 ms case. The dip in the curve at the right is the HPR. We now had to identify points on the X-axis of the microdensitometer scan with the appropriate wavelengths. Those wavelengths were designated on the X-Y recorder chart (cf Figure 3.5). The magnification factor connecting the two data outputs had to be established. This was done by measuring the center-to-center vertical separation between the electrode shadows both in the aerial
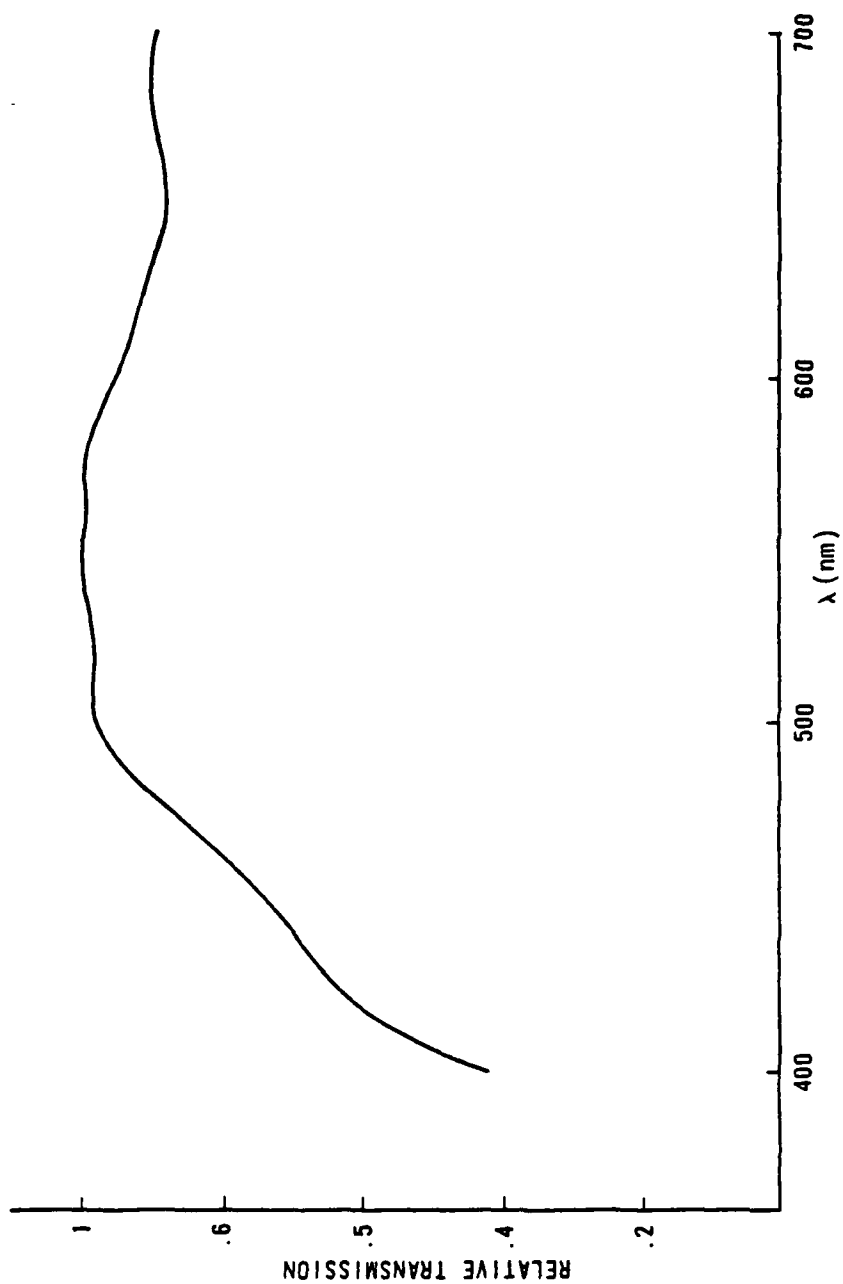
Figure 3.7. Spectral transmission of fiber probe and coupler.
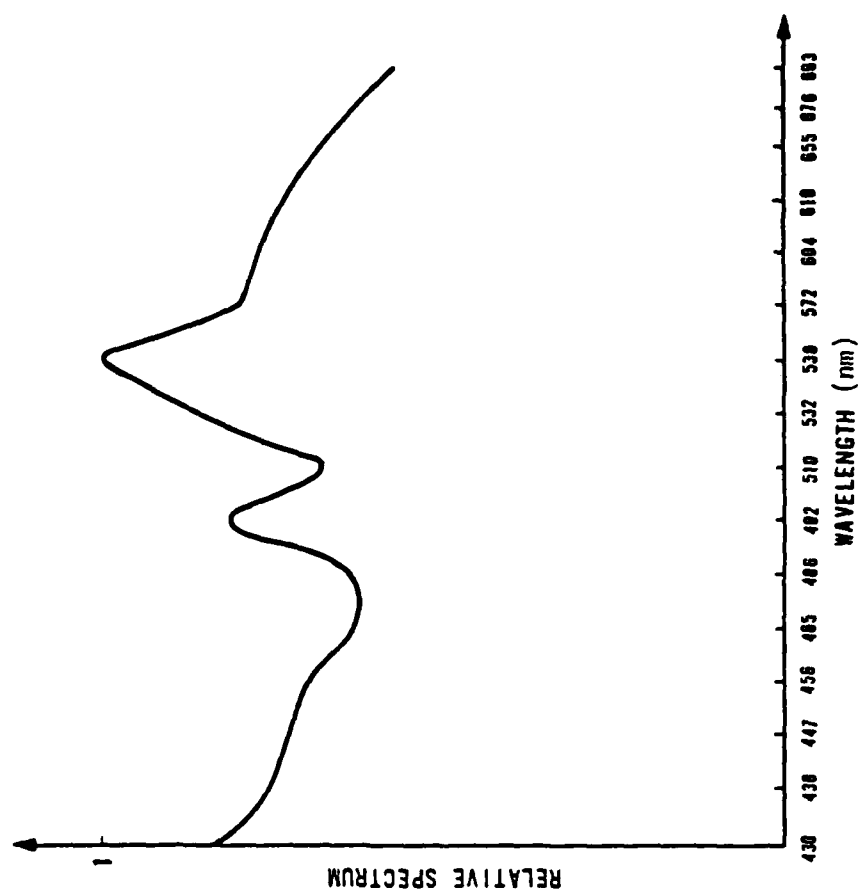
Figure 3.8. Corrected relative spectrum.

Figure 3.9. Negative of spectral microimage.
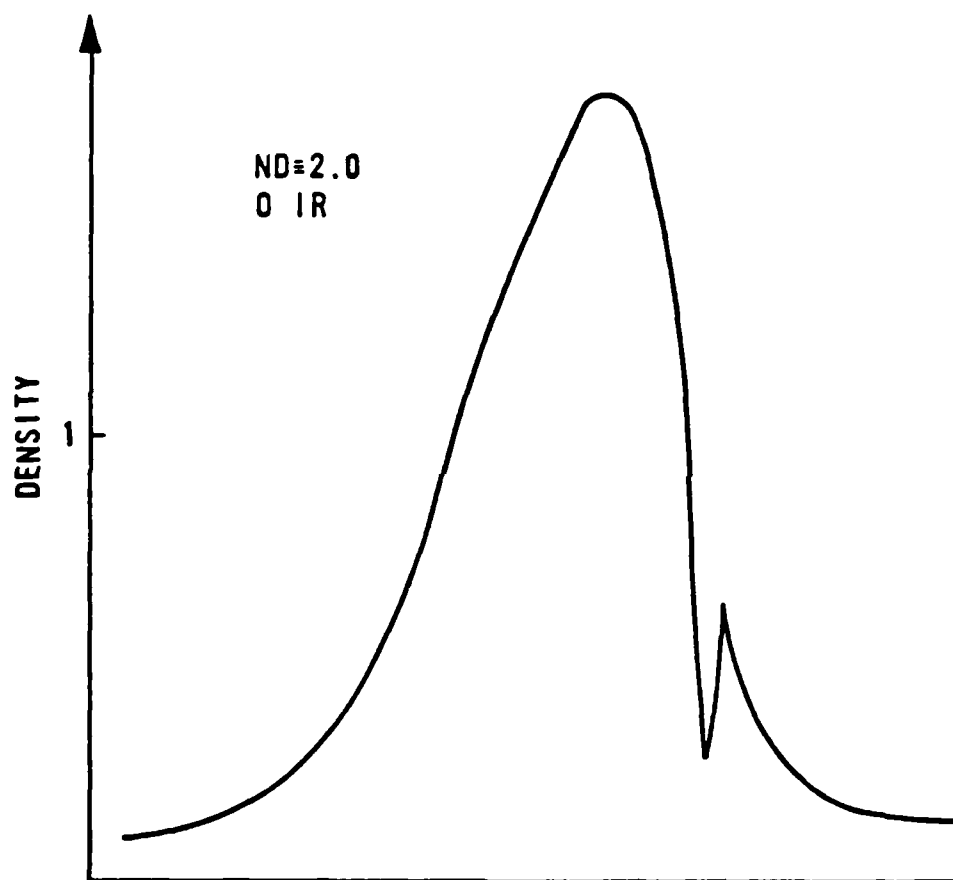
Figure 3.10. Microdensitometer scan of spectral microimage for ND = 2, 0 ms case.

image (scanned via the fiber probe with output onto the X-Y chart) and comparing this with the same measurement mode on the film via the microdensitometer.

Discussion

Figure 3.11 shows the combined microdensitometer outputs (left) and DIRE curves (right) for a range of IR exposures(0 to 20 ms) and visible exposure levels. (Note that the reference dip was used to align the various scan cases.) The wavelength positional information is provided along the X-axis of the microdensitometer traces. To determine the DIRE curve, an array of vertical lines was erected at specific wavelengths on the microdensitometer scans. Points of intersection were then located. These data are tabulated in Table 3.1. Using Table 3.1, plots of density vs IR energy (time) for a given wavelength were obtained. The DIRE plots in Figure 3.11a pretty much parallel one another. They would not do so if there were spectral sensitivity variations. Consequently, we are not seeing any significant wavelength dependency here, at least not over the energy range explored. This implies that the effect IRPP has on the film's spectral sensitivity curve is simply to induce a vertical shift, as illustrated in Figure 3.12. DIRE results shown in Figure 3.11b are somewhat similar, but now there is a hint of divergence at the shorter wavelengths. Note that the lower density values are in the toe region of the characteristic curve (cf Figure 3.13). A spectral test was conducted so that most of the density values fell well within the toe region. This information is provided in Figure 3.11c.
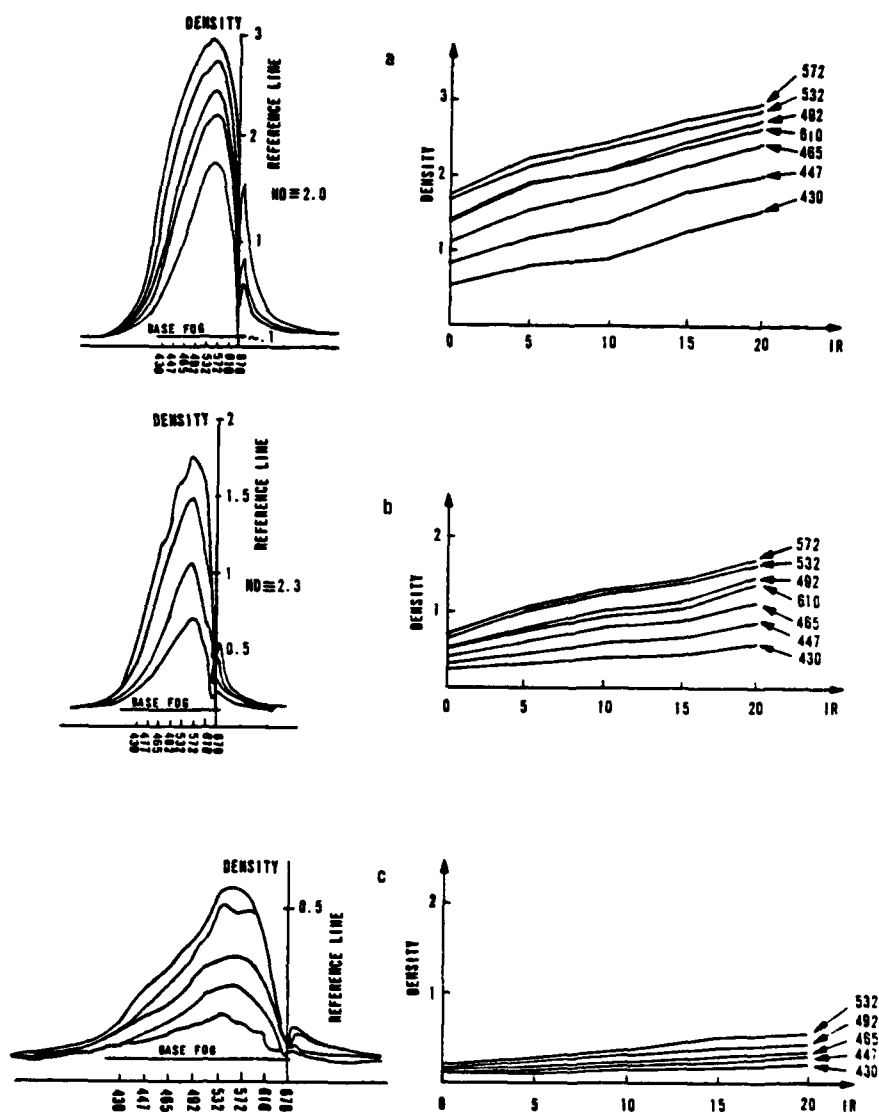
Figure 3.11. Spectrally calibrated microdensitometer scans (left) and spectral DIRE curves (right) as a function of IR exposure level, and background density.

Table 3.1. Density values as a function of visible wavelength, IR
            and visible exposure levels.

ND = 2.0

λ	0	5	10	15	20
430	.516	.804	.888	1.284	1.572
447	.816	1.176	1.368	1.812	2.040
465	1.116	1.548	1.794	2.160	2.442
492	1.398	1.884	2.088	2.454	2.830
532	1.680	2.130	2.352	2.640	2.892
572	1.758	2.244	2.436	2.754	2.952
610	1.428	1.896	2.070	2.400	2.658

ND = 2.3

λ	0	5	10	15	20
430	.240	.308	.404	.444	.588
447	.305	.440	.604	.680	.884
465	.400	.588	.816	.896	1.152
492	.516	.788	1.040	1.172	1.480
532	.620	.992	1.264	1.408	1.648
572	.704	1.036	1.296	1.452	1.712
610	.512	.744	.944	1.052	1.408

ND = 2.6

λ	0	5	10	15	20
430	.104	.104	.144	.152	.186
447	.116	.136	.196	.216	.276
465	.137	.170	.232	.284	.334
492	.162	.226	.302	.384	.420
532	.192	.266	.358	.512	.542
572	.168	.272	.372	.502	.556
610	.120	.194	.284	.378	.424
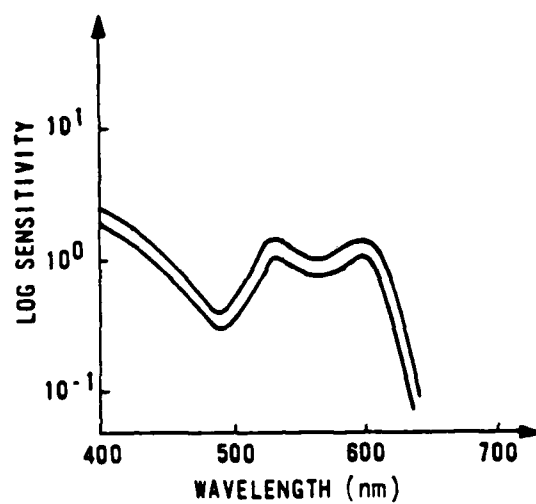
Figure 3.12. IRPP induced sensitivity
shift.

5369
PROCESSING
D-72
3 min
68° F
AGITATION
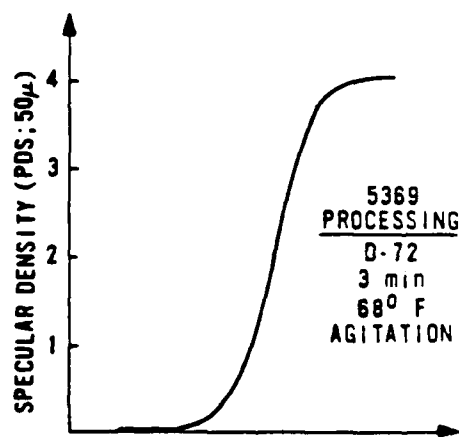
Figure 3.13. Characteristic
curve (specular)
for 5369.

There is a definite divergence in the DIRE plots. But we reiterate that this is not a wavelength sensitivity shift, but a variation due solely to operation in the nonlinear portion of the characteristic curve.

Naor et al.[6] found dramatic divergence in their data (cf Figure 3.14). However, they were using a different emulsion (blue sensitive 5367), the thickness of which is almost a factor of 4X that of 5369. Furthermore, they were depositing IR energy much faster. Their laser pulse times were on the order of 0.1 microsecond. Naor provided no information on development conditions. It is assumed he used Kodak recommended processing and calibrated his microdensitometer for diffuse density readings (cf Figure 3.15). With reported background densities between 0.4 and 0.5, he should be operating in the linear portion of the characteristic curve. Toe effects should not have been influencing his data. Although no wavelength dependency was found for the film we employed, it appears (from Naor's work) that this cannot be made into a generalization. Until the difference in the 5369 and 5367 results can be definitely pinned down or attributed to some variance in film parameters, the IRPP spectral dependence is something that needs to be measured for each film and each condition of operation.

64
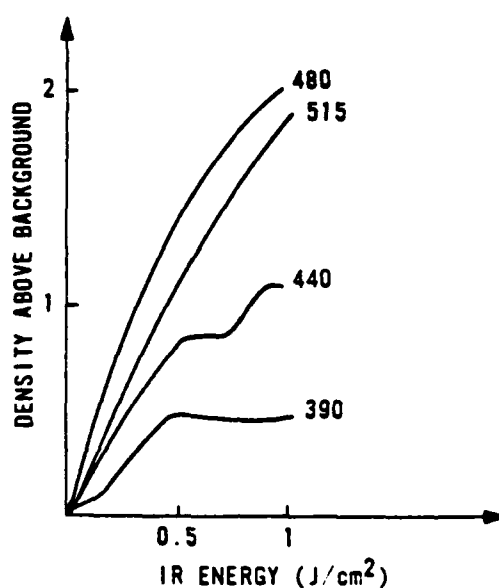
Figure 3.14. Results from Naor's
test.
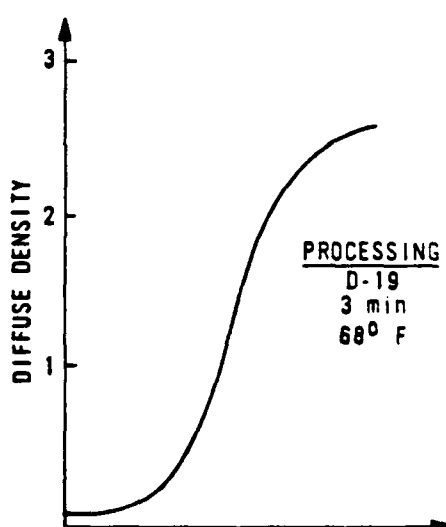
Figure 3.15. Characteristic
curve (diffuse)
for 5367.

CHAPTER 4

FILM TEMPERATURE

Introduction

To gain some understanding of the mechanism(s) responsible for the IRPP phenomenon, it is important to know exactly how hot the film gets during the process. For example, if thermal expansion of crystal grains plays an important role, then it is obvious that film temperature will be a key parameter of interest. It is critical to be able to measure this temperature on the time scale of the phenomenon itself, and in the local region in which it is occurring. The test configuration that allowed us to do this is illustrated in Figure 4.1. The IR path is the same as before. The visible arm, however, has been _replaced_ with a sensitive cooled IR detector system. The purpose of this detector is to monitor the _thermal_ radiation emitted by the film as it is heated by the CO_2 (10.6-μm) laser beam. This transient signal is then compared to thermal radiation signals from two other film samples held at constant but different temperatures. Such a comparison enables us to determine the transient film temperature.

LASER
IR

30 cm f/3 (Ge)

5.1 cm f/2.7 (ZnSe)

NRC ELECTRONIC SHUTTER

ALIGNMENT
TELESCOPE

25.4 cm f/9.1 (ZnSe)

PbSnTe
DETECTOR

CHOPPER

10 cm f/2.5
(ZnSe)

TARGET CARRIER

T_2 T_1
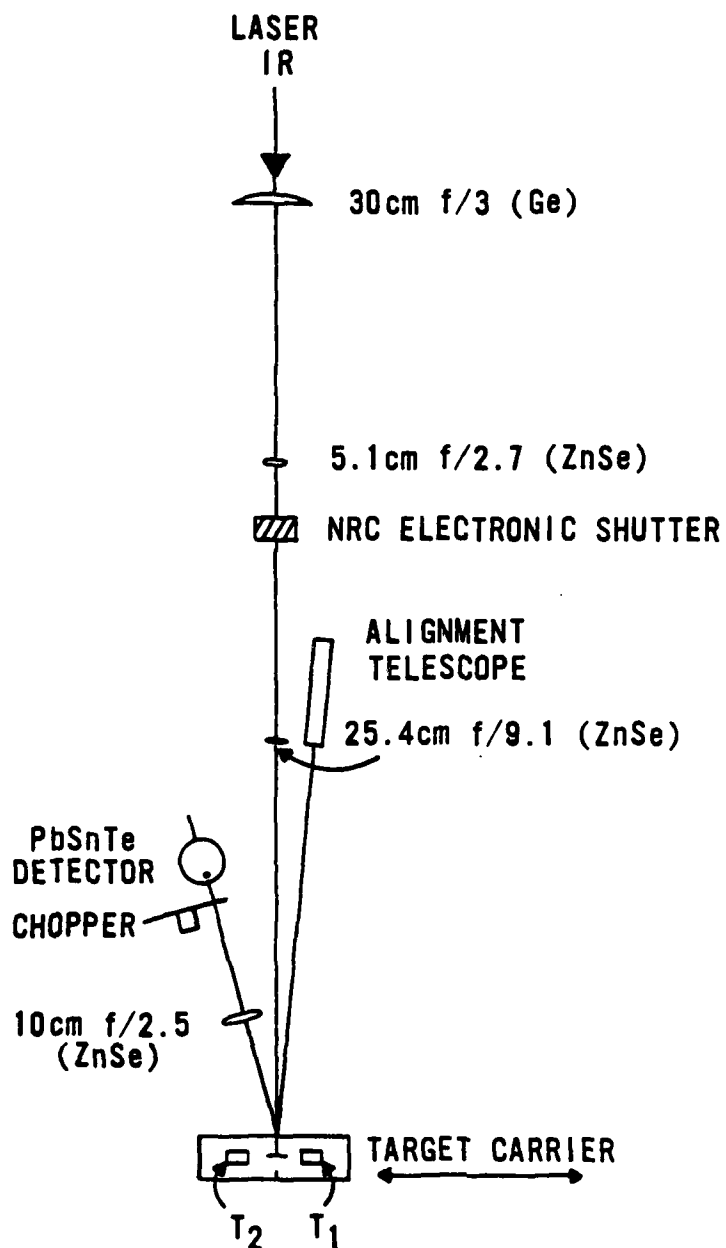
Figure 4.1. Experimental configuration for film
temperature test.

Discussion of Experimental Setup

The plane of the detector element (PbSnTe, 1-mm diameter) is conjugate to the film target plane at unit magnification. Hence, the detector image on the target has an effective sampling aperture of 1 mm and is centered on the gaussian beam footprint. A radiometric scan of the gaussian beam footprint is shown in Figure 4.2 with the 1-mm sampling aperture indicated. The central film target (Figure 4.3) alone is subject to laser irradiation. It is mounted so as to approximate the manner in which film is held in the 35-mm camera that we have been using for exposure tests. (For example, the backing plate is of the same material and thickness as that in the camera. The metal washer in front represents the format. The film sample is held between the two by pressure from the bottom clamp.)

The side targets in Figure 4.3 are resistive heater elements (Dale, wire wrapped power resistors Model RH10). The front surface of each has three separate target areas: a polished strip, a lamp black strip, and a film strip (emulsion out) that is cemented to the heater surface. The idea was to use these various strips to measure emissivity. The temperature of the heater surface was measured with an Omega Thinfilm RTD element (2 mm square, 1 mm thick). These are designed to accurately measure surface temperature. The resistance of such devices is temperature dependent. Resistance is measured and the temperature is determined from a calibration chart. The RTD probe was cemented to the polished part of the heater surface as can be seen in Figure 4.3. (Note: A colleague, Mr. Dave Holmes,
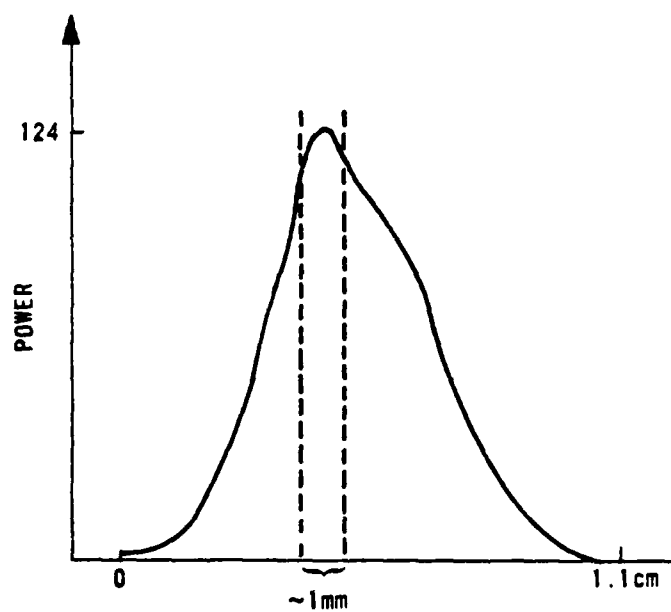
Figure 4.2. Radiometric scan of IR test beam.
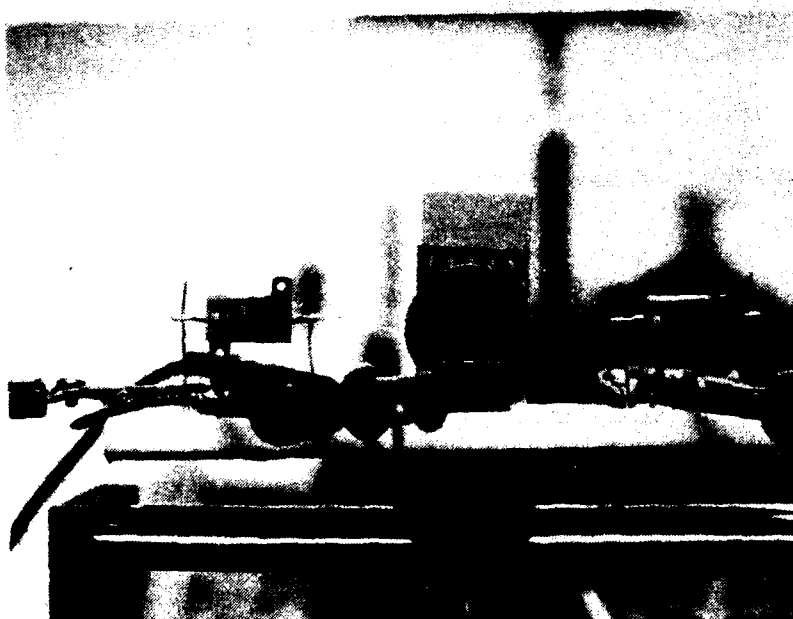
Figure 4.3. Photograph of target board.

determined that the difference in surface temperature between the polished strip and the film strip amounted to only 1° or 2°C.) One side target was held at a high steady-state temperature and the other at a low steady-state temperature, so that the difference would span the temperature range seen by the central target. The surfaces of all three targets lie in the same plane. They are mounted on a common base that is capable of lateral motion. This allows the thermal detector (which is immobile) to view any one of the three targets. Positioning of the targets for detector viewing was accomplished with the aid of an alignment telescope (Figure 4.1) whose crosshairs had previously been centered on a laser burn pattern.

The alignment of the thermal detection path was a bit more complicated. The centers of the detector, lens, film targets, and laser gaussian footprint all had to be set at the same height above the optical table. The detector and film target had to be on the optical axis of the lens. The latter was first roughed in. A burn pattern was obtained on white thermal-sensitive paper at the target position. This burn target was then strongly illuminated by a CW white light source. The detector (which was observable behind its transparent ZnS window) was moved axially until a sharp visible image of the burn pattern was seen on the detector plane. The detector package was then tweaked laterally until the burn mark image was centered on the detector element. The detector was then moved axially away from the lens a calculated distance corresponding to the

10.6-μm focus position (the amount of this shift is derived in Appendix 1). The burn paper was removed. In its place was set a graphite block whose front surface was in the target plane. The chopper (indicated in Figure 4.1) was now utilized for the first time. The detector was AC coupled; consequently, it was necessary to modulate the incoming DC signal from the scattered CO_2 laser radiation. The detector package was once again tweaked axially and laterally until the chopped signal (viewed on an oscilloscope) was maximized. When this was achieved, the thermal detector arm was considered aligned.

Test Procedure

The graphite block was removed, and the central target was replaced. The chopper was disabled, the blades set so as not to interfere with the detection path. IR exposures were made between 5 and 35 ms at 5-ms intervals. Each exposure took place on a fresh film sample. This was necessary because even the smallest exposure altered the coloration of the emulsion surface, and greater exposures dimpled it. The side targets, modulated by the chopper, were viewed before and after each test. A typical test result is shown in Figure 4.4. The "shark fin" is the transient data from the laser exposure. As the electronic shutter opens, it produces a small vertical step initiating the data run. The detector is seeing scattered 10.6-μm radiation. Thereafter, we see the contribution from broadband thermal emission from the film as it heats up. This latter signal is above the diffuse laser signal. When the electronic shutter closes,
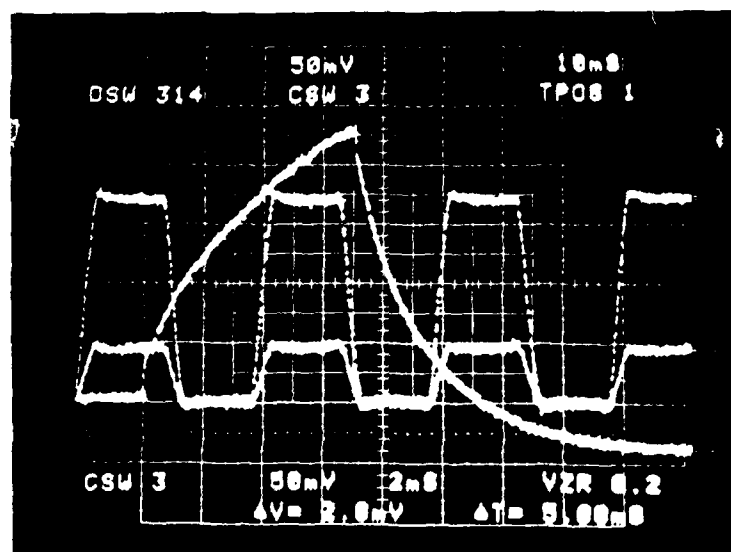
Figure 4.4. Oscilloscope film temperature data sample.

the scattered laser signal is immediately lost. This is seen on the data run as a small vertical drop right after the peak of the "fin." The signal level at this point represents the maximum temperature of the film. We then witness classical exponential decay as the film cools off. Note, however, that the signal does not return to "zero" but actually flattens out well below the "room temperature" level. This is due to a change in the emissivity of the film and is the main reason that new film samples had to be used for each test. The two square wave patterns in Figure 4.4 are the signals from the respective side target films, one at 124°C and the other at 59°C. Note that the side targets suffered no apparent emissivity change. Throughout the test series, the laser power was continually monitored for power stability. A compilation of all test runs is presented in Figure 4.5. Again, the "shark fin" is the transient data from the central target. The horizontal lines denote the temperatures of the side targets. The peak thermal temperature is also indicated for each IR exposure time.

Upon completion of the thermal tests, another radiometric scan was made, and was compared to the one taken before test initiation. The results were the same as already shown in Figure 4.2. In addition, an IRPP test was run for the same series of IR exposure levels. The film received our standard processing (D-72, 3 min, 69°F, agitation). The gaussian images were scanned through the center with a microdensitometer (50-μm square sampling aperture). The microdensitometer traces are displayed in Figure 4.6. At
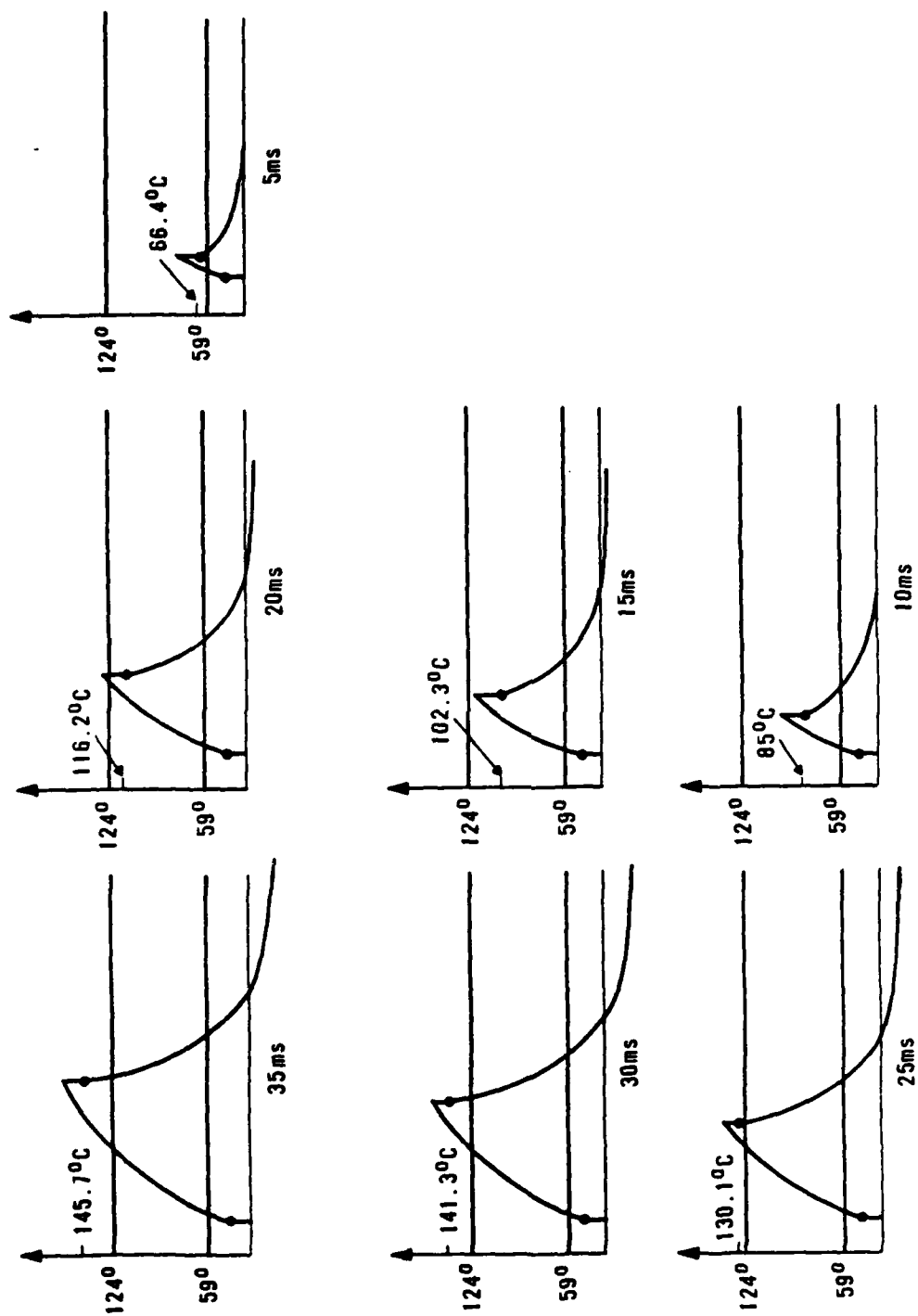
Figure 4.5. Composite of all film temperature test runs.
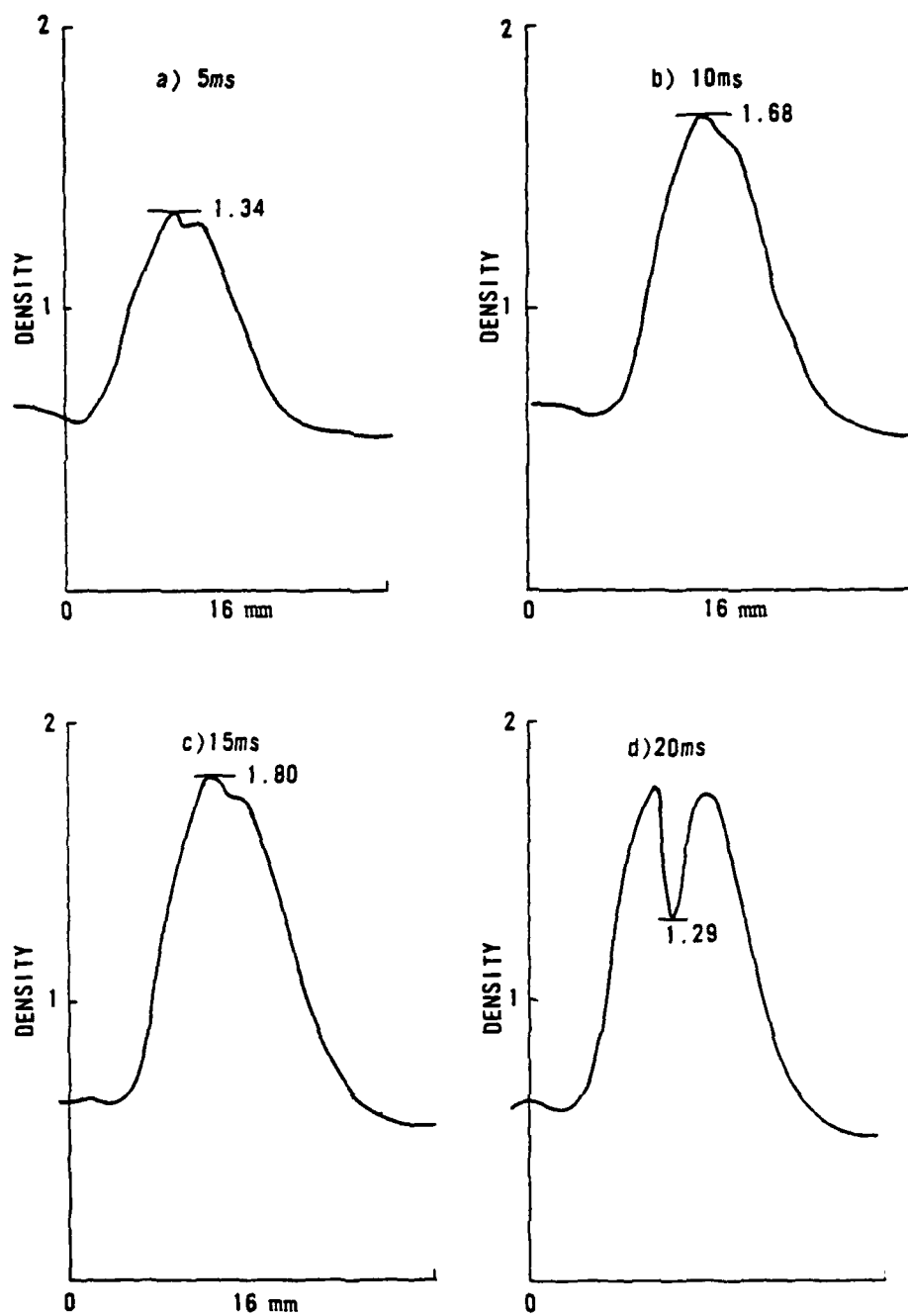
Figure 4.6. Microdensitometer scans of IRPP
correlation data.
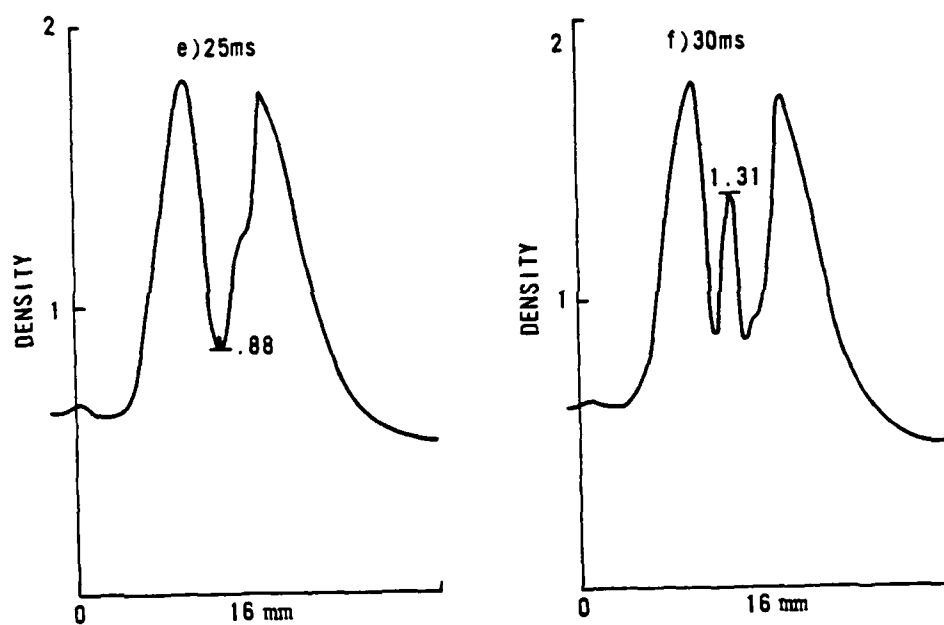
Figure 4.6. continued

approximately 15 ms, a density ceiling of 1.8 is reached. The 20 and 25 ms cases show strong "reversal" effects. At about 25 ms, the central part of the gaussian is on the rise again. This is obvious in the 30 ms case. This _second_ reversal effect is due to emulsion damage. The energy being dumped on the film in this region is actually charring the emulsion. A first cut correlation among film temperature, IR energy, and film density is presented in the first four columns of Table 4.1. (Refinements are needed, and will be discussed shortly.) For the first time since the discovery of the IRPP phenomenon, we have a good idea of how hot the film actually gets on the time scale of the event! It is difficult to compare these results with the work of Naor et al.[6] They did not determine film temperature directly. Rather, they used bulk steady-state heating of the film (by pressing it against a hot plate). This was not a measure of the IRPP temperature effect at all. Their highest steady-state temperature was $60°C$, which caused a density above background, $\Delta D = 0.51$ (at 515 nm). Our lowest transient temperature was $66°C$, resulting in a $\Delta D = 0.70$ for a 0.43 J/cm^2 energy input (and broadband visible exposure). They estimated a ΔT of $30°C$ for each 0.18 J/cm^2 increase in energy. We see a ΔT of $36°C$ for 0.85 J/cm^2 between the 5 and 15 ms cases. Such comparisons are shaky because vastly different films were used. Furthermore, we deposited IR energy on a time scale four orders of magnitude longer than Naor et al. did. It would not be at all surprising if IR reciprocity failure played a significant role over such a span of exposure times.

Table 4.1. Corrected correlation table comparing IR energy, temperature, and density.

IR exposure, ms	IR energy, J/cm^2	Density	Measured Temperature, $C°$	Corrected Temperature, $C°$
5	.43	1.34	66.4°C	55.8°C
10	.85	1.68	85.0	75.2
15	1.28	1.80	102.3	98.6
20	1.71	1.29	116.2	113.6
25	2.13	0.88	130.1	135.6
30	2.56	1.38	141.3	152.7
35	2.99	—	145.7	158.9

Temperature Adjustment

As mentioned, refinements to the temperature data in Table 4.1 are needed. The effects of averaging over the different-sized sampling apertures of the radiometer, microdensitometer, and thermal detector must be taken into account. The change in film emissivity as a result of the IR exposure must be considered. Finally, the _shift_ in the film's "blackbody" emission curve as film temperature increases must be examined relative to the spectral response of the detector. The effect of operating off-normal to the film plane, and of the detector's lying at the 10.6 μm image plane (instead of a best focus for broadband thermal radiation) can be neglected since these conditions were the same for all three targets.

In Figure 4.7, we have plotted the transmission spectrum of the IRTRAN 2 window, the IRTRAN 4 lens, the relative spectral sensitivity of the Barnes PbTnTe detector, and the blackbody spectrum for T = 273 and 400°K (all plotted against a _linear_ wavelength scale). In the region of interest (as defined by the detector), the effect of such a temperature change is essentially a vertical shift of the blackbody curve, which is fairly flat in this region. Consequently, no spectral correction to the data in Table 4.1 is needed. (We should mention that when we compared emissivities of the polished metal, lamp black, and film surfaces on the side targets, we found the film providing the highest signal (Figure 4.8). Our lamp black coating, which looked good by eye, showed pin-sized holes all over, down to the bare metal, when viewed under a microscope.)
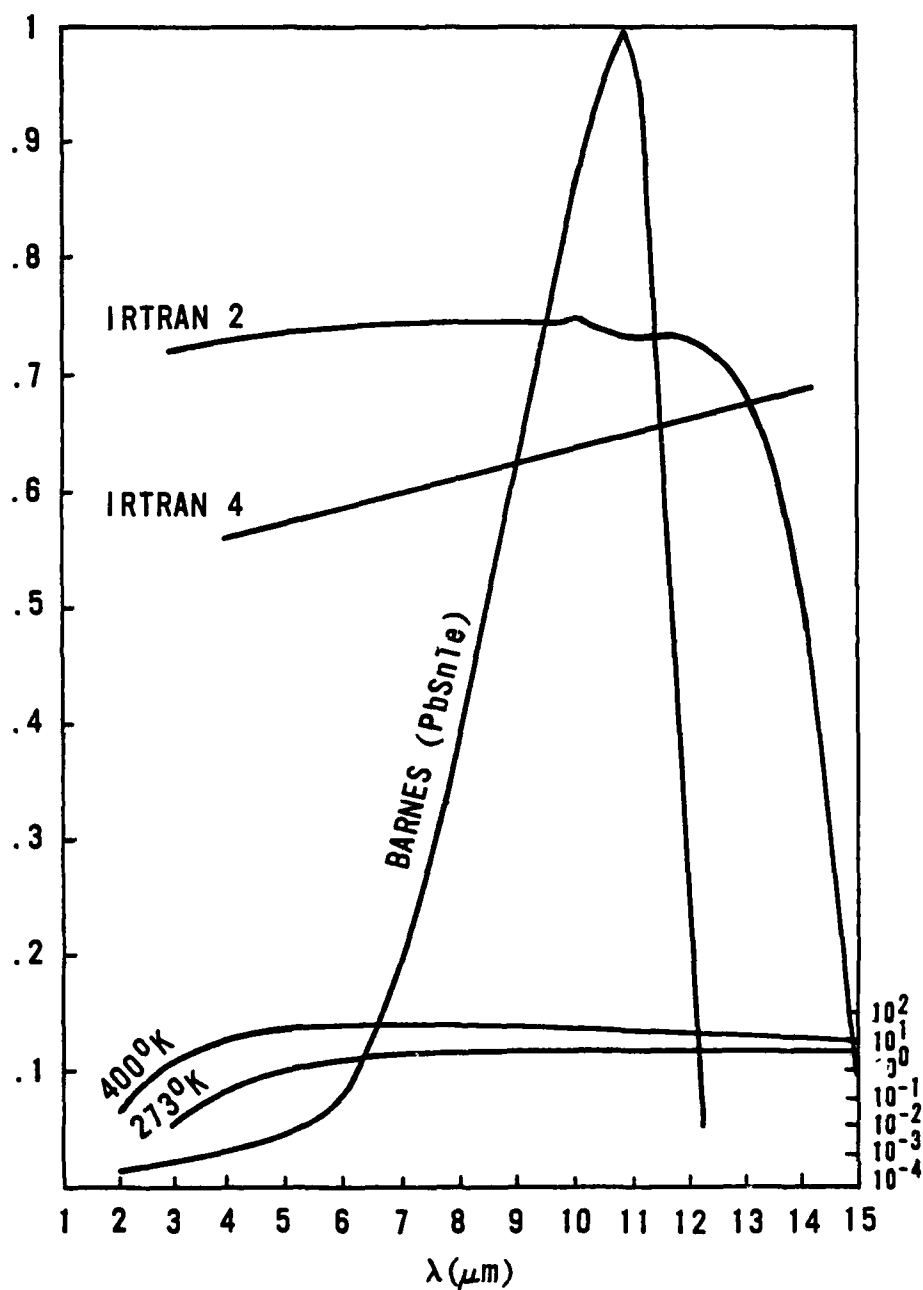
Figure 4.7. Spectral data on detector, materials, and blackbody curves.

T_1-LOW TEMPERATURE

POLISHED METAL FILM LAMP BLACK

T_2-HIGH TEMPERATURE

POLISHED METAL FILM LAMP BLACK
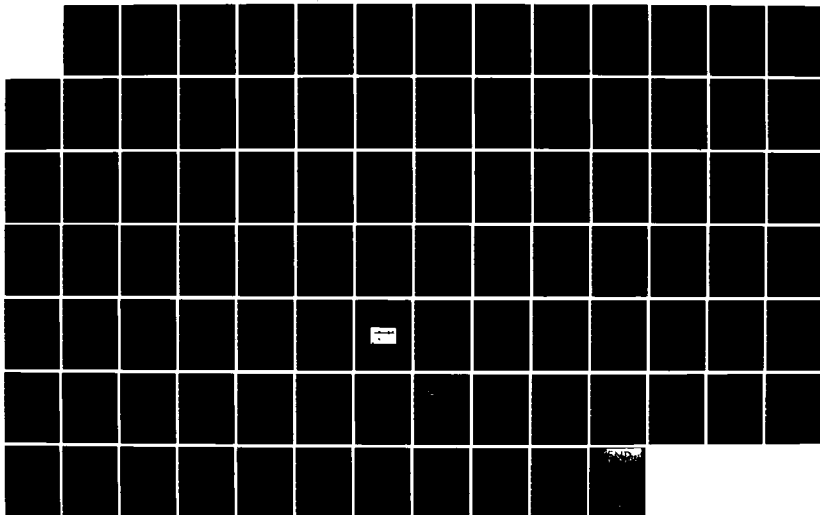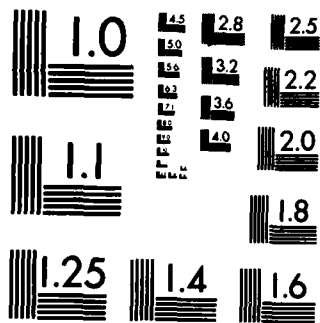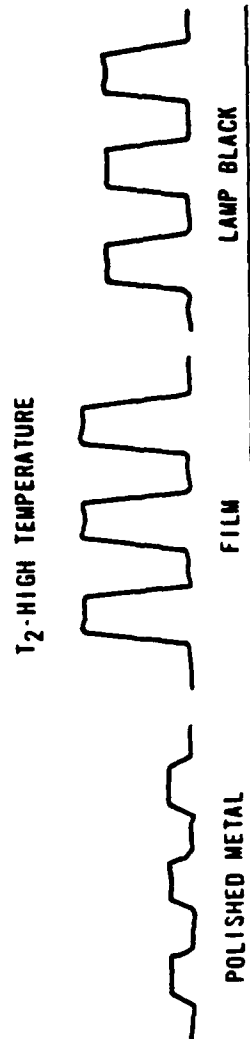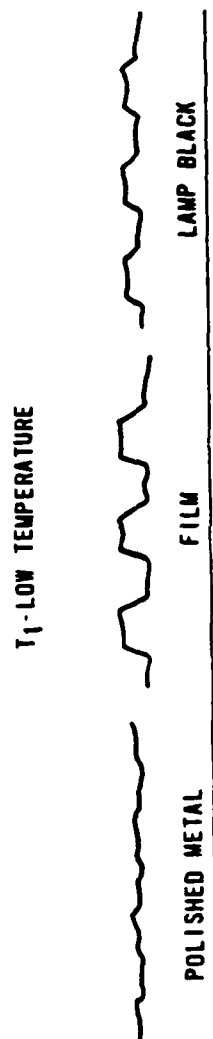
Figure 4.8. Relative emissivities of film emulsion lamp, and polished metal.

If we assume, for the moment, that our laser was providing a perfect gaussian footprint at the film plane (and assumming heat maps linearly with local IR irradiance levels), we can write the temperature distribution of the film as

$$T(r) = T_0 \text{ Gauss } (r/b) \qquad (1)$$

where

$$T_0 = \text{peak temperature Gauss } (r/b) = e^{-\pi (r/b)^2} \qquad (2)$$

With the thermal detector, we do not measure T_0 but some average temperature, $\overline{T}$, defined by

$$\overline{T} = \int_0^R \frac{2\pi r dr \ T(r)}{A} \qquad (3)$$

Recalling that $\int_0^x e^{ax} dx = \frac{1}{a}[e^{ax} - 1]$, $\overline{T}$ can be written as

$$\overline{T} = \frac{\pi T_0}{A} \left\{ \frac{-b^2}{\pi} \left[e^{\frac{-\pi R^2}{b^2}} - 1 \right] \right\} \qquad (4)$$

where

$$b = 0.42 \text{ cm (estimated from Figure 4.2)}$$
$$R = 0.05 \text{ cm}$$
$$A = \pi (0.05 \text{ cm})^2$$

Substituting in these values, we find that $\overline{T} = 0.976 \ T_0$. But $\overline{T} = 66.4°C$ (from Table 4.1, measured 5 ms case). Therefore $T_0 = 68.03°C$. This is only a 2.4% change. From Figure 4.2, we see that we do not have a perfect gaussian. There is an approximately 6% power (hence temperature) variation across the 1-mm sampling aperture. For our estimate, we will pick something in between, say 4%. We will

therefore increase the temperature values in Table 4.1 by this amount. Correction for the sampling aperture of the radiometer is less than 1%. This is not considered significant enough to warrant changes in energy values listed in the table.

As already noted, the emissivity of the central target is changed, particularly at the higher IR exposure levels. This is not true of the side targets subject to bulk heating. Consequently, we must realign the relative room temperature level between the central and side targets by considering the post-exposure room temperature level of the central target, which sits below the pre-exposure level. Before making this particular adjustment, however, we must first perform another. In Figure 4.9a (taken from Figure 4.5), we note that the "room temperature" levels of both the central and side targets are set at the same place. This is misleading. The room temperature level of the side targets is set not by the film samples but by the chopper, which has a different emissivity. Using linear scaling on Figure 4.9a, we find that "room temperature" for the side targets is well below "room temperature" for the central target (cf Figure 4.9b). Consequently, we must put them on the same footing. This is shown in Figure 4.9c. With this adjustment complete, we can work on the film emissivity change. In Figure 4.9c, this amounts to $\Delta T = 20.1°C$. The immediate post-exposure film temperature is 133°C. To this we must add the aforementioned ΔT, which gives us a film temperature of 153°C. Finally we add on the 4% hike due to the sampling aperture effect to reach the actual film temperature, 159°C.
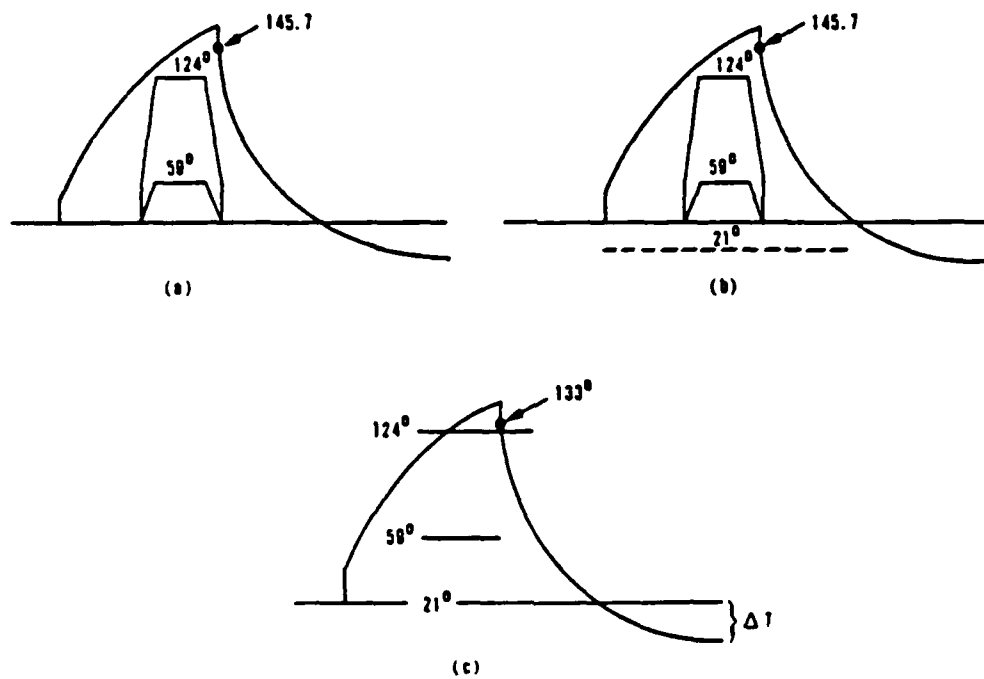
Figure 4.9. Adjustment for post-IR exposure emissivity change.

CHAPTER 5

SHAW MODEL

Introduction

In Chapter 2, we found a way to explain the DIRE curve in terms of a temperature-dependent characteristic curve. We learned empirically that the characteristic curve shifted laterally (relative to the exposure axis) toward increased sensitivity as more IR energy was deposited. However, knowing that a certain thing happens is not equivalent to understanding why it happens. In this chapter, we probe more deeply into the whys and wherefores of the IRPP phenomenon. We use, in a rather unconventional way, a model of the photographic process developed by Dr. Rodney Shaw.[9] In the next few pages, we provide some background needed to understand Dr. Shaw's model.

Shaw Model Development

Suppose we have a large array of detectors, closely packed and all the same unit area size and shape. Suppose, also, that this array is subject to uniform irradiance over some unit time period. Figure 5.1 illustrates a typical case (the black dots represent incident and absorbed photons). If we plot the fraction of detectors
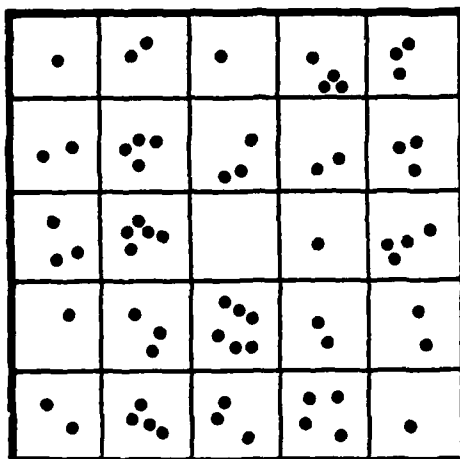
Figure 5.1. Close-packed detector
array subjected to a
Poisson photon rain.

receiving r photons, we find that the resulting graph is best fitted with a discrete probability density function known as the Poisson distribution:

$$P(r) = \frac{q^r}{r!} e^{-q} \tag{1}$$

where

$$\sum_1 P(r) = 1 \tag{2}$$

$$\bar{r} = \sum_1 rP(r) = q \tag{3}$$

An ideal detector would provide a one-to-one relationship between incident photons and some measurable output response of the detector. For now, we assume that response will be a number counter. In other words, if a particular detector received r = 5 photons, then the output count would be m = 5. If the array in Figure 5.1 is made up of such ideal detectors, then its response will faithfully mimic the photon flux falling on it. If we plot the average count level, $\bar{m}$, over all detectors vs the average number of photons (over all detectors), we obtain the plot shown in Figure 5.2.

In the real world, there are no ideal detectors. Real detectors have limitations, such as a signal threshold level below which they will not respond to stimulus and a saturation level above which they have the same fixed response. Let us consider the latter situation. Suppose a detector can accurately count each photon up to R photons. At R photons, the count number is M (Note: M = R). At R + n photons, the count number remains M. If we have an array of such imperfect detectors the average count $\bar{m}$ over all detectors for a Poisson photon rain, r = q, is
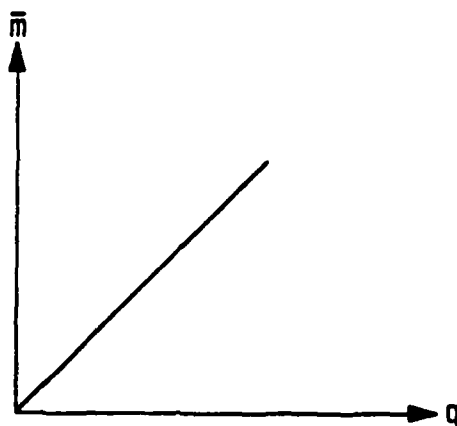
Figure 5.2. Average count response of
perfect detector array.
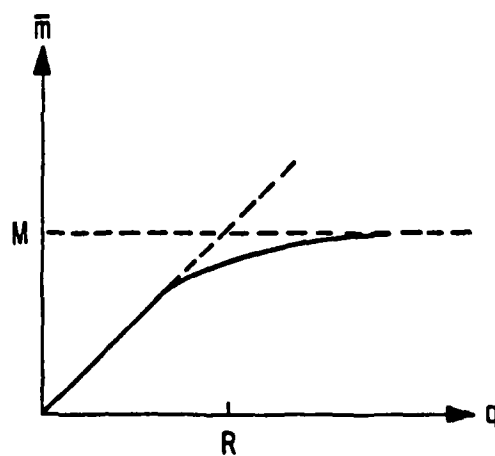
Figure 5.3. Average count response of
saturation limited detector
array.

$$\bar{m} = \sum_{r=1}^{r-1} r \frac{q^r}{r!} e^{-q} + \sum_{r=R} R \frac{q^r}{r!} e^{-q} \qquad (4)$$

Equation (4) can be considerably simplified, but the details are quite laborious. The reader is referred to reference 9. We obtain

$$\bar{m} = M(1 - f_1 e^{-q}) \qquad (5)$$

where

$$f_1 = \frac{1}{M} \left\{ 1 + \sum_0 \frac{q^r}{r!} + \sum_0 \frac{q^r}{r!} + \ldots + \sum_0^{n-1} \frac{q^r}{r!} \right\} \qquad (6)$$

A general plot of $\bar{m}$ is shown in Figure 5.3. As expected, the relationship is no longer linear . The average response rolls over and flattens out, never exceeding the average count level, $\bar{m} = M$.

The effect of both threshold and saturation levels is illustrated by Table 5.1. The detector count remains zero until the threshold is reached. It accumulates a count up to saturation. Beyond saturation, the count remains unchanged. The average count level, $\bar{m}$, in the presence of both threshold and saturation has the same form as Equation (5). However, f_1 now looks like

$$f_1 = \frac{1}{M} \left\{ \sum_0^{T-1} \frac{q^r}{r!} + \sum_0^T \frac{q^r}{r!} + \sum_0^{T+1} \frac{q^r}{r!} + \ldots + \sum_0^{S-1} \frac{q^r}{r!} \right\} \qquad (7)$$

where

$$M = S - T + 1 \qquad (8)$$

In a photographic film, the individual detector is a silver halide grain. It must receive Q photons to become developable. The site of the grain is therefore either clear or opaque after development. In other words, there is only a single recording level, $M = 1$. For single level recorders (SLRs), Equation (5) is still

90

Table 5.1.   Illustration of threshold and saturation effects on
detector photon counting.

					T						S		
r	1	2	3	4	5	6	7	8	9	10	11	12	13
m	0	0	0	0	1	2	3	4	5	6	6	6	6

valid, with f_1 having the form

$$f_1 = \sum_{o}^{Q-1} \frac{q^r}{r!} \tag{9}$$

Substituting Equation (9) into Equation (5), we obtain

$$\bar{m} = 1 - \sum_{o}^{Q-1} \frac{q^r}{r!} e^{-q} \tag{10}$$

It is important to notice that $\bar{m}$ is a fraction, i.e.,

$$0 < \bar{m} < 1 \tag{11}$$

Note that the second term in Equation (10) is just a finite Poisson sum. The sum of an infinite number of such terms is given by Equation (2).

We now need to relate $\bar{m}$ to density. A shortcut will be taken by way of the Nutting model, which relates the density of developed film to its silver content over a finite sampling aperture. The Nutting model also takes into account the random distribution of grain detectors, as illustrated in Figure 5.4. The Nutting formula is given by

$$D = N \frac{\bar{a}}{A} \log e \tag{12}$$

where

N = number of silver grains within sampling aperture

A = area of sampling aperture

$\bar{a}$ = average grain size

The Shaw model can be thought of as a variation of the Nutting model. The modification occurs in the parameter N of Equation (12), which is replaced by $N_o \bar{m}$. The Shaw model is therefore given by

$$D = \left[N_o \frac{\bar{a}}{A} \log e \right] \bar{m} \tag{13}$$

SAMPLING APERTURE
AREA IS "A"
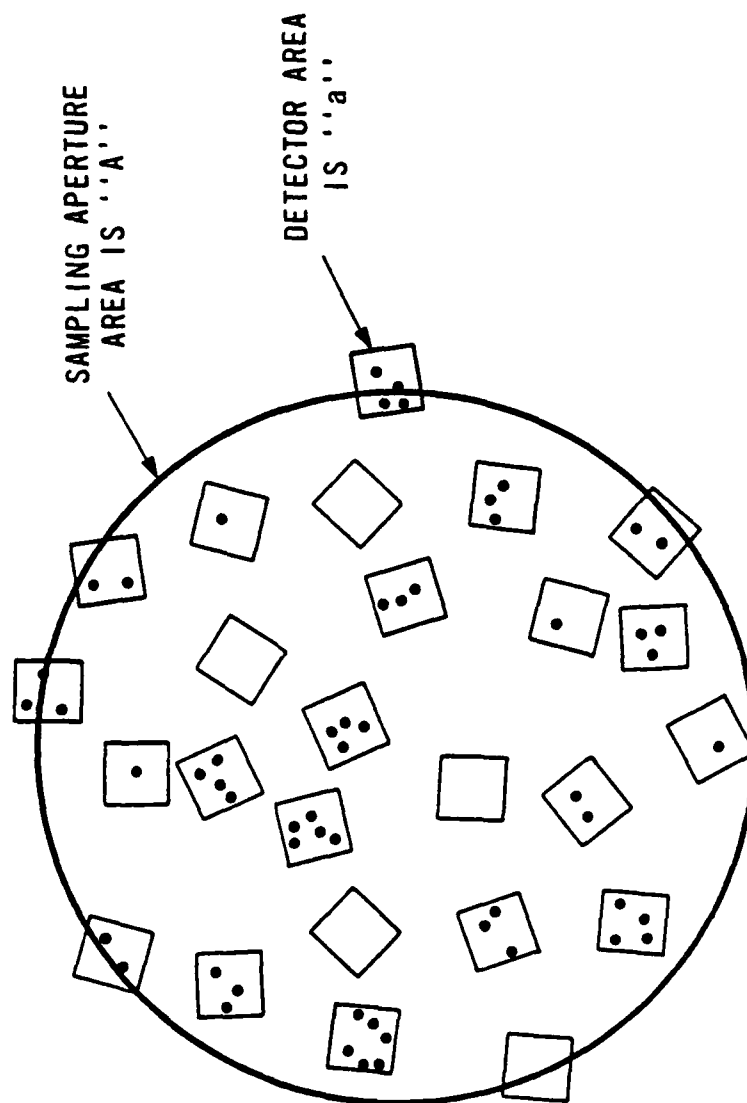
DETECTOR AREA
IS "a"

Figure 5.4. Random detector array subjected to sampling
aperture constraints.

The quantity N_0 is the total number of _silver halide_ grains present within the sampling aperture _before_ development. The entire quantity within the brackets yields the _saturation_ density of the film. The quantity $\bar{m}$ is given by Equation (10). This is a function of q, the average number of photons per _unit_ area grain. To account for changes in grain area, q in Equation (10) must be replaced by (aq). For example, if we double the size of a unit area grain (keeping the same irradiance), we obtain 2q photons/grain. Combining this modification with Equations (10) and (13), we obtain the simplest form of the Shaw model,

$$D = \left[N_0 \frac{\bar{a}}{A} \log e\right]\left(1 - e^{-aq} \sum_0^{Q-1} \frac{(aq)^r}{r!}\right) \qquad (14)$$

What we immediately notice about Equation (14), of pertinence to the IRPP phenomenon, are the parameters that are susceptible to the influence of temperature. If there is thermal expansion of the crystal, the quantity "a" will be affected. As "a" increases, so does the density. The other parameter of use to us is Q, the quantum sensitivity. This controls the number of terms in the summation. The fewer the terms, the higher will be the resulting density.

The final and most complex form of the Shaw model includes the effects of both grain size and quantum sensitivity distributions. Grains within a sampling aperture are not all the same size, nor will they all have the same quantum requirements. These influences are incorporated in Equation (15):

$$D = D_0 \left\{1 - \frac{1}{a} \sum_i \beta_i \left\{a_i e^{-a_i q} \sum_j \alpha_j \sum_0^{Q-1} \frac{(a_i q^r)}{r!}\right\}\right\} \qquad (15)$$

where

$$D_\bullet = N_\bullet \frac{\bar{a}}{A} \log e \qquad (16)$$

A simple example showing h w Equation (15) works is provided in Appendix 2. Because it is tedious to do such calculations by hand, Equation (15) (and variations) were programmed for use on a computer. These programs are contained in Appendix 3. Simple test cases were run, and were verified by hand calculation to make sure the programs were operating properly.

We now know enough about the Shaw model to use it. We want to simulate the experimental DIRE curve shown in Figure 5.5. The upper curve is specular density as seen by the PDS microdensitometer. This had to be corrected to diffuse density values (the kind of density the Shaw model uses). It is this lower curve we wish to fit by using the Shaw model.

Before proceeding to the discussion of thermal expansion, we must say a few words about grain size and quantum sensitivity distributions. It is beyond the scope of this work to determine actual distributions for Kodak 5369. Such measurements are extremely complex, difficult, and time consuming and would constitute major efforts in their own right. Our purpose in using the Shaw model is to basically define a viable approach for IRPP modeling investi- gations, and to explore the question of mechanism. We can satisfy these goals without resorting to specifics on distributions. However, the grai size and quantum sensitivity distributions we do use will have some basis in fact. In addition, the Shaw model does

EXPERIMENTAL DIRE CURVE
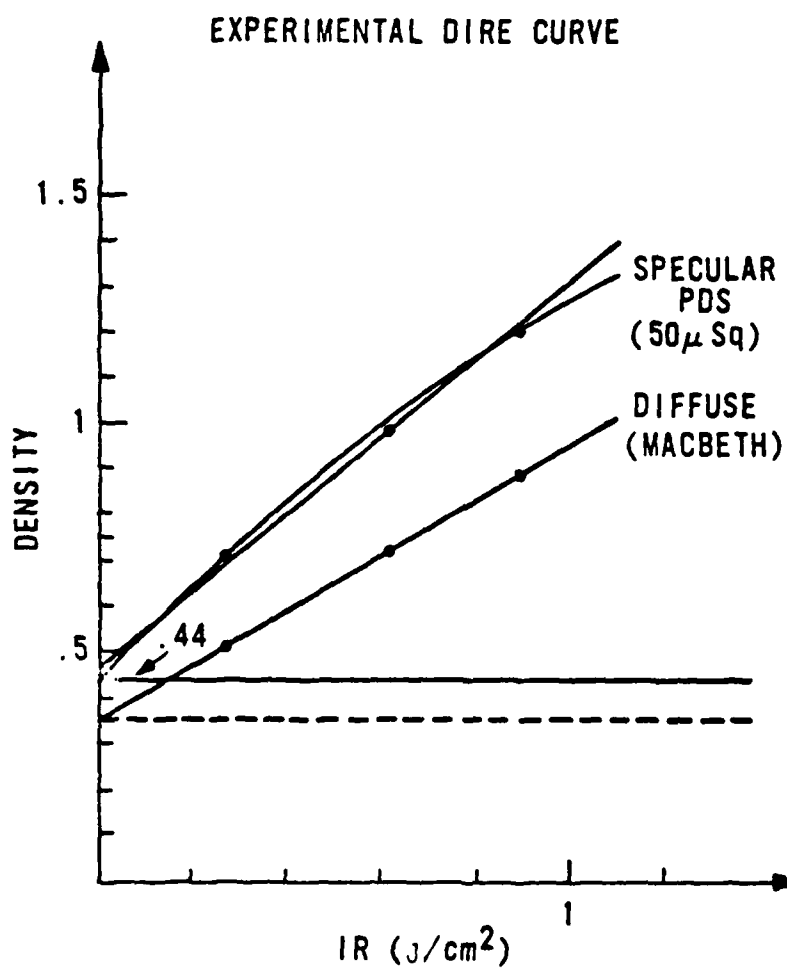
Figure 5.5. Linear fitted experimental DIRE
curve corrected for diffuse density.

not, as far as we know, take into account the effects of reciprocity failure. This will allow some uncertainty about the relationship between the actual measured background and the modeled background. The discrepancy will be in the number of photons needed for each.

Thermal Expansion

The silver halide contained in Kodak 5369 is silver bromide. The average linear grain size is ~0.25 μm. We know how hot the film gets in the IRPP process; consequently, we can calculate the change in grain area. If it is significant, the grains will present a larger cross-section for interaction with visible photons. The change in area is found from

$$\Delta A = 2 \, \gamma A \Delta T \qquad (17)$$

where

γ = coefficient of linear expansion = 3.37×10^{-5} $°C^{-1}$ for AgBr

A = room temperature grain area = 0.0625 μm^2

ΔT = change above room temperature

Using the maximum temperature found in our film heating experiments, we set $\Delta T = 140°C$. Substituting these values into Equation (17), we find $\Delta A = 0.0006$ μm^2. This represents less than a 1% change. We can use Equation (14) to see what this means in terms of a density change. However, we first need to pick values for D_o, q, and Q. Kodak 5369 saturates around a density of 3.3. Therefore, $D_o = 3.3$. We estimate that to obtain a background density between 0.4 and 0.5, the broadband visible energy being deposited is 1.66 X 10^{-9} J/cm^2. Assuming that $\bar{\lambda} = 0.5$ μm, its photon energy is

3.98×10^{-19} J (from $E = \frac{hc}{\lambda}$). Consequently, the number of photons per square centimeter is $\sim 4.17 \times 10^{9}$. Since q is defined for a square micrometers, we must divide that last number by the number of square microns in a square centimeter (10^{8}). This yields $q \simeq 42$ photons. Finally, we pick Q = 4 for the quantum sensitivity. Table 5.2 shows the results of this calculation.

We do see an increase in density, a change that would not be considered significant. One wonders, however, what would happen if grains were generally bigger, and followed a distribution. Then Equation (15) would have to be employed. The model we use for quantum sensitivity is shown in Figure 5.6 and tabulated in Table 5.3. It bears some resemblance to those models actually measured by Marriage.[10] For a large grain size distribution, we use one of the models employed by Shaw. It is shown in Figure 5.7 and tabulated in Table 5.4. In the program (Appendix 3), Figure 5.6 was fitted with a gaussian:

$$\text{Gauss}(a) = v_1 \, e^{-\left(\frac{a-v_2}{v_3}\right)^2} \qquad (18)$$

where

$$v_1 = .18766649$$

$$v_2 = 1.3163763 = \bar{a}$$

$$v_3 = .60334105$$

where

$$a = N(.2); \quad 1 \leq N \leq 14$$

$$N = \text{integer}$$

This was the room temperature curve. The temperature—

Table 5.2.   Thermal expansion calculations using simple form of Shaw model.

T(°C)	a	D	ΔD
21	.0625	.8905	
			.018
160	.0631	.9087	
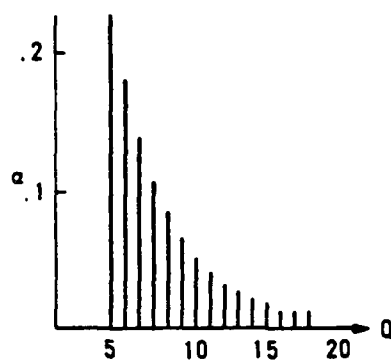
Figure 5.6. Exponential quantum
sensitivity distribution.
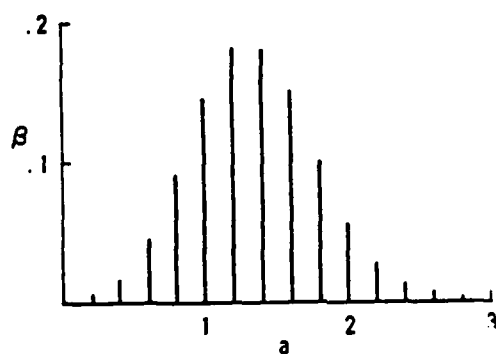
Figure 5.7. Gaussian (large)
grain size
distribution.

Table 5.3. Exponential quantum sensitivity distribution values.

Q	α	$\Sigma\alpha$
4	.225	.225
5	.180	.405
6	.136	.541
7	.106	.647
8	.083	.730
9	.064	.794
10	.050	.844
11	.039	.883
12	.030	.913
13	.024	.937
14	.018	.955
15	.014	.969
16	.011	.980
17	.009	.989
18	.007	.996

Table 5.4. Gaussian (large) grain size distribution values.

Grain Size	Fraction
a	β
0.2000000	0.0030000
0.4000000	0.0140000
0.6000000	0.0430000
0.8000000	0.0910000
1.0000000	0.1460000
1.2000000	0.1820000
1.4000000	0.1820000
1.6000000	0.1480000
1.8000000	0.0990000
2.0000000	0.0540000
2.2000000	0.0250000
2.4000000	0.0090000
2.6000000	0.0030000
2.8000000	0.0010000

shifted gaussian (for $\Delta T = 140°C$) had the following values:

$$v_2 = 1.328750237 = \bar{a}$$

where

$$a = N(.2) \times (1.0094); \quad 1 \leq N \leq 14$$

The values of v_1 and v_3 remained the same. In this test, the value of q was also varied. The results are shown in Table 5.5. Once again we see that thermal expansion plays an insignificant role in the IRPP process. This line of inquiry need no longer be pursued. The Shaw model has proved useful in that it has adequately eliminated a contender for the IRPP mechanism title.

Quantum Sensitivity Effects

With thermal expansion shown not to be the key of interest, quantum sensitivity (QS) is left as our only alternative. It seems reasonable to presume that the quantum requirements of the film are being reduced by the IRPP process. One way of looking at this is that a certain increasing percentage of the QS population relocates to lower values as the film temperature, induced by IR energy deposition, is raised. The situation is illustrated in Figure 5.8. Figure 5.8 (T=0) represents a portion of the room temperature QS distribution. After IR irradiation, (cf Figure 5.8b), a fraction of the population in Q_i has shifted into Q_{i-1}. At the same time, Q_i receives additional members from Q_{i+1}. An initial model will assume that the fraction, f, of a population which moves is the same for all Q_i. The percentage population α_i is therefore temperature dependent. This is shown by Equation (19) (where T is the temperature rise above

Table 5.5. Thermal expansion calculations using complex form of Shaw model.

q	UNSHIF	SHIF	ΔD
2	0.4458	0.4547	.0089
3	0.9632	0.9782	.0150
4	1.4709	1.4887	.0178
5	1.8993	1.9172	.0179
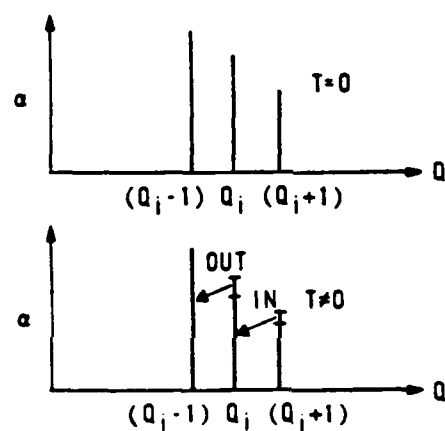
Figure 5.8. Simple model of quantum
sensitivity population
shift as a function of
temperature.

ambient):

$$\alpha_i(T) = \alpha_i(0) + f(T)\alpha_{i+1}(0) - f(T)\alpha_i(0) \qquad (19)$$

The next step is to employ Equations (19) and (15) with the QS distribution of Figure 5.6. (Note that $\alpha_{18}(T) = f\alpha_{18}(0)$, and $\alpha_3(T) = f\alpha_4(0)$.) A modified Shaw grain distribution, a narrow gaussian, defined by

$$\text{Gauss}(a) = .1877 \ e^{\left(\frac{a-25}{.09}\right)^2} \qquad (20)$$

is also used. Note that this is centered on $\bar{a} = 0.25$, which is closer to the sizes found in Kodak 5369. The values are tabulated in Table 5.6.

The results of this computer run are shown in Table 5.7 for two different q values. Note that lowering q not only reduces the background density but also increases the dynamic range. These results may be due to the larger spread in QS and grain size values. To test this, a single value for "a" was picked, i.e. a = 0.25 ($\beta = 1$), and was run for q = 42. The results, Table 5.8, turned out to be identical to those of the q = 42 case in Table 5.7. Evidently, the narrow gaussian used there is interchangeable with its average value. This encouraged us to try the Kodak 5369 average grain size, i.e. $a = 0.0625 \ \mu^2$, the results of which are also shown in Table 5.8. The background density decreases as expected. Note also that the density changes are on the order of those found for the q = 21 case in Table 5.7. This is probably because the product (aq) is approximately the same order of magnitude for both.

Table 5.6. Narrow gaussian grain size distribution values.

a	β
.235	.183
.205	.146
.175	.094
.145	.048
.115	.020
.085	.006

Table 5.7. Density values computed from linear population shift model (Q=3) using narrow gaussian grain distribution.

	DENSITY	
f	q=42	q=21
0	2.68	1.41
.5	2.76	1.58
1	2.83	1.76

Table 5.8. Density values computed from linear population shift model (Q=3) using single grain sizes.

	DENSITY	
f	a=.25	a=.0625
0	2.68	.326
.5	2.76	.474
1	2.83	.621

If we look at the diffuse DIRE curve in Figure 5.5, we note that a density range between ~0.36 and 1.0 must be bridged. In Table 5.8, the density ranges between 0.326 and 0.621. The quantity q could be increased slightly to raise the background density into the 0.36 neighborhood. The $f = 1$ end would see a ΔD increase of roughly the same amount. That still leaves a 0.34 shortfall in density. The only thing left to try is a modification in the QS temperature model. This will not, however, involve a change in Equation (19). Recall that some population was allowed to accumulate in $Q = 3$ for the $T = 0$ case. This is illustrated in Figure 5.9. The new modification will allow some population to spill over into $Q = 2$, as illustrated in Figure 5.10. Table 5.9 indicates what the *fractional population* will be for $Q = 2$ and $Q = 3$.

This model was run for $a = 0.0625$ and $q = 44$. The results are tabulated Table 5.10 and plotted against the DIRE curve in Figure 5.11. There are several things to note. First, the dynamic range has been increased by about 65%. Second, the $D(f)$ curve is not linear but has a noticeable bow. Third, the full range of the $D(f)$ curve still falls significantly short of the maximum density reached by the linear DIRE curve. Finally, for $f = 1$, the population in $\alpha_3(T)$ is zero, while population exists in $\alpha_2(T)$, and all $\alpha_i(T)$ for $i > 3$. Nonetheless, the data presented in Figure 5.11 are encouraging.

At this point, we decided to activate $Q = 1$, i.e., allow some population to accumulate here as well. The temperature model
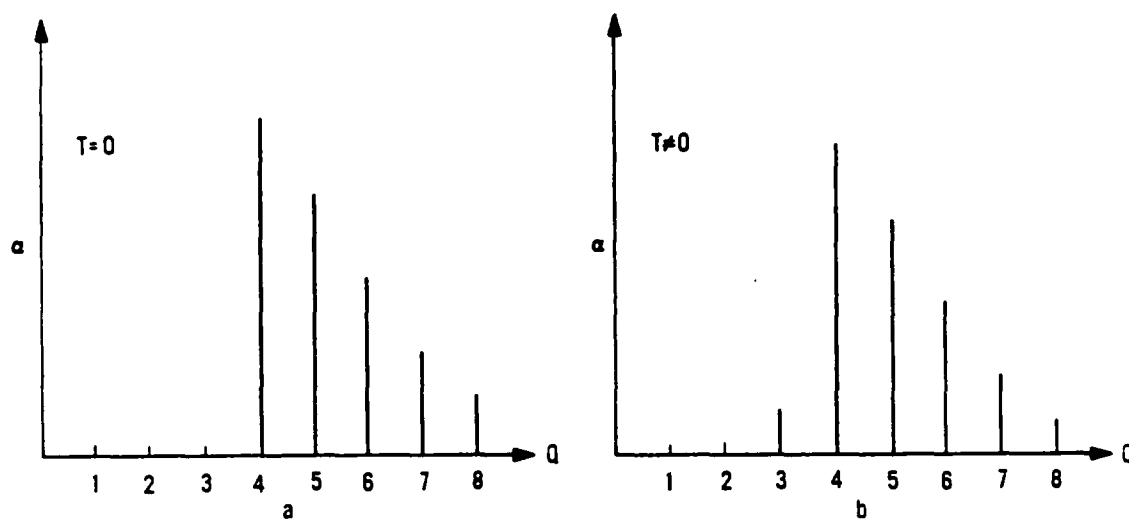
Figure 5.9. Illustration of population growth at
low quantum sensitivity numbers for $T \neq 0$.
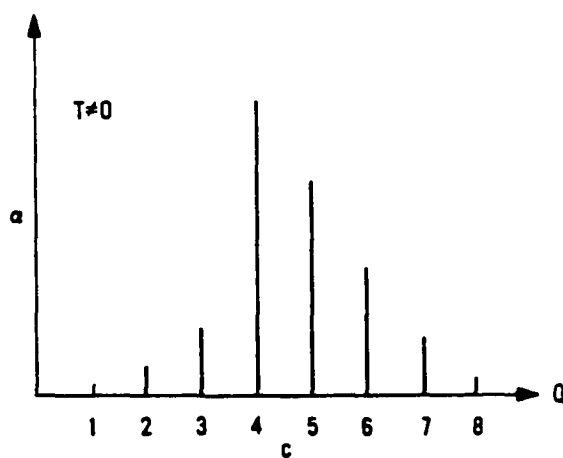
Figure 5.10. Population increase in $Q = 2$ for $T \neq 0$.

Table 5.9. Fractional population accumulation in Q=2 and 3.

Q_i	$\alpha_i(T)$
2	$f^2 \alpha_4(0)$
3	$f\alpha_4(0) - \alpha_2(T)$

Table 5.10. Density values computed from linear population shift model (Q=2) using single grain size.

f	D	$\Sigma\alpha_i$
0	.364	.993
.1	.397	.993
.2	.433	.993
.3	.473	.993
.4	.517	.993
.5	.564	.993
.6	.614	.993
.7	.669	.993
.8	.727	.993
.9	.788	.993
1	.853	.993
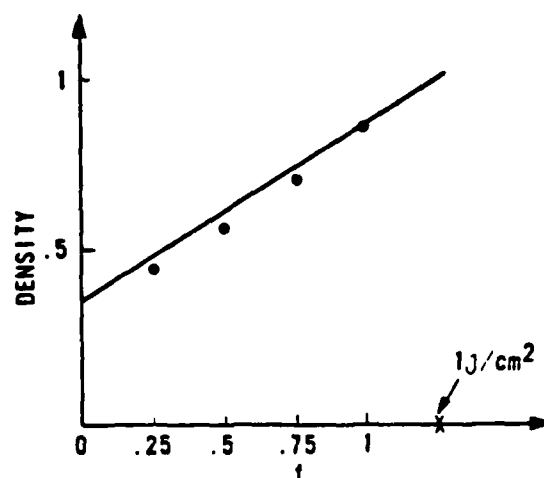
Figure 5.11. Comparison of linear population shift
model (Q = 2) with experimental DIRE
curve.
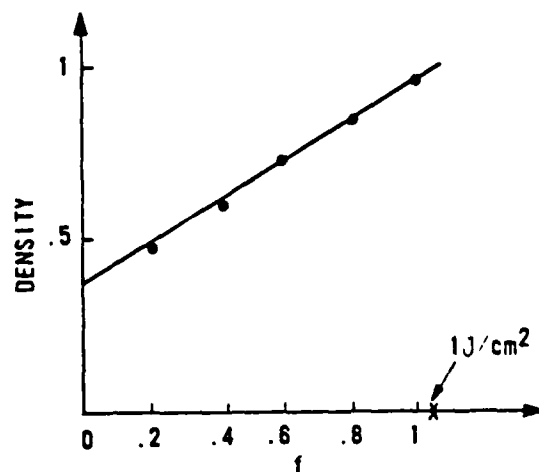
Figure 5.12. Comparison of modified linear population
shift model (Q = 1) with experimental
DIRE curve.

was also changed slightly to remove the zero population problem just mentioned. The modification would affect only the fractional population in Q = 1, 2, and 3 for T = 0. Table 5.11 shows the specific forms for $\alpha_i(T)$. Note that $0 \leq q \leq 1$ and $\sum_{i=1}^{3} \alpha_i(T) = f\alpha_4(0)$. A series of computer runs was made over the full range of f for various values of the parameter g. Results are presented in Table 5.12 and Figure 5.12 for the g = 0.95 case. The dynamic range has been increased another 22% over that in Figure 5.11. The data are much more linear. Only a modest bowing is evident. The maximum density of the D(f) curve is only 4% short of the full value we wanted to model. However, the population in Q_1 through Q_4 is lopsided, as can be seen from Table 5.12. Had we let g = 1, the population in Q_2 and Q_3 would have been zero for any value of f. Nonetheless, we have achieved remarkable agreement with the experimental data using this simple temperature model. In fact, it is possible to use the data in Figure 5.12 to relate f and IR energy via a simple linear model. At $f \approx 1$, the IR energy is 0.95 J/cm^2. Therefore, we can write

$$f = s \, E_{IR} \tag{21}$$

where $s = 1.05 \ (J/cm^2)^{-1}$. We could also find f(T) by making use of the data in Table 4.1 of Chapter 4.

Obviously, the thermal model we have employed is not unique. Other models might be employed, some of which could match up with the experimental data equally well. As a case in point a model based on the negative binomial distribution (NBD) was tried. (The latter was

Table 5.11. Fractional population accumulation in Q=1, 2, and 3.

Q_i	$\alpha_i(T)$
3	$f\alpha_4(0)-gf\alpha_4(0)$
2	$gf\alpha_4(0)-g^2f\alpha_4(0)$
1	$g^2f\alpha_4(0)$

Table 5.12. Density values computed from modified linear population shift model (Q=1) using single grain size.

f	D	$\Sigma\alpha_i$
0	.364	.993
.2	.484	.993
.4	.603	.993
.6	.723	.993
.8	.842	.993
1	.962	.993

suggested as a possibility by Dr. Shaw.) The NBD is shown in Equation (22):

$$\alpha_Q = \frac{(Q-1)!}{(Q-\tau)!(\tau-1)!}\left(\frac{1}{m}\right)^{\tau}\left(1-\frac{1}{m}\right)^{Q-\tau} \qquad (22)$$

The quantity τ is the required number of quanta (or photons) needed for latent image formation. It is the same for all grains. Q quanta are needed overall to achieve τ successes. Only one quantum in m contributes to the formation of a latent image center. For IRPP, we can suppose that either τ or m (or both) is temperature dependent. Figure 5.13 illustrates how the α_Q population shifts depending on whether τ or m is held fixed. Note that changing m has a bigger impact than changing τ. We therefore concentrate on m.

The computer program was modified to calculate the α_Q's from the negative binomial (with the check that $\Sigma\alpha_Q = 1$). The best match with the DIRE was obtained for $T = 2$ (q = 45). The results are tabulated in Table 5.13 and presented in Figure 5.14. The fit is not quite as good as that of Figure 5.12, but it is remarkable how such a totally different model can be used to approximate the DIRE curve.

Until now we have been content to use a uniform grain size (a = 0.0625). This is a bit unrealistic, though we did find that a narrow gaussian symmetric about this value gave essentially the same results. To remedy this situation, we developed the alternate distribution tabulated in Table 5.14 and shown in Figure 5.15. It is similar to one utilized by Shaw, but shifted and contracted. This was incorporated into the program and run as a function of m for $T = 2$ and q = 42. The results are shown in Table 5.15 and Figure
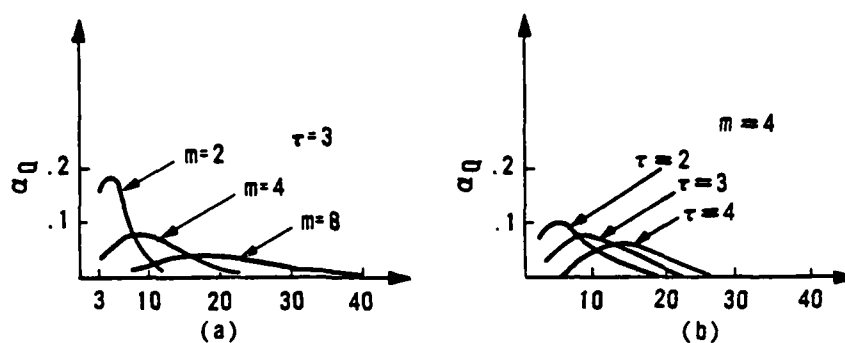
Figure 5.13. Population shift illustration when negative
binomial distribution (NBD) is used as a model.
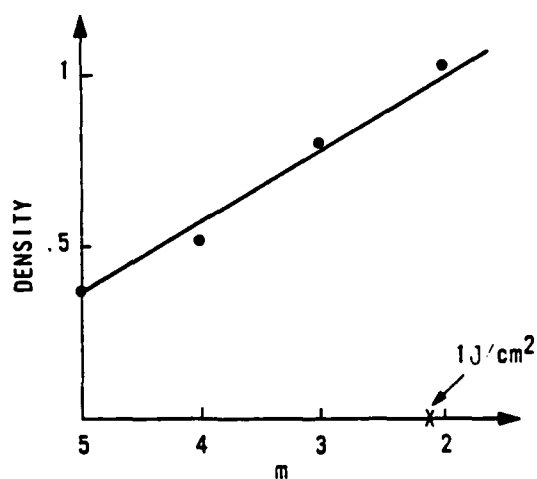
Figure 5.14. Comparison of NBD model with experimental
DIRE curve.

Table 5.13.   Density values computed from negative binomial
population shift using single grain size.

m	D	$\Sigma\alpha_i$
2	1.350	1
3	.796	1
4	.518	1
5	.366	.999
6	.284	.995

Table 5.14.   Alternate grain size distribution values.

a	β
.01750	.010
.02875	.055
.04000	.110
.05125	.150
.06250	.165
.07375	.140
.08500	.120
.09625	.085
.10750	.060
.11875	.035
.13000	.020
.14125	.015
.15250	.010
.16375	.005
	$\Sigma = .98$

Table 5.15. Density values computed from negative binomial population shift using alternate grain size distribution.

m	D	$\Sigma\alpha_i$
7	.359	.986
6	.416	.995
5	.531	.999
4	.727	1
3	1.06	1
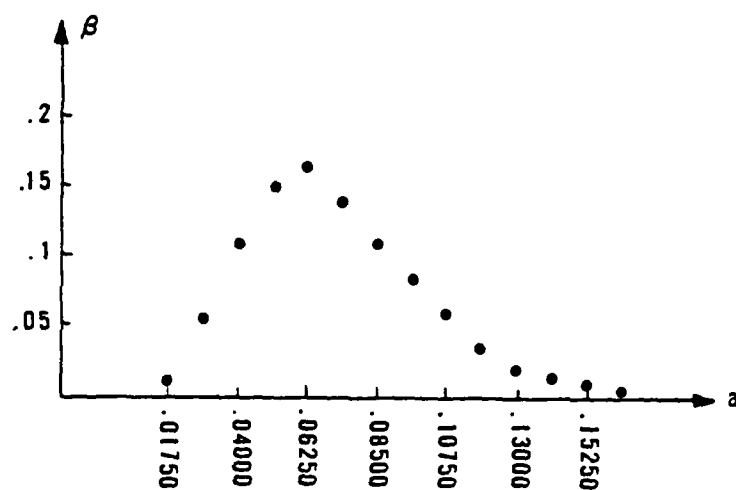
Figure 5.15. Alternate grain size distribution.
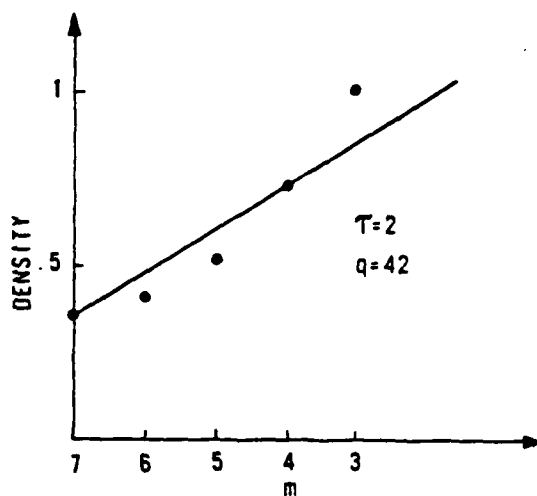
Figure 5.16. Comparison of NBD (alternate grain size) with experimental DIRE curve.

5.16. Note a more severe bowing in the data, but in both Figure 5.14 and 5.16 a density greater than 1 is achieved.

This brings to a close our modeling efforts. More serious follow-on investigations would do well to tie down grain size and quantum sensitivity distributions of the particular film being studied. However, we believe we have successfully demonstrated that the Shaw model is a reasonable approach to studying the IRPP phenomenon.

CHAPTER 6

SENSITIZING DYE

Introduction

In the previous chapter, a key to understanding IRPP was
uncovered. It involved the reduction of the film's overall quantum
sensitivity requirements. However, all we have done by this is
identify the appropriate "black box." The physics inside have yet to
be understood. In this chapter, we begin rummaging through the
contents of that box.

Silver halides, by themselves, are fairly insensitive to the
latter half of the visible spectrum. In order for them to respond to
photons inhabiting this region, sensitizing dyes are employed which
have strong absorption properties in this part of the spectrum. The
dyes adhere to the surface of the silver halide grain, forming a thin
molecular layer. Two theories are in vogue concerning the manner in
which a dye functions. The predominant one stresses actual photo-
electron transfer from the dye to the crystal. The other favors an
energy transfer of some sort with no exchange of particles. The film
used through most of this study, Kodak 5369, uses a sensitizing dye
to extend the spectral response of its silver bromide crystal grains.
One cannot help wondering whether the dye is responsible for the IRPP

119

effect in this film. A possible way of finding out is to test two identical films, except one would have a dye and one would not. We needed to find a dyeless cousin of Kodak 5369. Kodak suggested 2462, a blue-sensitive silver bromide emulsion. Figure 6.1 compares the spectral sensitivities of these two films. Table 6.1 compares several other pertinent parameters.

The information provided thus far looks favorable. However, two more pieces of data must be examined. The characteristic curves are compared in Figure 6.2. The respective MTFs are given in Figure 6.3. Figure 6.2 shows that 5369 is more sensitive. This is as expected with the dye being present. However, 5369 also saturates at a significantly higher density level, indicating more grain material. On the other hand, 2462 has a much better MTF, suggesting a finer grain. This is also reflected in the granularity numbers. Both films are, at core, silver bromide (as confirmed by electron spectroscopy). The 5369 has the dye but is also of coarser grain. The emulsion thickness (confirmed by independent measurements) is, fortunately, the same.

Experimental Comparisons

In testing the IRPP response of these two films, we would like to make a comparison in which both films receive the same visible exposure, and also one in which the background densities are matched. The reason for this is that the quantity q (average number of photons per unit area grain) in Chapter 5 affected the dynamic range. However, test results in Figure 6.4 show that for a visible

TABLE 6.1. Comparison of salient film parameters between Kodak 2462 and 5369.

Film	Granularity	Average Grain Size, μm	Emulsion Thickness, μm
5369	6	~.25	3-4
2462	5	~.20	3-4

SPECTRAL SENSITIVITY

DENSITY OF 1 ABOVE BASE FOG
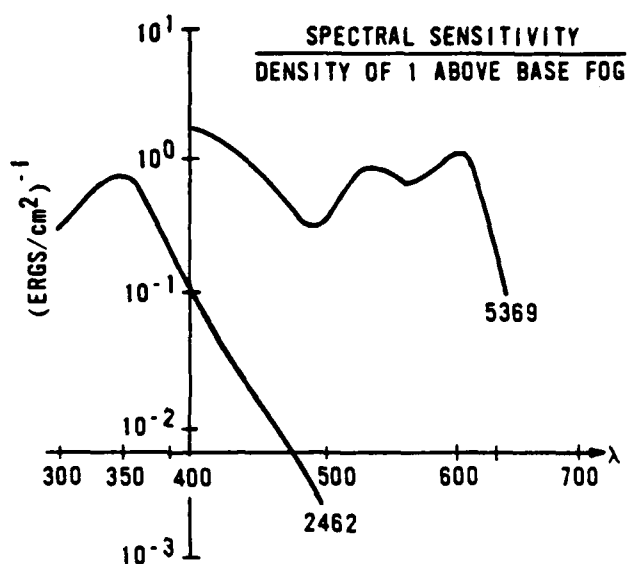
Figure 6.1. Spectral sensitivities of
Kodak 5369 and 2462.
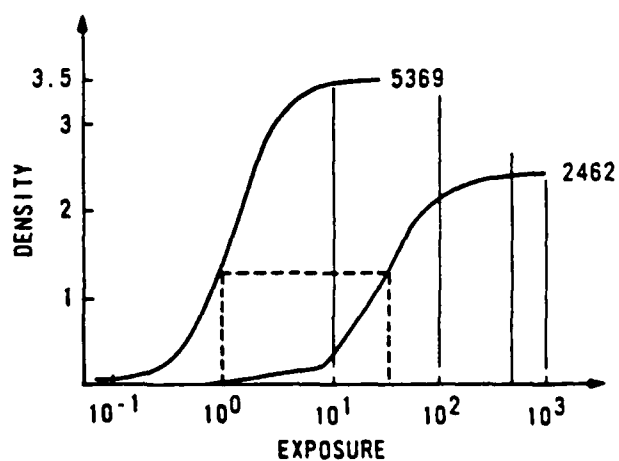
Figure 6.2. Characteristic curves of
Kodak 5369 and 2462.
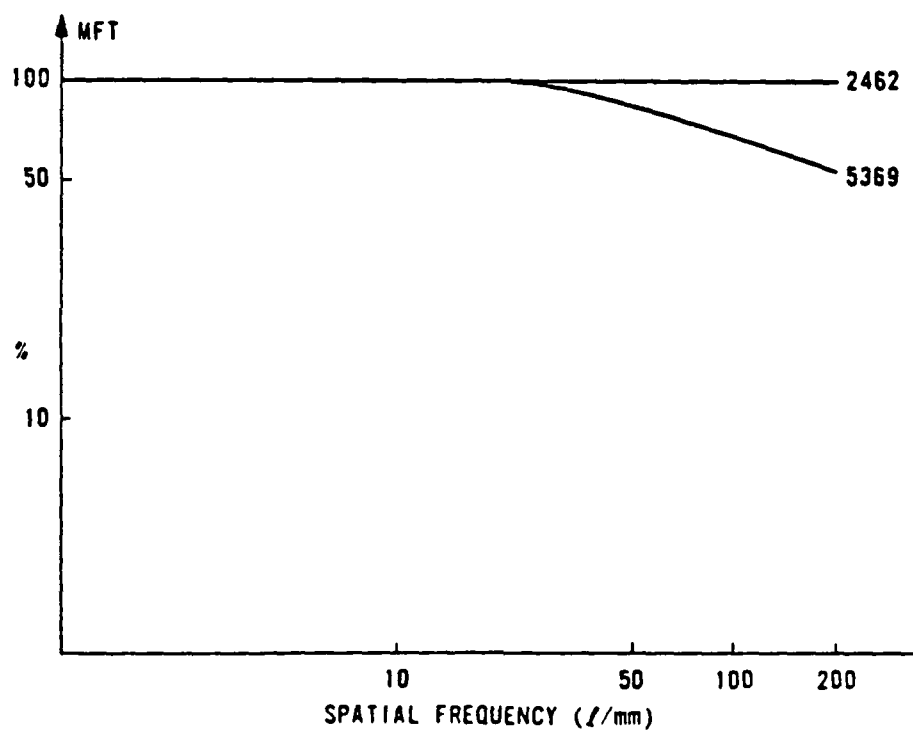
Figure 6.3. Modulation transfer function of
Kodak 5369 and 2462.
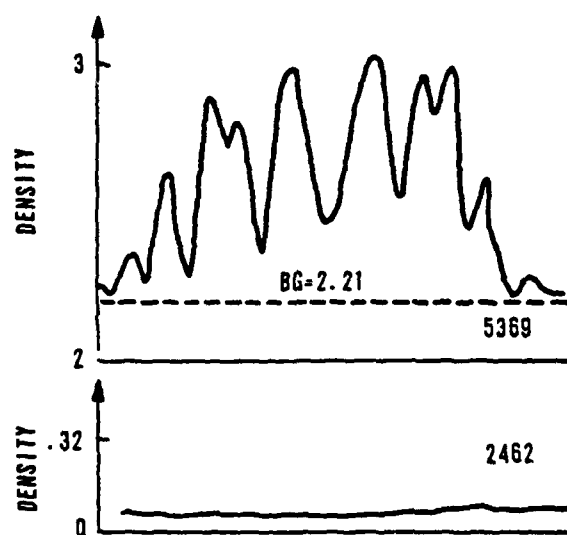
Figure 6.4. Film comparison: visible exposure
held constant.

exposure of 0.35 ergs/cm^2, 2462 is completely immersed in the nonlinear toe region of its characteristic curve, thereby washing out the IR information of interest. On the other hand, 5369 is making inroads into its own shoulder region, thus causing a nonlinear mapping of IR data. Consequently, a good comparison test between these films for the same visible exposure level is out of the question. We are left with matching background densities. Figures 6.5 and 6.6 show microdensitometer comparisons between the two films for two different background density levels. The first thing to note is that the IRPP effect still occurs even in the dyeless emulsion. This fact should simplify investigations into the basic IRPP phenomenon by removing from consideration the complex dye-silver halide interaction. On the other hand, 5369 shows a definite superiority in performance, due in all likelihood to the presence of the dye. A rough estimate of performance can be made by comparing the density difference between the central valley and adjacent peaks (as indicated in Figure 6.5) between Figure 6.5a and b and Figure 6.6a and b. Using this measure, Kodak 5369 is approximately 2.4 times better. (For these comparison tests, both films were processed together in the same can, at the same time, at D-72, 3 minutes, 69°F; agitation.)

If the dye's presence is the reason for the more efficient performance, it might be possible to negate its influence. This might be accomplished by operating in a spectral region where the dye's longer wavelength absorption properties are no longer utilized.
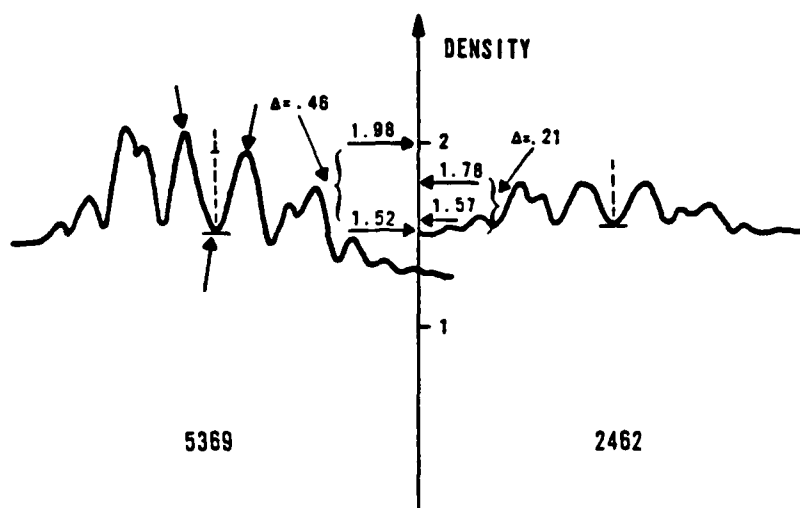
Figure 6.5. Film comparison: background density (HIGH) matched.
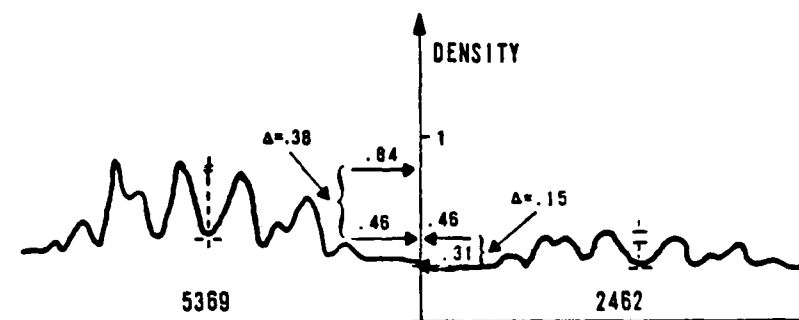
Figure 6.6. Film comparison: background density (LOW) matched.

An IRPP test was run using a narrowband interference filter centered on 410 nm. (See Figure 6.7.) The results are shown in the micro-densitometer traces of Figure 6.8. Once again 5369 is a better performer, this time by a factor of 2. Apparently, the dye's interaction with IR energy is still operative. It seems indifferent to the presence or absence of longer wavelength visible photons.

Comparison Using Shaw Model

The enhancing effect of the dye must be taken with a grain of salt at this point. We must ask ourselves how much of the modulation difference seen between 5369 and 2462 could be attributed to the difference in grain size and silver bromide content (the latter controlling the density saturation level). This question can be investigated by using the Shaw model. In Chapter 5, the linear part of the 5369 DIRE curve was successfully fitted. By altering the quantities "D_θ" and "a" in Equation (15), we should also be able to model Kodak 2462. We will use the QS temperature model given by Equation (19), and allow population to accumulate in $Q = 3$ and $Q = 2$. For Kodak 2462, the saturation density D_o will be set at 2.3, the grain area at 0.04 μm^2. The latter number is an estimate based on granularity and MTF data. Using the appropriate parameters for 5369 and 2462, the quantity q is adjusted in each case to achieve a background density equivalent to that shown by Figure 6.6. However, Figure 6.6 is rendered in specular density, and the Shaw model uses diffuse density. Consequently, the background density in Figure 6.6 must be corrected. Once the diffuse background density has been
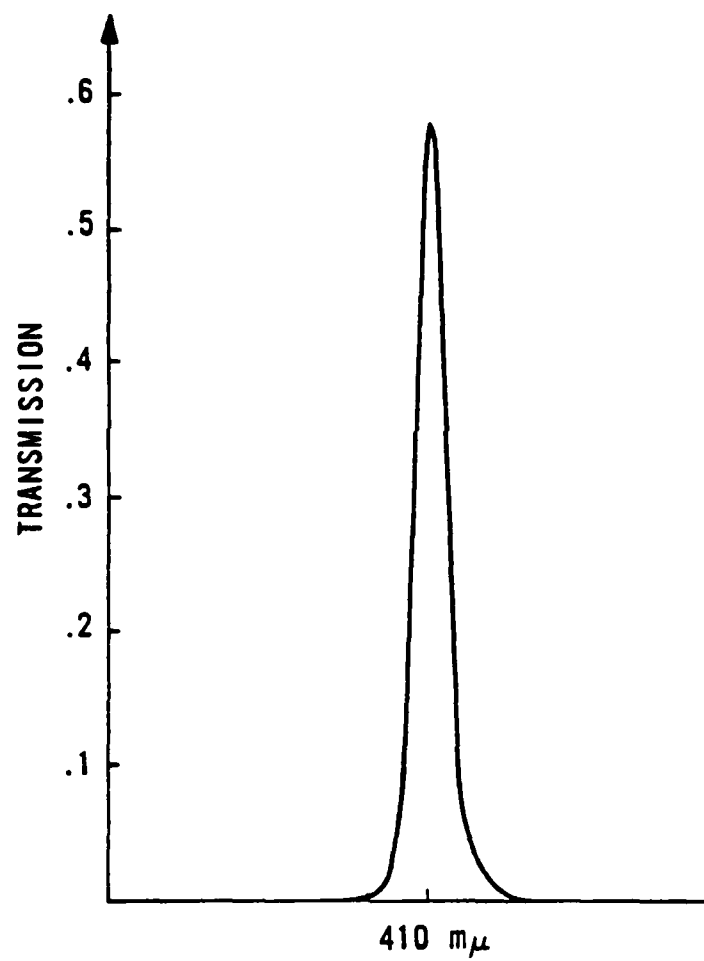
Figure 6.7. Spectral transmission of interference filter.
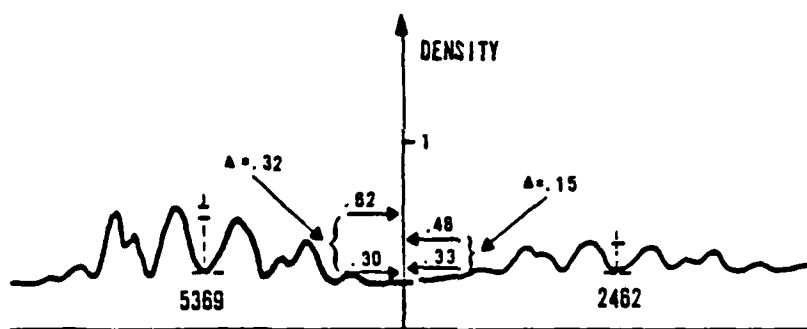
Figure 6.8. Film comparison in which red end of visible
strobe spectrum was not available to the dye.

approximately matched for both films, the quantity f is varied over its full range. The results of this are shown in Figure 6.9. Returning to Figure 6.6, the specular density values of the indicated valley and adjacent peaks for both 5369 and 2462 are also corrected to diffuse readings. The diffuse density differences are then calculated. These results are shown in Table 6.2. (Note that the ΔD for 5369 is now approximately 2.7X that for 2462.) We then take the peak and valley diffuse density readings of 5369 (determined from Figure 6.6) and locate these positions on the 5369 curve of Figure 6.9, and illustrated in Figure 6.10. These density positions correspond to certain f values. If it is now assumed that the only difference between 5369 and 2462 is in grain size and saturation level, we can use the same two f values (which locate the peak and valley densities for 5369) to determine the peak and valley densities for 2462, as indicated in Figure 6.11. These density values and differences are shown in Table 6.3. Note that the density difference for 5369 is approximately 1.3 times that of 2462, as predicted by the model. By using the Shaw-fitted 5369 experimental DIRE curve to extrapolate the 2462 DIRE curve, an implicit bias is built into the latter. This bias is that 2462 is modeled as if it had a dye attached. If this were so, the density differences seen between the two films is 1.3X. In actuality, it is 2.7X! The fact of the matter is that 2462 does not have a dye. Consequently, we can definitely say that the dye does make a substantial contribution in enhancing the IRPP effect.
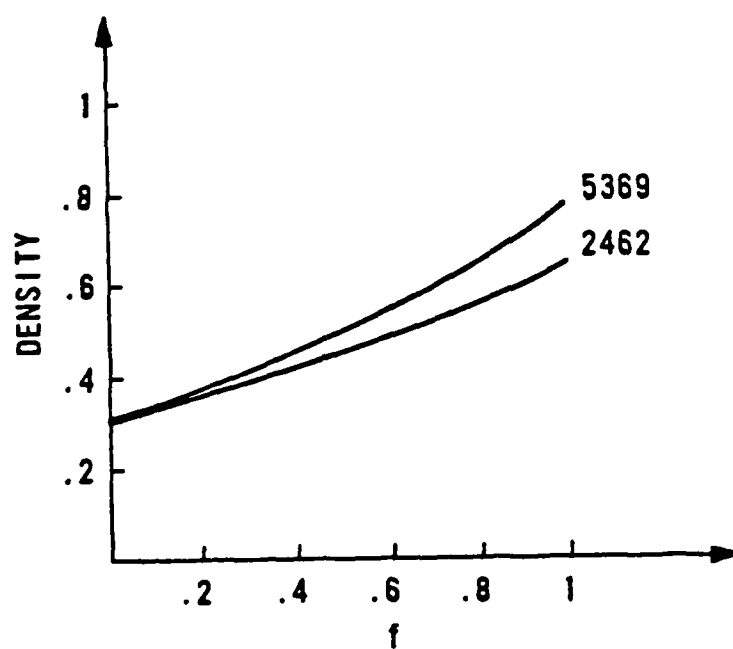
Figure 6.9. Simulation of 5369 & 2462 DIRE
curves via Shaw model.

TABLE 6.2. Specular and diffuse densities, and differences for Kodak 5369 and 2462.

	5369			2462		
	D_P	D_V	ΔD	D_P	D_V	ΔD
SPECULAR	.84	.46	.38	.46	.31	.15
DIFFUSE	.63	.33	.30	.33	.22	.11

TABLE 6.3. Diffuse densities, and differences for 5369 and 2462 via modeled DIRE curves.

	5369			2462		
	D_P	D_V	ΔD	D_P	D_V	ΔD
DIFFUSE	.63	.33	.30	.53	.30	.23
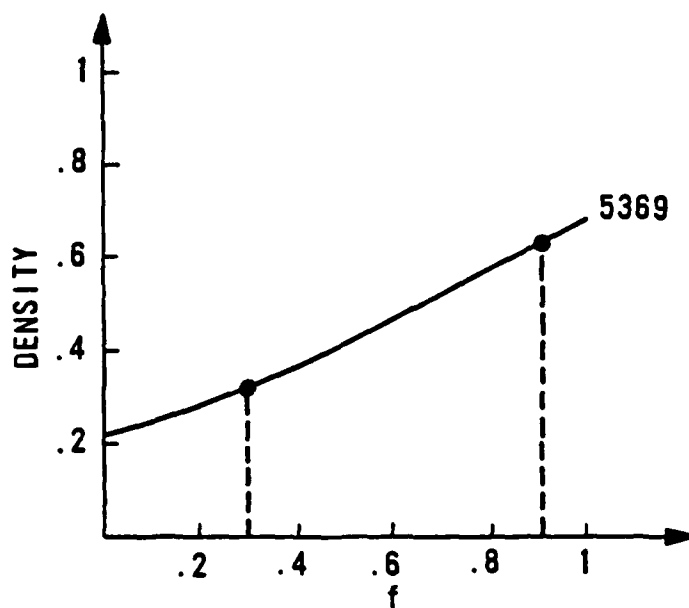
Figure 6.10. Peak & valley diffuse density
points located on 5369 curve.
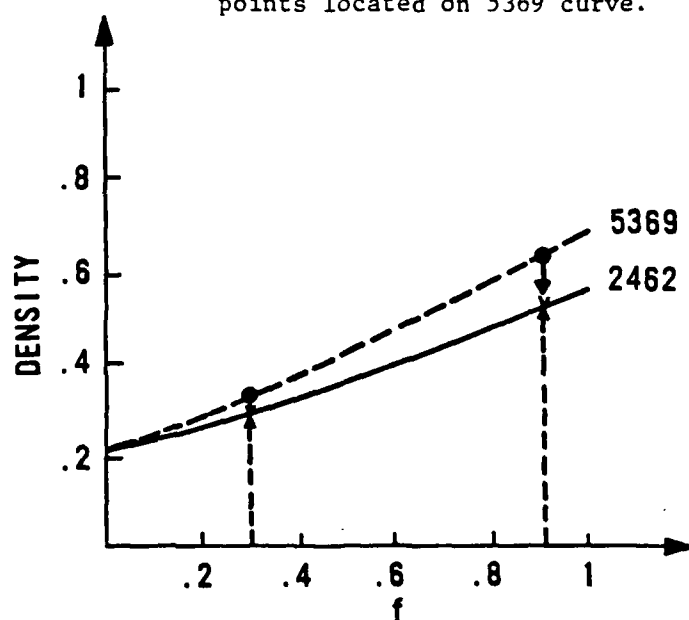
Figure 6.11. Peak & valley diffuse density
points located on the 2462 curve
from the 5369 curve.

CHAPTER 7

IONIC CONDUCTIVITY

Introduction

It is well known that bulk silver halide crystals demonstrate higher ionic conductivity with increases in temperature.[11] This can be due not only to increased mobility of the ions, but also to an increase in overall ionic population. It may be that silver halide grains in a film emulsion also experience increased ionic conductivity during the IRPP process. Suppose that IR irradiation causes a higher population of Ag^+. This would increase the probability of latent image centers being formed for a given visible exposure. In other words, the quantum requirements of the film would have been decreased. It would be interesting (and challenging) to measure such a population change in the context of the IRPP phenomenon, i.e., apply the IRPP technique to a piece of test film and look for transients in ionic population. The conceptual method of attack was to examine changes in an induced dipole moment by measuring transient capacitance. Consider a silver bromide crystal between the plates of a charged capacitor (Figure 7.1). The electric field due to the capacitor induces a net dipole moment in the crystal. Suppose now that the crystal is subjected to

134

a pulse of IR laser radiation. The crystal heats up. The ionic population increases, resulting in an increase in the net dipole moment. This in turn changes the system capacitance.

If we sandwich a piece of film between the plates of a charged capacitor, we have, instead of a single crystal, thousands of silver bromide grains, little conductive islands embedded in a thin insulating gelatin sea. Each grain is a tiny dipole. When the emulsion heats up, each dipole becomes a bit stronger. The contribution of any one grain will be minuscule. However, the combined influence of changes in hundreds of thousands of grain dipoles just might be measurable. Capacitance is defined as

$$c = \frac{q}{V} \tag{1}$$

where

$$q = \text{free charge}$$

$$V = \text{voltage}$$

For a parallel plate capacitor filled with dielectric,

$$C = \frac{\varepsilon A}{d} \tag{2}$$

where

$$A = \text{plate area}$$

$$d = \text{plate separation}$$

$$\varepsilon = \text{permittivity}$$

Now consider a parallel plate capacitor with some dielectric sheet in between as illustrated in Figure 7.2. The capacitance is

$$C = \frac{q}{V} = \frac{\varepsilon_o \varepsilon E A}{E_o(d-b) + Eb} \tag{3}$$

where
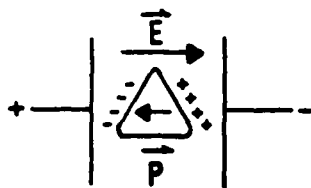
Figure 7.1. Thought experiment,AgBr
grain between charged
capacitor plates.
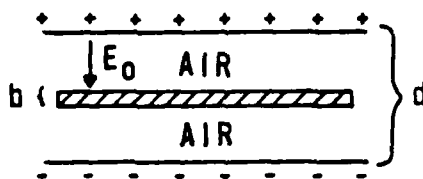
Figure 7.2. Simple model for a film
capacitor.

E = electric field inside the dielectric layer

κ = dielectric constant

If we divide the top and bottom of the right-hand side of Equation (3) by E, and recall that κ = E_o/E, we find that

$$C = \frac{\varepsilon_o \kappa A}{\kappa(d-b)+b} \qquad (4)$$

Equation (4) could be used to model a piece of film between the plates of a capacitor, provided "base material" replaced "air," i.e., ε_o in Equation (4) with ε_B, the permittivity of the base. The thin emulsion layer of the film would be represented by the thin dielectric sheet in Figure 7.2.

To obtain some idea of the size of the capacitance we would be dealing with, the value due to the base material (130 μm thick) can be calculated. Since the emulsion is only 4 to 5 μm thick, the base will dominate any measurement. Equation (2) can be used with

$A = 1$ cm^2

$d = 135$ μm

$\varepsilon = \kappa_B \varepsilon_o$

$\kappa_B = 3.5$ (acetate, based on in-house measurement)

inserting these values into Equation (2), we obtain C = 23 picofarads! However, we will be trying to observe even smaller capacitance changes induced in the film by the laser pulse. This could be on the order of a picofarad or less.

Experimental Setup

The capacitors were made by gold-coating (150 Å) both sides of a small film sample. This coating was originally made thick enough to allow good surface conductivity but thin enough to provide some transmission of the 10.6-μm radiation into the film. (As it later turned out, too little IR energy was transmitted into the film to cause any significant heating of the emulsion.) Wire leads were attached to the gold coating with a conductive epoxy. There remained, however, the poor coupling of IR into the emulsion. The basic requirement of the experiment was to heat up the emulsion. In the IRPP process, this is accomplished by absorption of IR photons in the emulsion and base material. For the capacitance measurements, there was no real need for IR photons and emulsion to interact directly, provided the emulsion could be heated on the time scale of the phenomenon. This was accomplished by coating the emulsion side of the capacitor with a thin layer of IR absorbing paint. The paint acted as the energy transducer: It absorbed photons and heated up. This heat was then immediately transferred through the thin gold layer and into the film. The emulsion got hot. Figure 7.3 illustrates the arrangement of this unusual capacitor.

The test configuration is illustrated in Figure 7.4. A closeup photograph of the circuit board is shown in Figure 7.5. This circuit had to be sufficiently sensitive to measure very small capacitance changes, and needed to do so on the time scale of the event, i.e. several milliseconds. Figure 7.6 is a simplified diagram
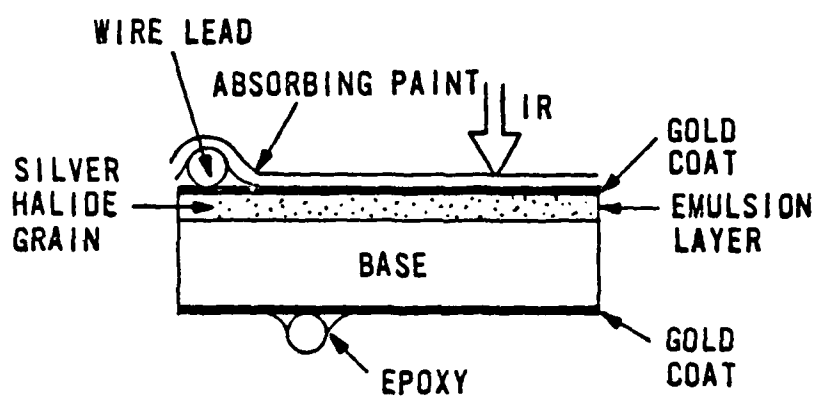
Figure 7.3. Illustration of fabricated film
capacitor used for tests.
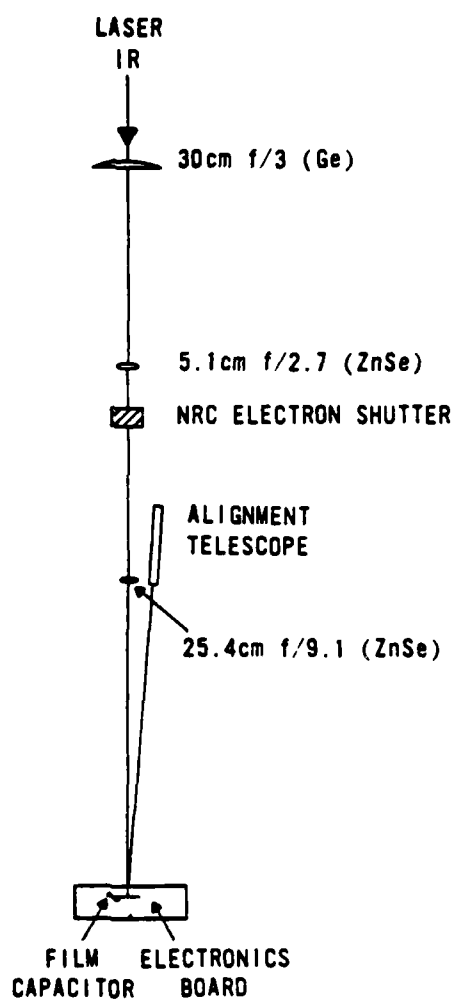
Figure 7.4. Experimental arrangement for
ionic conductivity tests.
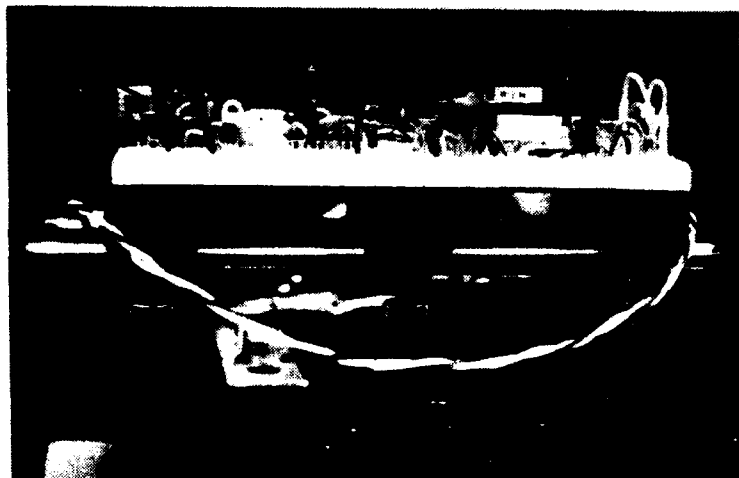
Figure 7.5. Photograph of circuit board with film
capacitor incorporated.

of the circuit (built by Mr. Dave Holmes). There was a constant bias voltage across the capacitor. The circuit measured the capacitance change indirectly by measuring the change in charge on the plates.

Test Procedure

A gaussian IR laser beam was centered on the test area of the target capacitor (with the aid of the alignment telescope and burn paper) as illustrated in Figure 7.7. Prior to IR energy deposition, the capacitor's leakage current was measured. This provided a reference. As a precaution, the actual test was conducted in the dark to eliminate possible photoelectron effects. Four IR exposure levels were used: 20, 30, 40, and 50 ms. Three to four runs were made at a given exposure and averaged. A rest period of 20 to 30 seconds preceded each additional run to allow the film capacitor to cool to room temperature. After the 50-ms runs, a test was again made at the 20-ms level to make sure nothing irreversible had occurred at the higher exposure levels. If this post-test compared well with the initial 20-ms data, it was assumed that the film had sustained no damage or permanent alteration.

It was not possible to separate out transient dipole changes in the silver halide grains from possible (and likely) transients in the gelatin-base material. Therefore, a control was needed. That control turned out to be a piece of film in which the silver halide grains had been removed from the emulsion (by hypo). A capacitor test sample was made from this film in a manner identical to that already described. This "clean" sample was put through the same
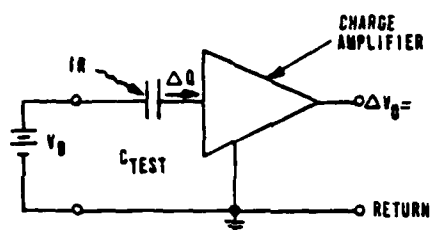
Figure 7.6. Diagram of charge-measuring
circuit.
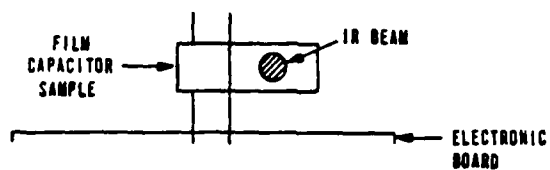
Figure 7.7. Illustration of beam location
on the film capacitor target.

barrage of IR tests as the "dirty" one. It would be the differences between these two cases that would be of interest.

Test Results

Results of these tests are shown in Figure 7.8. (Note: the vertical scale is in mv, where 20 mv = 0.17 picofarad). Each data frame is divided by a vertical time bar. To the right of this bar the laser is on; to the left, it is off. As the film heats up, the capacitance of both samples _decreases_! The decrease is almost linear with the amount of IR energy deposited. The decrease for the "clean" sample is about twice that of the "dirty" sample. In our simplistic model, we had expected an increase in capacitance. However, the "dirty" curve is actually _positive_ relative to the "clean" version, indicating a real increase in capacitance. This indicates that ionic conductivity had also increased. In the 100-ms observation window, the film capacitances do not return to coincidence with the reference after the IR exposure. The most we see is a paralleling of the reference. The full recovery period is probably several hundreds of milliseconds. Recall from Figure 1.16 in Chapter 1 that the density modulation of the fringes also showed a similar slow recovery trend.

It should be pointed out that the "dirty" sample, though undeveloped, was still an exposed piece of film. There was no convenient way of gold-coating in the dark. Even the coating process itself involves exposing the test film to a "glowing boat" in the vacuum chamber. However, attempts were made to minimize the overall exposure buildup. The "clear" sample had been soaked in hypo,
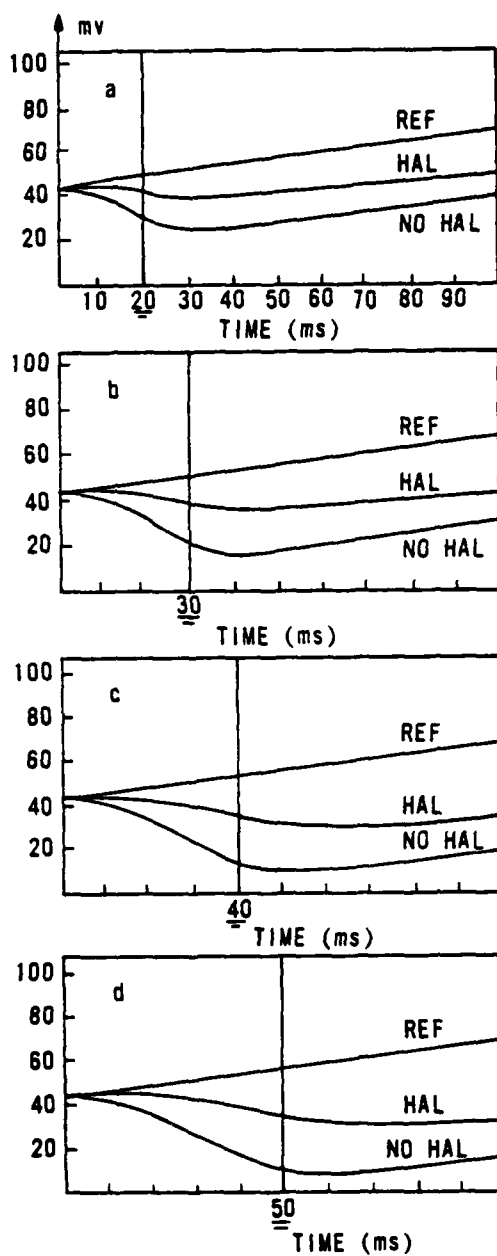
Figure 7.8. Test results for bias
voltage, V = 15 volts.
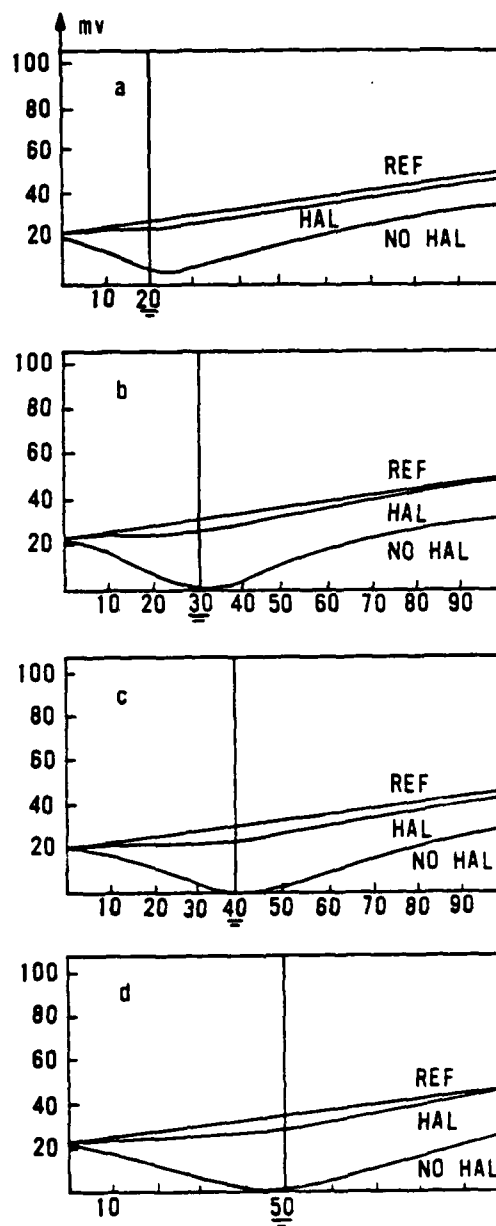
Figure 7.9. Test results for bias
voltage, V = 0.

washed, and dried. It was not known whether this left unwanted residues in the emulsion, or altered its basic composition other than to remove the silver halide.

The ionic conductivity experiment was repeated several times. On one of those occasions, the bias voltage on the film capacitor had been inadvertently disconnected. In that event, nothing should have happened. Unfortunately, this was not the case. Figure 7.9 presents the results of that test. A fair resemblance to the data in Figure 7.8 can be seen. Somehow, through some unknown mechanism, charge separation was being induced in the film in response to the transient thermal shock loading. This charge separation showed up in the measuring circuit. It seems that this effect would take place even in the presence of a bias voltage. Consequently, the result we are really looking for is the difference between the biased and unbiased tests. Figure 7.10 shows plots of the "dirty" and "clean" samples with and without the bias voltage. The next step is to subtract the $V = 0$ part of the curve from the $V \neq 0$ part for both "clean" and "dirty" samples for each exposure case, and then plot these difference curves relative to the reference level. Figure 7.11 shows the results of this process. This should represent the charge or capacitance change due to increased ionic activity. The first thing to notice is that during the heating period, the "clean" sample's capacitance is always higher than that of the "dirty" sample. The reverse had been expected. In fact, initially, the "clean" sample is even higher than the reference. The
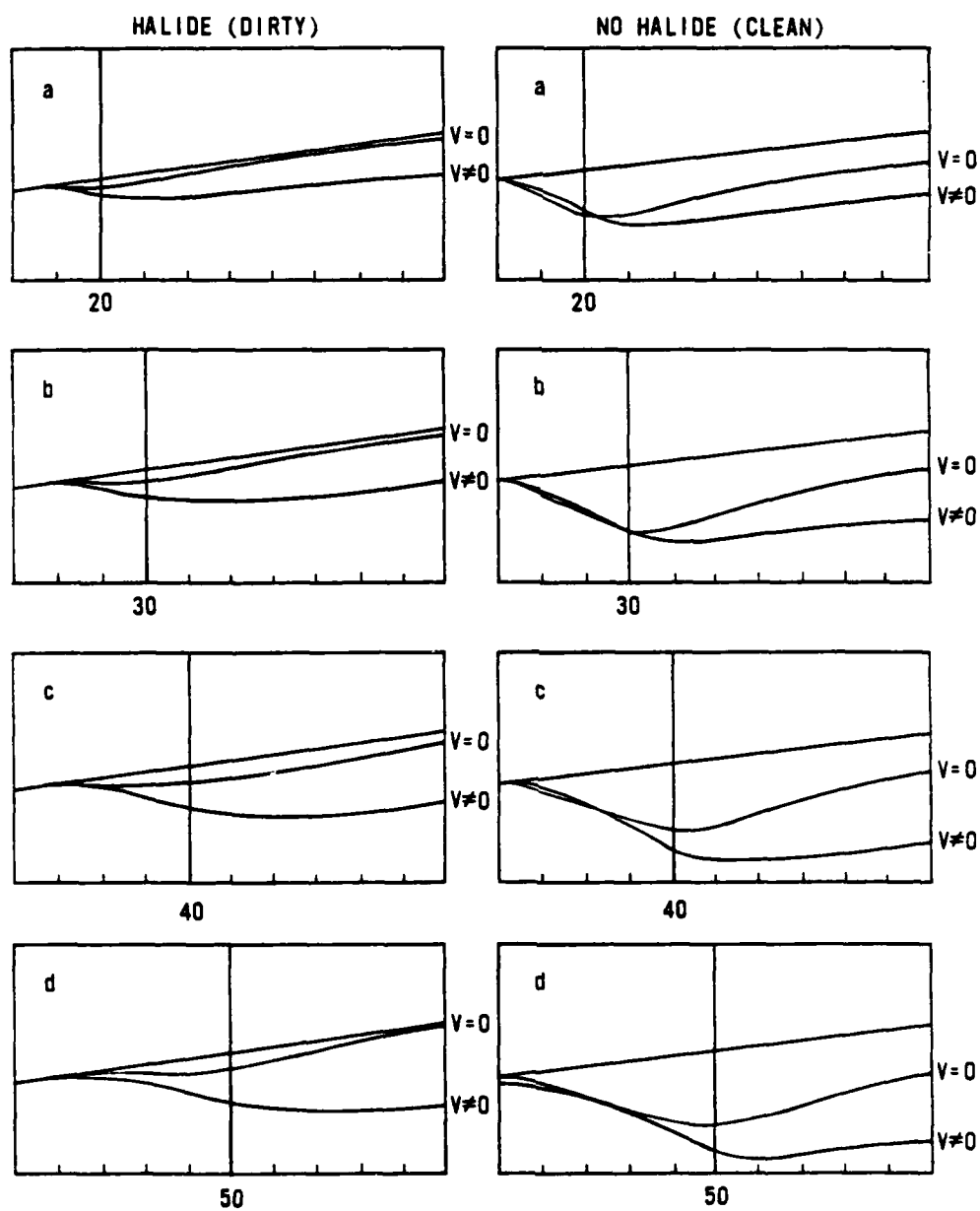
Figure 7.10. Comparison of "dirty" and "clean"
samples with and without bias
voltage.
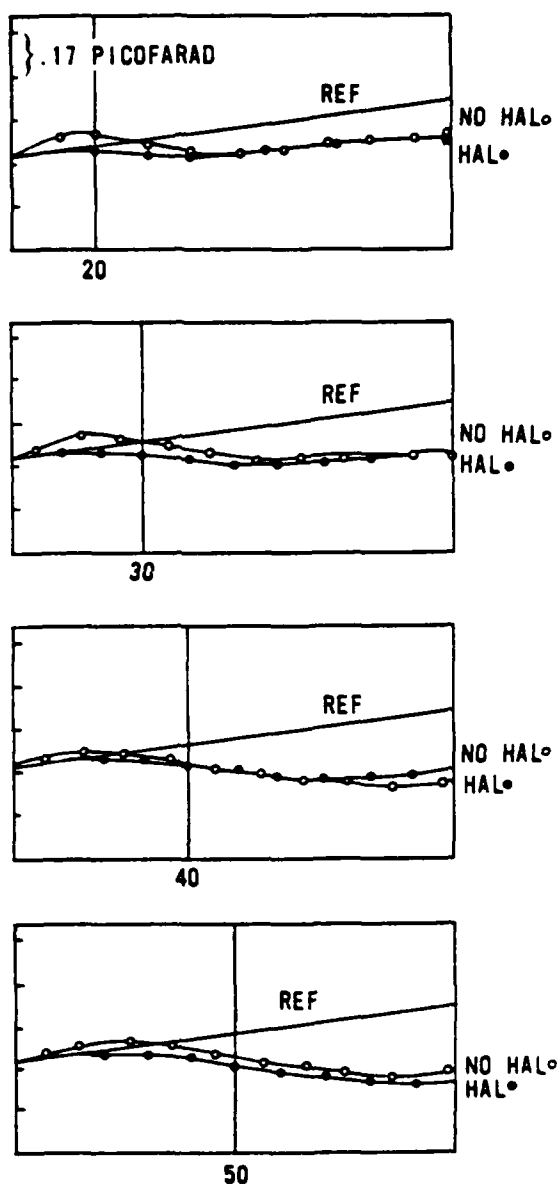
Figure 7.11. Difference curves for "clean"
and "dirty" sample.

"dirty" sample is always less than the reference. After the heating period, the two film curves tend to overlap. Again, there is no recovery evident within the 100-ms observation window.

Discussion

The results of this particular experiment were inconclusive. The goals were not accomplished in a clear and decisive fashion, though the data in Figures 7.8 and 7.9 were somewhat dramatic. The discovery of the self-generating charge phenomenon was surprising. It bears a strong resemblance to the operation of a pyroelectric detector. Even here, however, there was a marked difference between clean and dirty film samples.

This type of experiment deserves to be repeated, with suitable modifications to improve the chances for success. It would be prudent to eliminate as many unnecessary factors as possible, e.g., eliminating the base material. One possibility would be to utilize two small, thin metal plates. One plate would be coated with 100 μm of pure gelatin, the other with 100 μm of emulsion (gelatin with a suspension of silver halide crystals with no dye). To make a capacitor, we would need to gold-coat only the gelatin and emulsion sides, attach wires, and overcoat the gold with an IR absorbing layer. Tests could then be performed similar to those already described in this chapter. The results of such a test should be far clearer than those reported here.

CHAPTER 8

CONCLUSIONS AND DISCUSSION

Introduction

In the previous chapters, we attempted to acquire some insight into what physical process makes IRPP work. We saw that the proximate cause was the shift in the characteristic curve toward higher sensitivity. In a more fundamental vein, we found that a redistribution of the quantum sensitivity population, weighted toward lower quantum numbers, accounted for the initial linear rise in the DIRE curve. Probing deeper, we discovered that IRPP takes place with or without the presence of a sensitizing dye. The dye, however, enhances the effect. Attempts to measure ionic conductivity turned up a charge separation effect analogous to the operation of pyroelectric detectors. This unexpected effect appeared to be dependent upon the presence or absence of the silver halide material in the film.

We were able to measure film temperature during the IRPP process and correlate this with IR energy and optical density. It may be that the gelatin sea (in which grains are embedded) absorbs IR photons, heats up, and transfers that heat energy to the grains. But there is still no firm evidence to indicate that IRPP is a heat- or

150

temperature-dependent effect. Although it correlates with temperature, hot film may be only a side issue distracting our attention from the main event, e.g., a true quantum optical phenomenon.

Gelatin IR Transmission

Initially, one is tempted to assume that gelatin is opaque to IR radiation. Figure 8.1 shows the spectral transmission of a 0.004 inch-thick clear gelatin sample in the region around 10.6 μm. We can calculate the attenuation coefficient from Equation (1):

$$I = I_0 \, e^{-\alpha z} \tag{1}$$

where

$$I_0 = 1$$
$$I = 0.0257$$
$$z = 101.6 \, \mu m$$

We find that

$$\alpha = 0.036 \, \mu m^{-1} \tag{2}$$

Now consider the thickness of the gelatin emulsion layer in Kodak 5369:

$$I = e^{-(.036 \mu m^{-1}) 4 \mu m} = 0.866 \tag{3}$$

This says that only 13% of the power is absorbed by the gelatin. (And some is reflected. If we knew the refractive index of gelatin, we could calculate the percent reflection.) Thin layers of gelatin are very transparent at 10.6 μm. Furthermore, as shown in Figure 8.2, bulk AgBr crystals are also highly transparent at 10.6 μm.
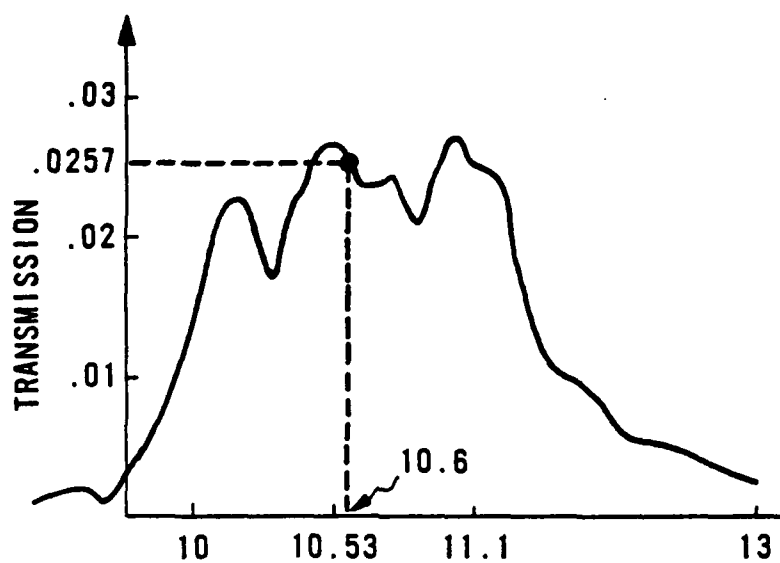
Figure 8.1. Spectral transmission of gelatin sample
(.004" thick) in the region around
10.6 microns.
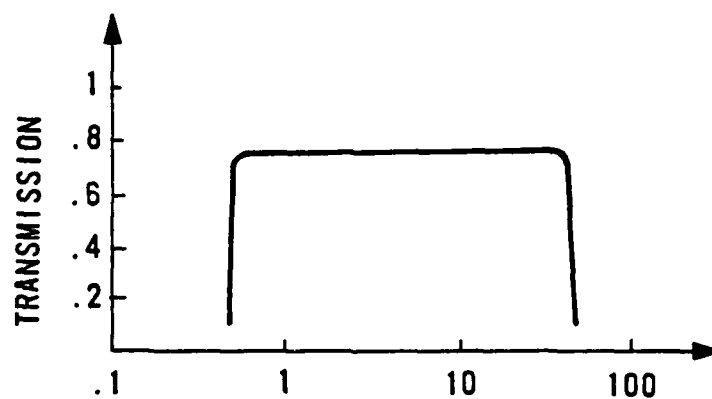
Figure 8.2. Spectral transmission of bulk AgBr
in the IR.

This indicates that significant numbers of IR photons are present and available for direct interaction with grains at all levels of the emulsion. Consider an IR irradiation of 0.1 J/cm^2. A 10.6-μm photon has an energy of 1.88×10^{-20} J. Consequently, there are 5.32×10^{18} photons/cm^2. In each square micrometer, there are 5.32×10^{10} photons. For a 0.25-μm grain (area $= 0.0625$ μm^2), there are 3.32×10^9 photons available! This is equivalent to 3.9×10^8 eV. (Recall that our visible background exposure required only 3 to 6 visible photons/grain.)

Kodak 5369 vs 2415

In Chapter 1, we saw the significant impact that visible pulse length had on the dynamic range of the IRPP phenomenon. There is an interesting side story not reported there. It involved a test comparing 5369 and 2415. Results for the short pulse are shown in Figure 8.3. Note that 5369 performs better than 2415. Figure 8.4 shows the results for the long pulse. The startling observation to be made here is the desensitization response of the 2415. What is it about 2415 that can yield such dramatically different results depending solely upon the length of the visible pulse? Could we find a pulse length to yield a null result? It would seem that a study of 2415 and visible pulse length might yield valuable clues to the mechanism of IRPP.
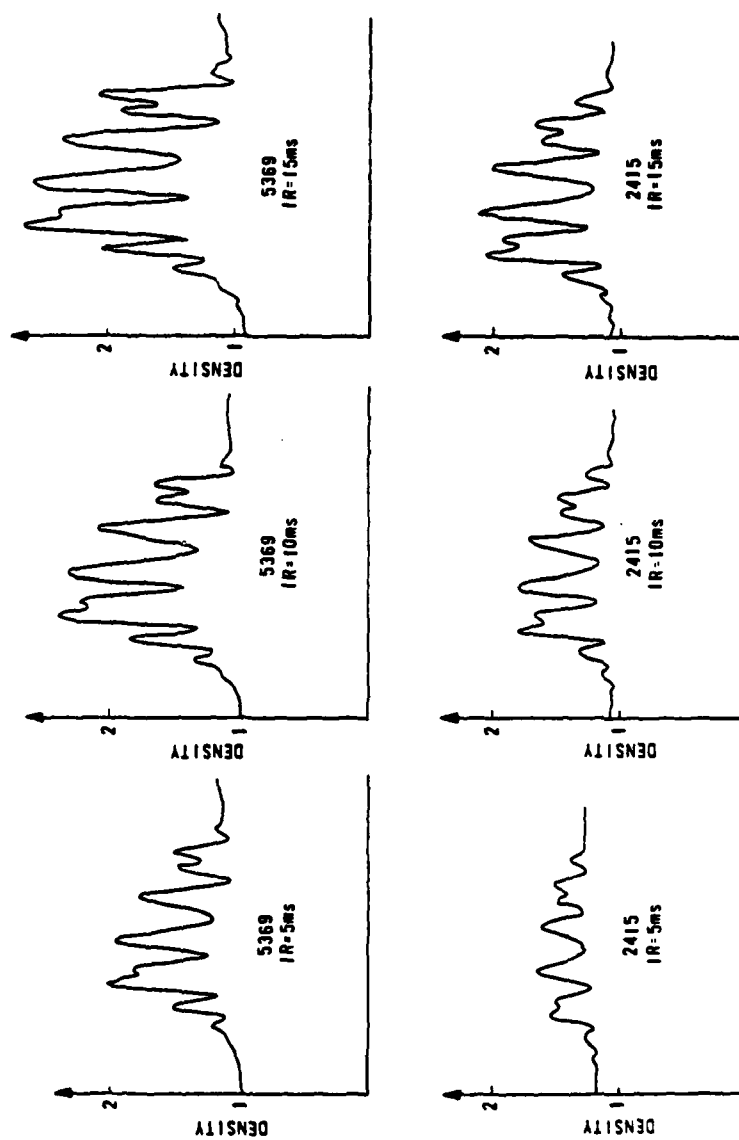
Figure 8.3. Comparison of Kodak 5369 and 2415 for short visible pulse.
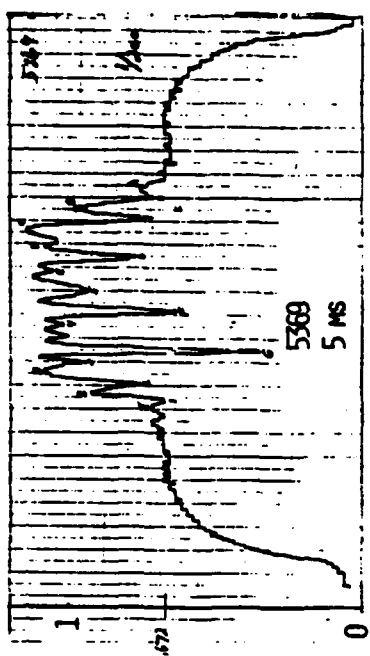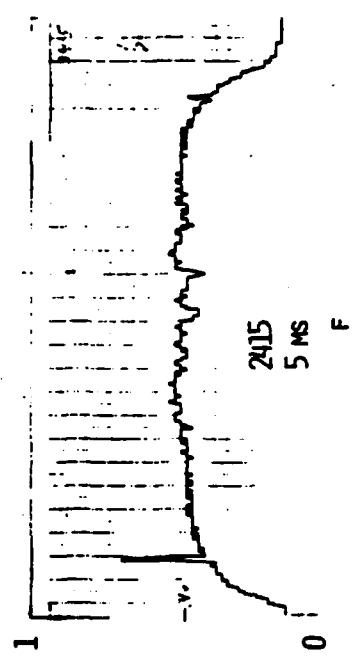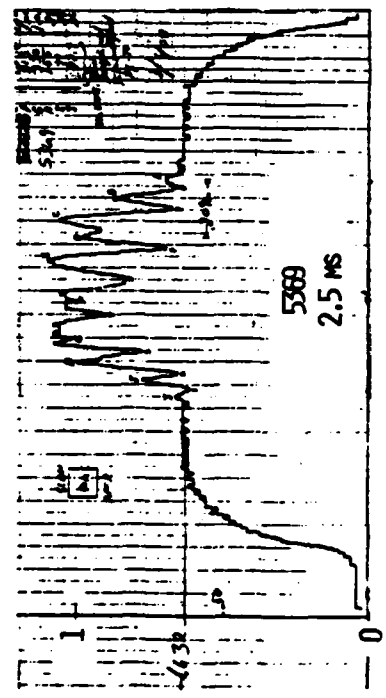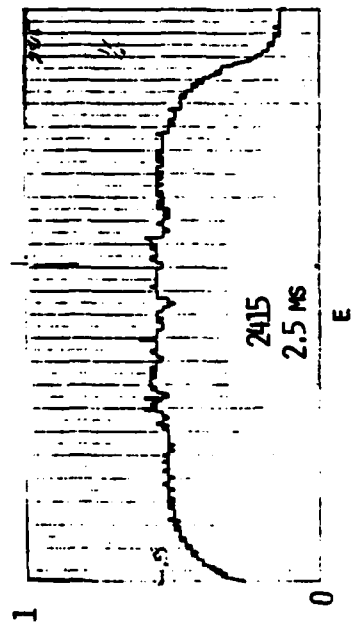
Figure 8.4. Comparison of Kodak 5369 & 2415 for long visible pulse.
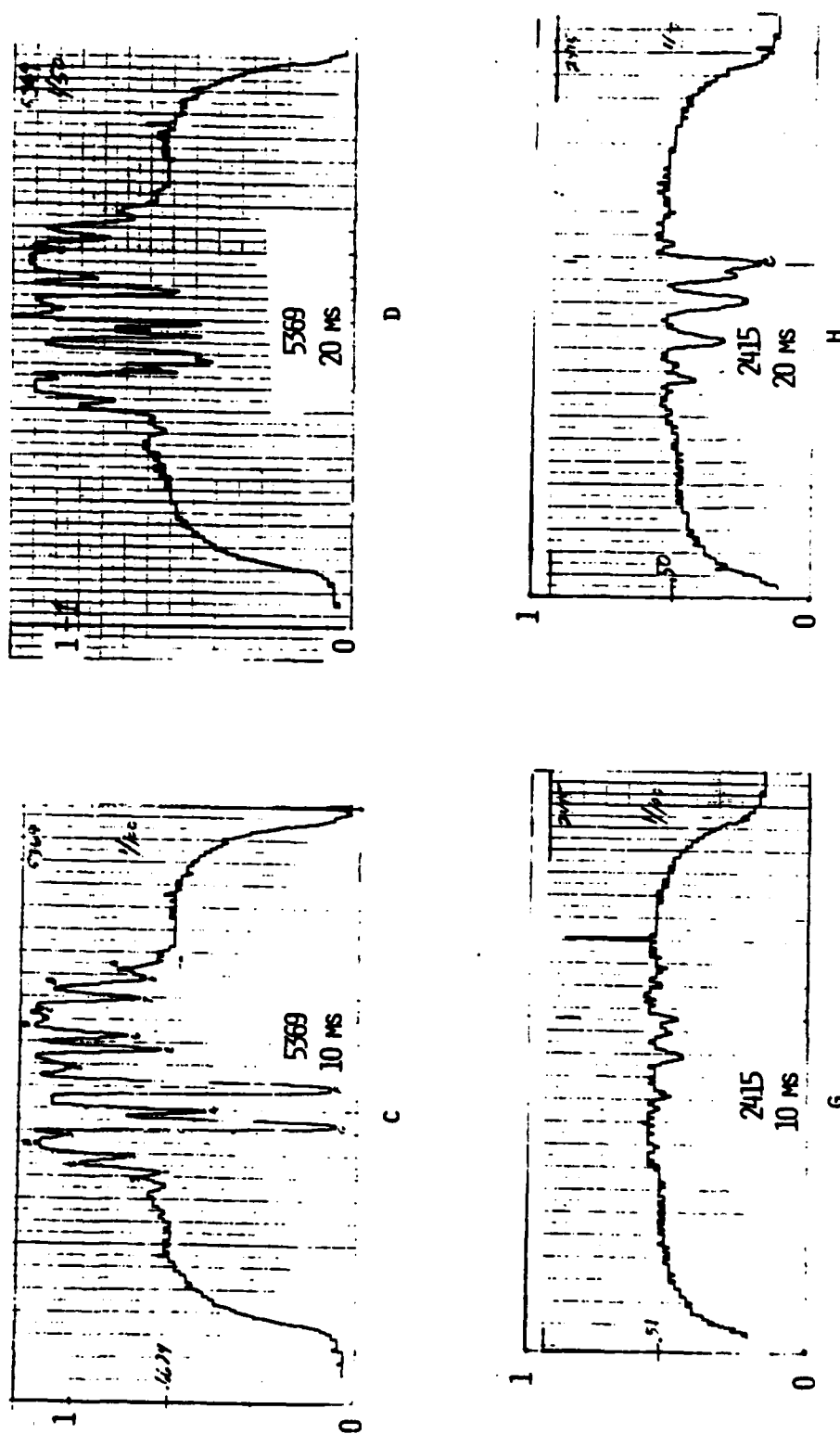
Figure 8.4. Continued

Other Double Exposure Processes

The use of two exposures[11] in sequence to increase a film's overall response is not unique to IRPP. Hypersensitization and latensification are two such processes used to ward off or minimize the effects of reciprocity failure in either the low or high irradiance regions respectively. In both cases, the high irradiance exposure is made immediately after. Both exposures are in the visible. The difference between them is that in one case the information of interest is carried by the low power exposure and in the other by the high power exposure. In either case, the first exposure seems to establish the nucleation aspect of latent image formation, and the second accomplishes the silver aggregation. Perhaps the IR exposure is also setting up nucleation. In a multiphoton process, there is potentially enough energy available to generate photoelectrons. However, it would seem that if IRPP could establish nucleation, it should also be able to follow through with aggregation as well. The IR exposure by itself, however, induces no density upon development. Obviously, the coupling efficiency of IR photons to crystal electrons is extremely low.

The IRPP phenomenon is responsible not only for sensitization but also for desensitization (depending upon IR energy and visible pulse length). In the visible realm there are several effects where desensitization occurs. There are some films that, after reaching saturation density, can become less dense with increasing exposure. This is called solarization. It is not well

understood. But modern negative emulsions are not prone to it. Furthermore, it is not a double exposure phenomenon. There are other films for which a post-exposure with red light partially destroys the latent image formed in blue light. This is the <u>Herschel effect</u>. In the <u>Villard effect</u>, a latent image formed by exposure to X-rays or high visible irradiance can be seriously degraded by a longer post-exposure to moderate irradiance. The <u>Clayden effect</u> is similar. Here, however, a short, high irradiance pre-exposure decreases the film's sensitivity to a subsequent moderate to low irradiance exposure.

There are a number of other sensitization and desensitization techniques that require development, or some special chemical treatment. These have not been discussed since IRPP does not depend on such chemical manipulation. All of the double exposure effects discussed in the previous paragraphs operate strictly in the visible. Consequently, these do not appear to have any bearing on the infrared-visible relation examined in this dissertation (which has concentrated on linear sensitization).

Future Work

The IRPP phenomenon remains a fertile field for research. This dissertation has made only modest inroads. The bulk of the DIRE curve remains to be explained, particularly the nonlinear regions. The density "ceiling" and the "reversal" phenomenon are untouched. Even in the linear sensitization region there is much left do do. A number of suggestions for further study follow: (1) The <u>specific</u>

mechanism has not been identified. For example, the whole question of heat-induced traps via transient thermal shock has yet to be investigated. If thermal shock due to the IR loading sets up more trap sites, then there is increased probability that a photoelectron will be caught at some trap in the grain. (2) The effect of visible pulse length could provide valuable data. We saw in Chapter 1 what a big difference this could make. There, however, only two different pulse times were tried. A continuous mapping of modulation and dynamic range as a function of visible pulse length (for a given IR exposure) should provide helpful insights. It would be interesting to discover whether this process is smooth and monotonic, or fraught with interesting kinks and reversals. (3) The effect of varying the IR pulse length over several orders of magnitude (constant energy exposures) is an important test of IR reciprocity failure. (4) A pertinent issue is how the DIRE curve behaves as a function of IR wavelength. For the same amount of IR energy (and same background exposure), it will be interesting to see whether density will increase or decrease as the wavelength region above and below 10.6 μm is explored. (5) Extensive investigations of dyeless emulsion types should be conducted to root out those parameters that support significant IRPP responses. This may provide valuable clues about mechanism. (6) A standard dyeless emulsion should be compared to essentially the same grain material, size, and distribution but with various sensitizing dyes attached. This should be helpful in determining how dyes enhance the IRPP effect. (7) For more

sophisticated and accurate modeling efforts, it will be important to have an emulsion whose grain size and quantum sensitivity distributions are well defined. This should be done for a standard emulsion with and without a dye present. (8) It is very likely that the IRPP effect is a quantum optics phenomenon. This is really wide open territory, and should prove a fruitful line of inquiry.

Before closing, I should like to make several more observations. First, latent image formation is still a fertile field of study. In light of this, IRPP might prove a valuable investigative tool. Such an unusual approach might provide some new and fascinating insights into this well worn and venerable topic. Second, IRPP has been used in practice to obtain information contained in an IR radiation field. But in a private conversation, Dr. Rodney Shaw indicated that it has uses in enhancing visible information as well. Film could be uniformly pre-exposed to IR radiation, thereby making it more sensitive to information contained within a visible image. Third, it may be possible to reduce the current IRPP energy requirements so that information on weaker IR fields could be successfully recorded. This would make IRPP an even more valuable tool by opening up potential application areas in remote sensing, reconnaissance, mapping, medical imaging, and astronomy. Finally, solar astronomers have current interests in obtaining data using the near IR wavelengths. It would appear that IRPP, as currently understood and practiced, is immediately usable to record such solar information. There certainly should be enough IR energy available to do the job.

APPENDIX 1

LOCATING THE IR IMAGE PLANE

The problem is to find the axial distance difference in
image plane locations between IR and visible light for a given object
distance. The power of the ZnSe singlet was known; consequently, an
object distance was selected to yield unit magnification in the IR.
The visible image on the detector plane was located experimentally.
Since the detector assembly was mounted on a carrier platform
attached to a scaled optical rail, and since the separation between
detector and window were not known, it proved more convenient to
calculate the shift required to place the detector in the appropriate
IR image plane. The power of the singlet is given by

$$\phi = (n-1)(C_1 - C_2) \tag{1.1}$$

where

$$n = \begin{cases} 2.403, & IR \\ 2.590, & VIS \end{cases} \tag{1.2}$$

Knowing ϕ for the IR, the quantity $(C_1 - C_2)$ in Equation (1.1) can be
determined:

$$(C_1 - C_2) = \frac{0.1cm^{-1}}{1.403} = 0.0713 \ cm^{-1} \quad . \tag{1.3}$$

We can now use Equations (1.3), (1.2) and (1.1) to find the power of
the lens in the visible:

$$\phi_v = (1.59)(0.0713) = 0.1134 \ cm^{-1} \tag{1.4}$$

161

With the object distance set at 20 cm, we can use the lens equation

$$\frac{1}{L_v} + \frac{1}{L_v'} = \phi_v \qquad (1.5)$$

with Equation (1.4) to find the visible image distance L_v':

$$L_v' = (0.1134-.05)^{-1} = 15.78 \text{ cm} \qquad (1.6)$$

At unit magnification in the IR, the image distance L_{IR}' is 20 cm. Consequently, the axial distance difference between IR and visible image planes is

$$\Delta L' = L_{IR}' - L_v' = 4.22 \text{ cm} \qquad (1.7)$$

To our experimentally determined visible image plane we must increase the lens–detector separation by $\Delta L'$ in order to locate the IR image plane.

APPENDIX 2

SAMPLE DENSITY CALCULATION VIA SHAW MODEL

We wish to illustrate how Equation (15) in Chapter 5 is used to calculate density in the presence of both a grain size and quantum sensitivity distribution. The distributions used in this hand calculation are presented in Table 2.1.

TABLE 2.1			
Grain Size		Quantum Sensitivity	
a_i	β_i	Q_j	α_j
0.5	0.35	4	0.50
1	0.25	5	0.30
2	0.40	6	0.20

These values will be substituted into Equation (2-1):

$$D = D_0 \left\{ 1 - \frac{1}{\bar{a}} \Sigma_i \beta_i \left\{ a_i e^{-a_i q} \Sigma_j \alpha_j \left[\Sigma_0^{Q-1} \frac{(a_i q)^r}{r!} \right] \right\} \right\} \qquad (2\text{-}1)$$

where

$$q = 5$$

$$\bar{a} = \Sigma_1 \beta_i a_i = 2.1$$

We start by calculating the factor within the brackets.

$$Q \Sigma_0^{-1} \frac{(a_i q)^r}{r!} = 1 + 5a_i + \frac{(5a_i)^2}{2} + \frac{(5a_i)^3}{6} + \frac{(5a_i)^4}{24} + \frac{(5a_i)^5}{120} \qquad (2\text{-}2)$$

The first four terms are used when Q = 4; the first five, when Q = 5; all terms, when Q = 6. Table 2.2 tabulates the results.

TABLE 2.2

a_i	Q_i		
	4	5	6
0.5	9.23	10.86	11.67
1	39.33	65.38	91.42
2	227.67	644.33	1477.67

Next, the quantity $a_i e^{-a_i q}$ is determined. Table 2.3 presents this data.

TABLE 2.3

a_i	$a_i e^{-5a_i}$
0.5	4.10×10^{-2}
1	6.74×10^{-3}
2	9.08×10^{-5}

All these values are substituted into Equation (2-1):

$$D = D_\theta \left\{ 1 - \frac{1}{a}.476 \left\{ \beta_i .35 \left\{ a_i e^{-5a_i} 4.10 \times 10^{-2} \right\} \left\{ \alpha_4 \sum_\theta^4 \frac{1}{\theta}.5(9.23) + \alpha_5 \sum_\theta^5 \frac{1}{\theta}.3(10.86) + \alpha_6 \sum_\theta^6 \frac{1}{\theta}.2(11.67) \right\} \right\} \right.$$

$$+ .25 \left\{ 6.74 \times 10^{-3} \left\{ .5 (39.33) + .3(65.38) + .2(91.42) \right\} \right\}$$

$$\left. + .40 \left\{ 9.08 \times 10^{-5} \left\{ .5(227.67) + .3(644.33) + .2(1477.67) \right\} \right\} \right\}$$

$$D = D_\theta \{ 1 - .476 \{ .1465 + .0970 + .0219 \} \}$$

$$D = D_\theta \left\{ 1 - 0.1263 \right\} = 0.8737\ D_\theta$$

As can be readily appreciated, hand calculations for reasonable grain size and quantum sensitivity distributions would be formidable, and prone to error. The hand calculation presented here was necessary, however, to check the validity of the computer programs (cf Appendix 3) used to compute density values for the rest of Chapter 5.

APPENDIX 3

SHAW MODEL PROGRAMS

The basic Shaw model program and variations were supplied
via the auspices of Dr. Phil Peterson. Program A3.1 was used to
examine the effect of thermal expansion of AgBr grains. Program A3.2
was used in the modified linear quantum sensitivity model (Q=1).
Program A3.3 was used in conjunction with the negative binomial
distribution of quantum sensitivity.

A3.1

```fortran
      DIMENSION ALPHA(54),BETA(14),A(14),Q(54),AA(14),ALP(54)
C**LNA IS THE UPPER BOUND ON THE BETA SUM,LNQ ON THE ALPHA SUM**
      ACCEPT*,F
      ACCEPT*,QS
      ACCEPT*,DELA
      LNA=14
      LNQ=15
      B=1
      XNUM=3.3
      BIGA=1
      WRITE(6,101)LNA
      WRITE(6,102)F
      WRITE(6,103)QS
      WRITE(6,105)B
      WRITE(6,106)XNUM
      WRITE(6,107)BIGA
C**BUILDING BETA MATRIX FROM GAUSSIAN**
      V1=.18766649
      V2=1.3163763
      V3=.60334105
      WRITE(6,111)
      DO 1 J=1,LNA,1
      AA(J)=0.2 + 0.2*(J-1)
      A(J)=AA(J)*(1.0 + DELA)
      BETA(J)=V1*EXP((-(AA(J) - V2)**2)/(V3**2))
      ABAR=ABAR + A(J)*BETA(J)
      WRITE(6,108)A(J),BETA(J),ABAR
    1 CONTINUE
C***BUILDING ALPHA MATRIX FROM EXPONENTIAL FIT**
      WRITE(6,112)
      DO 2 I=1,LNQ,1
      Q(I)=3 + I
C      ALPHA(I)=-.000781550*Q(I) + .041836200
      ALPHA(I)=.225*EXP(-.25*(Q(I) - 4.0))
    2 CONTINUE
      IF(F .EQ. 0.0)GO TO 4
      LQ=3
      Q(1)=LQ
      Q(16)=18
      ALP(1)=F*ALPHA(1)
      ALP(16)=(1 - F)*ALPHA(15)
      DO 3 I=2,LNQ,1
      Q(I)=LQ-1+I
      ALP(I)=(1.-F)*ALPHA(I-1) + F*ALPHA(I)
    3 CONTINUE
      LNQ=LNQ + 1
      DO 22 J=1,LNQ,1
      ALPHA(J)=ALP(J)
   22 CONTINUE
    4 CONTINUE
      WRITE(6,109)(Q(J),ALPHA(J),J=1,LNQ)
```

```
      SUM3=0.0
      DO 30 NA=1,LNA,1
      SUM2=0.0
      DO 20 NQ=1,LNQ,1
      SUM1=0.0
      FAC=1.0
      TRM1=1.0
      DO 10 NR=0,Q(NQ)-1,1
      IF(NR .EQ. 0)GO TO 5
      TRM1=TRM1*((A(NA)*QS)/NR)
      GO TO 6
    5 TRM1=1.0
    6 CONTINUE
      SUM1=SUM1 + TRM1
   10 CONTINUE
      TRM2=ALPHA(NQ)*SUM1
      SUM2=SUM2 + TRM2
   20 CONTINUE
      TRM3=SUM2*BETA(NA)*A(NA)*EXP(-A(NA)*QS)
      SUM3=SUM3 + TRM3
   30 CONTINUE
      TSUM=SUM3/ABAR
      BRKT=1.0 - TSUM
      DEN=B*XNUM*BRKT/BIGA
      WRITE(6,400)DEN
  400 FORMAT(2X,'DENSITY= ',E13.6)
  101 FORMAT(2X,'NUMBER OF TERMS IN A SUM=',I4)
  102 FORMAT(2X,'F IS = ',E10.3)
  103 FORMAT(2X,'AVERAGE # OF PHOTONS/GRAIN',E10.3)
  105 FORMAT(2X,'SCALING FACTOR= ',E10.3)
  106 FORMAT(2X,'AVERAGE NUMBER OF GRAINS IN SAMPLING APERTURE= ',
     :E10.3)
  107 FORMAT(2X,'SAMPLING APERTURE SIZE= ',E10.3)
  108 FORMAT(2X,E10.3,20X,E10.3,3X,E10.3)
  109 FORMAT(2X,E10.3,23X,E10.3)
  111 FORMAT(2X,'GRAIN SIZE',12X,'FRACTIONAL POPULATION',
     :5X,'ABAR')
  112 FORMAT(2X,'QUANTUM SENSITIVITY',10X,'FRACTIONAL QS POPULATION')
      END
```

```
                              A3.2
      DIMENSION ALPHA(54),BETA(14),A(14),Q(54),AA(14),ALPH(54)
C**LNA IS THE UPPER BOUND ON THE BETA SUM,LNQ ON THE ALPHA SUM**
      ACCEPT*,F,G
      ACCEPT*,QS
      ACCEPT*,DELA
      ACCEPT*,EPS
      ACCEPT*,XNUM
      LNA=1
      LNQ=15
      B=1
      BIGA=1
      WRITE(6,101)LNA
      WRITE(6,102)F,G
      WRITE(6,103)QS
      WRITE(6,105)B
      WRITE(6,106)XNUM
      WRITE(6,107)BIGA
C**BUILDING BETA MATRIX FROM GAUSSIAN**
      V1=.18766649
      V2=.25
      V3=.09
      WRITE(6,111)
      DO 1 J=1,LNA,1
      AA(J)=EPS + 0.03*(J-1)
      A(J)=AA(J)*(1.0 + DELA)
C     BETA(J)=V1*EXP((-(A(J) - V2)**2)/(V3**2))
      BETA(1)=1.
      ABAR=ABAR + A(J)*BETA(J)
      WRITE(6,108)A(J),BETA(J),ABAR
    1 CONTINUE
C***BUILDING ALPHA MATRIX FROM EXPONENTIAL FIT**
      WRITE(6,112)
      DO 2 I=1,LNQ,1
      Q(I)=3 + I
      ALPH(I)=.225*EXP(-.25*(Q(I) - 4.0))
    2 CONTINUE
      IF(F .EQ. 0.0)GO TO 4
      Q(18)=18
      ALPHA(18)=(1.0-F)*ALPH(15)
      DO 22 J=17,4,-1
      Q(J)=J
      ALPHA(J)=(1.0-F)*ALPH(J-3) + F*ALPH(J-2)
   22 CONTINUE
      Q(3)=3
      Q(2)=2
      Q(1)=1
      ALPHA(1)=(G**2)*F*ALPH(1)
      ALPHA(2)=G*F*ALPH(1)-(G**2)*F*ALPH(1)
      ALPHA(3)=F*ALPH(1)-G*F*ALPH(1)
      LNQ=18
      WRITE(6,109)(Q(J),ALPHA(J),J=1,18)
```

```
      GO TO 23
  4   CONTINUE
      DO 24 I=1,LNQ,1
      ALPHA(I)=ALPH(I)
  24  CONTINUE
      WRITE(6,109)(Q(J),ALPHA(J),J=1,LNQ)
  23  CONTINUE
      XTT=0.0
      DO 77 I=1,LNQ,1
      XT=ALPHA(I)
      XTT=XTT + XT
  77  CONTINUE
      WRITE(6,301)XTT
 301  FORMAT(20X,'SUM OVER ALL ALPHAS = ',E10.3)
      SUM3=0.0
      DO 30 NA=1,LNA,1
      SUM2=0.0
      DO 20 NQ=1,LNQ,1
      SUM1=0.0
      FAC=1.0
      TRM1=1.0
      DO 10 NR=0,Q(NQ)-1,1
      IF(NR .EQ. 0)GO TO 5
      TRM1=TRM1*((A(NA)*QS)/NR)
      GO TO 6
  5   TRM1=1.0
  6   CONTINUE
      SUM1=SUM1 + TRM1
 10   CONTINUE
      TRM2=ALPHA(NQ)*SUM1
      SUM2=SUM2 + TRM2
 20   CONTINUE
      TRM3=SUM2*BETA(NA)*A(NA)*EXP(-A(NA)*QS)
      SUM3=SUM3 + TRM3
 30   CONTINUE
      TSUM=SUM3/ABAR
      BRKT=1.0 - TSUM
      DEN=B*XNUM*BRKT/BIGA
      WRITE(6,400)DEN
 400  FORMAT(2X,'DENSITY= ',E10.3)
 101  FORMAT(2X,'NUMBER OF TERMS IN A SUM=',I4)
 102  FORMAT(2X,'F IS = ',E10.3,5X,'FRACTION OF F =',E10.3)
 103  FORMAT(2X,'AVERAGE # OF PHOTONS/GRAIN',E10.3)
 105  FORMAT(2X,'SCALING FACTOR= ',E10.3)
 106  FORMAT(2X,'AVERAGE NUMBER OF GRAINS IN SAMPLING APERTURE= ',
     :E10.3)
 107  FORMAT(2X,'SAMPLING APERTURE SIZE= ',E10.3)
 108  FORMAT(2X,E10.3,20X,E10.3,3X,E10.3)
 109  FORMAT(2X,E10.3,23X,E10.3)
 111  FORMAT(2X,'GRAIN SIZE',12X,'FRACTIONAL POPULATION',
     :5X,'ABAR')
 112  FORMAT(2X,'QUANTUM SENSITIVITY',10X,'FRACTIONAL QS POPULATION')
      END
```

A3.3

```
      DIMENSION ALPHA(54),BETA(14),A(14),Q(54),AA(14),ALPH(54)
     :,LQ(54)
C**LNA IS THE UPPER BOUND ON THE BETA SUM,LNQ ON THE ALPHA SUM**
      ACCEPT*,QS
      ACCEPT*,DELA
      ACCEPT*,EPS
      ACCEPT*,XNUM
      ACCEPT*,NT
      ACCEPT*,M
      LNA=1
      LNQ=40
      B=1
      BIGA=1
      WRITE(6,101)LNA
      WRITE(6,102)NT,M
      WRITE(6,103)QS
      WRITE(6,105)B
      WRITE(6,106)XNUM
      WRITE(6,107)BIGA
C**BUILDING BETA MATRIX FROM GAUSSIAN**
      V1=.18766649
      V2=.25
      V3=.09
      WRITE(6,111)
      DO 1 J=1,LNA,1
      AA(J)=EPS + 0.03*(J-1)
      A(J)=AA(J)*(1.0 + DELA)
C     BETA(J)=V1*EXP((-(A(J) - V2)**2)/(V3**2))
      BETA(1)=1.
      ABAR=ABAR + A(J)*BETA(J)
      WRITE(6,108)A(J),BETA(J),ABAR
    1 CONTINUE
C***BUILDING ALPHA MATRIX FROM NEGATIVE BINOMIAL**
      WRITE(6,112)
      DO 511 J=1,LNQ,1
      LQ(J)=NT + (J-1)
      Q(J)=FLOAT(LQ(J))
      F=1.0
      ANS=1.0
      DO 512 I=1,NT-1,1
      F=(Q(J)-I)*F
      ANS=ANS*I
  512 CONTINUE
      ST=((1./M)**NT)*(1.0 - 1./M)**(LQ(J)-NT)
      ALPHA(J)=F*ST/ANS
  511 CONTINUE
      WRITE(6,109)(Q(J),ALPHA(J),J=1,LNQ)
      XTT=0.0
      DO 77 I=1,LNQ,1
      XT=ALPHA(I)
      XTT=XTT+XT
```

```
   77 CONTINUE
      WRITE(6,301)XTT
  301 FORMAT(20X,'SUM OVER ALL ALPHAS=',E10.3)
      SUM3=0.0
      DO 30 NA=1,LNA,1
      SUM2=0.0
      DO 20 NQ=1,LNQ,1
      SUM1=0.0
      FAC=1.0
      TRM1=1.0
      DO 10 NR=0,Q(NQ)-1,1
      IF(NR .EQ. 0)GO TO 5
      TRM1=TRM1*((A(NA)*QS)/NR)
      GO TO 6
    5 TRM1=1.0
    6 CONTINUE
      SUM1=SUM1 + TRM1
   10 CONTINUE
      TRM2=ALPHA(NQ)*SUM1
      SUM2=SUM2 + TRM2
   20 CONTINUE
      TRM3=SUM2*BETA(NA)*A(NA)*EXP(-A(NA)*QS)
      SUM3=SUM3 + TRM3
   30 CONTINUE
      TSUM=SUM3/ABAR
      BRKT=1.0 - TSUM
      DEN=B*XNUM*BRKT/BIGA
      WRITE(6,400)DEN
  400 FORMAT(2X,'DENSITY= ',E10.3)
  101 FORMAT(2X,'NUMBER OF TERMS IN A SUM=',I4)
  102 FORMAT(2X,'T=   ',I3,5X,'M= ',I5)
  103 FORMAT(2X,'AVERAGE # OF PHOTONS/GRAIN',E10.3)
  105 FORMAT(2X,'SCALING FACTUR= ',E10.3)
  106 FORMAT(2X,'AVERAGE NUMBER OF GRAINS IN SAMPLING APERTURE= ',
     :E10.3)
  107 FORMAT(2X,'SAMPLING APERTURE SIZE= ',E10.3)
  108 FORMAT(2X,E10.3,20X,E10.3,3X,E10.3)
  109 FORMAT(2X,E10.3,23X,E10.3)
  111 FORMAT(2X,'GRAIN SIZE',12X,'FRACTIONAL POPULATION',
     :5X,'ABAR')
  112 FORMAT(2X,'QUANTUM SENSITIVITY',10X,'FRACTIONAL QS POPULATION')
      END
```

LIST OF REFERENCES

1. G.F. Frazier, T.D. Wilkerson, and J.M. Lindsay, Appl. Opt. 15, 1350 (1976).

2. G.F. Frazier, J. Appl. Photo. Engr. 3, 31 (1977).

3. N.H. Burnett, H.Z. Baldis, G.D. Enright, M.C. Richardson, and P.B. Corkum, J. Appl. Phys. 48, 3727 (1977).

4. G.R. Mitchel, B. Grek, F. Martin, H. Pepin, F. Rheault, and H. Baldis, J. Phys. D: 11, L153 (1978).

5. G.R. Mitchel, B. Grek, T.W. Johnston, F. Martin, and H. Pepin, Appl. Opt. 18, 2422 (1979).

6. D. Naor, A. Flusberg, and I. Itzkan, Appl. Opt. 20, 2574 (1981).

7. D.P. Juyal, S.P. Gupta, and R. Hradaynath, Appl. Opt. 22, 2152 (1983).

8. J. Geary, D. Vunck, B. Deuto, R. Sessions, D. Duneman, C. Moeller, R. Wick, S.P.I.E. PROCEEDING, Vol. 429, pa. 153.

9. J.C. Dainty, and R. Shaw, Image Science, Academic Press (1974).

10. A. Marriage, J. Photogr. Sci., 9, 93 (1961).

11. T.H. James, The Theory of the Photographic Process, 4th Edition, Macmillan Pub. Co. (1977).

END

FILMED

11-84

DTIC